Mohamed Boudiaf University - M'sila

FACULTY OF TECHNOLOGY

DEPARTMENT OF ELECTRICAL ENGINEERING

Serial number……..…

Registration number: D.ER/3C/05/22

Thesis

Presented for the Degree of

DOCTORATE LMD

Field: Renewable Energies

Specialty: Renewable Energies

THEME

Enhancement of Robust and Optimal Control Techniques for the Energy Produced by a Variable-Speed Wind Energy Conversion System Based on DFIM

Presented By

Mohammed OUINTEN

Supported on: 15/06/2026

Before the jury composed of**:**

Surname & Name	**Grade**	**Establishment**	**Quality**
Abderrahim ZEMMIT	Professor	University of M'Sila	President
Riyadh ROUABHI	Professor	University of M'Sila	Supervisor
Abdelghafour HERIZI	Associate Professor A	University of M'Sila	Co-Supervisor
Oussama MOUSSA	Associate Professor A	University of Ghardaia	Examiner
Ali AKKA	Associate Professor A	Higher School of Boussaâda	Examiner
Salim DJERIOU	Associate Professor A	University of M'Sila	Examiner

Academic year: 2025/ 2026

Université Mohamed Boudiaf - M'Sila

FACULTE DE TECHNOLOGIE

DEPARTEMENT DE GENI ELECTRIQUE

Numéro de série……

Numéro d'inscription : D.ER/3C/05/22

Thèse

Présentée pour l'obtention du diplôme de

DOCTORAT LMD

Filière : Énergies Renouvelables

Spécialité : Énergies Renouvelables

THEME

Amélioration des Techniques de Commande Robuste et Optimale de l'Énergie Produite par un Système de Conversion d'Énergie Éolienne à Vitesse Variable Basé sur une MADA

Présenté par

Mohammed OUINTEN

Soutenue le : 15/06/2026

Devant le jury composé de :

Prénom et nom	**Grade**	**Établissement**	**Qualité**
Abderrahim ZEMMIT	Professeur	Université de M'Sila	Président
Riyadh ROUABHI	Professeur	Université de M'Sila	Directeur de thèse
Abdelghafour HERIZI	M.C.A	Université de M'Sila	Co-Encadreur de thèse
Oussama MOUSSA	M.C.A	Université de Ghardaïa	Examinateur
Ali AKKA	M.C.A	Ecole supérieur de Boussaâda	Examinateur
Salim DJERIOU	M.C.A	Université de M'Sila	Examinateur

Année Universitaires : 2025/ 2026

Acknowledgment

In the name of God, the All Knowing and All Wise

First of all, I want to express my sincere gratitude and utmost praise to Allah Almighty, who has blessed me with His infinite grace and care. By His will and permission, my efforts have come to fruition and this work has been successfully completed.

I would like to convey my deep appreciation to my supervisor, **Professor Riyadh ROUABHI** and my co-supervisor, **Dr. Abdelghafour HERIZI** for their continuous support, valuable guidance, patience and insightful suggestions. Their expertise, constructive criticism, and thoughtful advice have greatly enriched this work and shaped my academic development.

I am deeply honored and sincerely grateful to the distinguished members of my thesis defense committee for their willingness to examine and evaluate this dissertation.

My sincere appreciation is extended to:

- **Mr. Abderrahim ZEMMIT**, Professor at the University of M'Sila, for graciously accepting to chair the thesis defense committee.
- **Mr. Oussama MOUSSA**, Senior Lecturer at the University of Ghardaia, for kindly accepting to examine and evaluate this dissertation.
- **Mr. Ali AKKA**, Senior Lecturer at Higher School of Boussaâda, for kindly accepting to examine and evaluate this dissertation.
- **Mr. Salim DJERIOU**, Senior Lecturer at the University of M'Sila, for kindly accepting to examine and evaluate this dissertation.

I am truly grateful for the time, expertise, and valuable insights they have devoted to the assessment of this work.

Dedication

I devote this thesis, with heartfelt gratitude, to the memory of my beloved parents. whose love, guidance, and sacrifices forever inspire me.

I warmly thank my family, friends and loved ones for their steadfast support and encouragement, patience, and moral support during both difficult and joyful moments of this journey.

And also, to the heroes, children, and women of Gaza, whose courage, resilience, and dignity inspire humanity.

May Allah accept this modest effort and make it a source of benefit.

Mohammed OUINTEN

List of publications and communications

International publications:

- ✓ M. Ouinten, R. Rouabhi, and A. Herizi, "Power enhancement using Grey Wolf Optimizer algorithm for doubly fed induction generator based on fuzzy logic controller", Diagnostyka, vol. 27, no. 1, Art. no. 2026101, 2026, e-ISSN: 2449-5220, doi: 10.29354/diag/216415.

International communications:

- ✓ M. Ouinten, R. Rouabhi, A. Herizi, and L. Bensaadia, "Active and reactive powers control of doubly fed induction generator using interval type-1 fuzzy controller", 1st International Conference on Engineering, Natural and Social Sciences, ICENSOS 2022, December 20-23, 2022, Konya. Turkey
- ✓ Mohammed Ouinten, Riyadh Rouabhi, Abdelghafour Herizi, and Salim Djeriou, "Type-1 adaptive fuzzy logic control of a permanent magnet synchronous machine (PMSM)", 8th International education and innovative science congress, 24-26, 2023, Ankara, Turkey
- ✓ M. Ouinten, R. Rouabhi, and A. Herizi, "Wind Energy Production in Algeria", 12th International Scientific Research and Innovation Congress, MARCH 3-4, 2024, Almaty Kazakhstan.
- ✓ M. Ouinten, R. Rouabhi, A. Herizi, B. Bendjaima, and A. Ouali "Modeling and simulation of the double fed induction machine for both motor and generator operating modes", Mas 19th International European conference on mathematics, engineering, natural & medical sciences April 17-18, 2024. Mingachevir State University, Mingachevir, Azerbaijan.
- ✓ M. Ouinten, R. Rouabhi, and A. Herizi, "Robust non-linear control of a doubly-fed induction generator", II. International future engineering conference, IFEC2O25, April 28-29, 2025, Baku, Azerbaijan.

National communications:

- ✓ M. Ouinten, R. Rouabhi, A. Herizi, A. Fezzani, I. Hadjmahammed, and S. Bennacer "Design and implementation of an electronic load for characterizing photovoltaic modules", The First National Conference on Renewable Energies and Advanced Electrical Engineering, NC-REAEE'25, May 06-07th, 2025, Mohammed Boudiaf University of M'Sila.

Contents

Acknowledgment *I*
Dedication *II*
Contents *IV*
General Introduction *1*
Chapter I : Overview of Wind Energy Systems **4**
I.1 Introduction 4
I.2 Statistics on Scientific Production in Wind Energy 4
I.2.1 Wind Energy Publication Statistics in the IEEE Database 4
I.2.2 Wind Energy Publication Statistics in the ScienceDirect Database 5
I.2.3 Wind Energy Publication Statistics in the Springer Nature Database 5
I.3 Statistics on Wind Energy Installation and Production 6
I.3.1 Wind Energy Advancement in America 7
I.3.2 Wind Energy Advancement in Africa and the Middle East 8
I.3.3 Wind Energy Advancement in Asia 9
I.3.4 Wind Energy Advancement in Europe 10
I.4 Global Leaders in Wind Energy Installed Capacity and Market Share 11
I.5 Overview of the DFIM 12
I.5.1 Operation Description of the DFIM 12
I.5.2 Different Configurations of the DFIM 15
I.5.3 DFIM Applications 20
I.5.4 Advantages and Disadvantages of the DFIM 20
I.6 Conclusion 21
Chapter II : Wind Energy Conversion System Modeling **22**
II.1 Introduction 22
II.2 DFIM Modeling 23
II.2.1 Simplifying Assumptions 23
II.2.2 Mathematical Equations of the DFIM in (a b c) System 23
II.2.3 Park Transformation 25
II.2.4 Mathematical Equations of the DFIM in (d–q) System 26
II.2.5 Reference Frame Selection 27
II.2.6 State-Space Representation of the DFIM Model 27
II.3 Machine Side Converter Modeling and Control 28
II.3.1 Machine Side Converter Modeling 28
II.3.2 PWM Control 30
II.4 Grid-Side Converter Modeling and Control 30
II.4.1 Grid-Side Converter Modeling 31
II.4.2 Grid-Side Converter Control 32
II.4.3 Simulation Results 34
II.4.4 Results Interpretation 34
II.5 Wind Turbine Modeling and Control 34
II.5.1 Wind Turbine Aerodynamic Modeling 34
II.5.2 Wind Turbine Control 39
II.5.3 Simulation Results 43
II.5.4 Results Interpretation 43
II.6 Conclusion 44
Chapter III : Theoretical Aspects of the Control System and Optimization Method **45**
III.1 Introduction 45
III.2 Stator Flux-Oriented Control 45
III.2.1 Principle of SFOC 45
III.2.2 Different Types of SFOC 45
III.2.3 Advantages and Disadvantages of SFOC 48

III.2.4 Different Types of Controllers Used 49
III.3 Optimization Using the GWO Algorithm 51
III.3.1 Definition 51
III.3.2 Principle of the Technique 51
III.3.3 Operators 52
III.3.4 Mathematical Model of the GWO Technique 53
III.3.5 Objective Function for the Grey Wolf Optimizer 55
III.4 Conclusion 56
Chapter IV : Control System Implementation and Optimization Technique **57**
IV.1 Introduction 57
IV.2 SFOC Algorithm 57
IV.2.1 Stator–Rotor Current Relationship under SFOC 58
IV.2.2 Stator Power–Rotor Current Relationship under SFOC 58
IV.2.3 Rotor Voltage–Current Relationship under SFOC 59
IV.3 Implementation of the GWO Algorithm in the Simulation 60
IV.3.1 SFOC Based on PI-GWO Controllers 62
IV.3.2 Optimal Fuzzy Control Using GWO 64
IV.3.3 SFOC Based on FPD-GWO Controllers 65
IV.3.4 SFOC Based on FPD+I-GWO Controllers 67
IV.4 Comparative Analysis and Control Performance 70
IV.4.1 Qualitative Comparisons 70
IV.4.2 Quantitative Comparisons 70
IV.5 Optimality and Robustness Analysis 72
IV.5.1 Optimality Analysis 72
IV.5.2 Robustness Analysis 75
IV.6 Conclusion 76
General Conclusion ***77***
Bibliographies ***79***
Appendix ***85***

Figure I-1 : Wind Energy Publications in the IEEE Database 5
Figure I-2 : Wind Energy Publications in the ScienceDirect Database 5
Figure I-3 : Wind Energy Publications in the Springer Nature Database 6
Figure I-4 : Global Growth of Wind Energy Installations (2001–2025) 6
Figure I-5 : Evolution of Onshore and Offshore Wind Installations Worldwide 7
Figure I-6 : Wind Power Capacity in the Americas in 2025 7
Figure I-7 : Wind Power Capacity in Africa and the Middle East in 2025 8
Figure I-8 : Wind Power Capacity in Asia in 2025 9
Figure I-9 : Wind Power Capacity in Europe in 2025 10
Figure I-10 : Breakdown of Wind Power in the Top 10 Countries in 2025 11
Figure I-11 : DFIM Structure 13
Figure I-12 : Operation in Sub-Synchronous Motor Mode 13
Figure I-13 : Operation in Super-Synchronous Motor Mode 14
Figure I-14 : Operation in Sub-Synchronous Generator Mode 14
Figure I-15 : Operation in Super-Synchronous Generator Mode 15
Figure I-16 : Diagram of the DFIM with Its Rotor Powered by an Inverter 16
Figure I-17 : Diagram of the DFIM with Its Rotor Powered by a Cycloconverter 16
Figure I-18 : Block Diagram for Power Supply via Two Cycloconverters 17
Figure I-19 : DFIM with Slip Control by Dissipated Energy 18
Figure I-20 : DFIM (Kramer Structure) 18
Figure I-21 : Scherbius Structure with Cycloconverter 19
Figure I-22 : Scherbius Structure with PWM Converters 19
Figure II-1 : WECS Block Diagram 22
Figure II-2 : DFIM Representation in the Three-Phase Reference Frame 23
Figure II-3 : Park Reference Orientation 25
Figure II-4 : Simplified Diagram of a Two-Level Three-Phase Inverter 28
Figure II-5 : GSC Structure 31
Figure II-6 : GSC Block diagram 32
Figure II-7 : GSC Control Block Diagram 33
Figure II-8 : (a) DC Bus Voltage, (b) Line Voltage and Line Current 34
Figure II-9 : Power Coefficient Curves versus Lambda and Beta 36
Figure II-10 : Mechanical Model of the Turbine 37
Figure II-11 : Simplified Model of the Turbine 37
Figure II-12 : WT Model 38
Figure II-13 : Power-speed curve of WT 39
Figure II-14 : WT and MPPT Model 40
Figure II-15 : Blade Orientation 41
Figure II-16 : Blade Orientation Control System 42
Figure II-17 : Pitch Control System 42
Figure II-18 : Mechanical Speed and Power Generated Signal 43
Figure II-19 : Power Coefficient and Specific Speed 43
Figure III-1 : Direct Control 46
Figure III-2 : Indirect Open-Loop Power Control 47
Figure III-3 : Indirect Closed-Loop Power Control 47
Figure III-4 : PI Controller Structure 49
Figure III-5 : Fuzzy Logic System 50
Figure III-6 : Fuzzy PD Controller Structure 50
Figure III-7 : Fuzzy PD+I Controller Structure 51

Figure III-8 : Hierarchy of a Grey Wolf Pack 52
Figure III-9 : Attacking Prey versus Searching Prey 53
Figure III-10 : Position Updating in GWO 54
Figure III-11 : GWO Algorithm Flowchart 55
Figure IV-1 : Block Diagram of the Simplified DFIG Model 60
Figure IV-2 : PI Control 62
Figure IV-3 : Stator Power Response Using PI–GWO Controller at Constant Wind Speed 63
Figure IV-4 : Stator Power Response Using PI–GWO Controller at Variable Wind Speed 63
Figure IV-5 : Membership Function for Input Variables 64
Figure IV-6 : Membership Function for Output Variable 64
Figure IV-7 : Structure of the Fuzzy Controller Membership Function 65
Figure IV-8 : Fuzzy PD Control 66
Figure IV-9 : Stator Power Response Using FPD-GWO Controller at Constant Wind Speed 66
Figure IV-10 : Stator Power Response Using FPD–GWO Controller at Variable Wind Speed 67
Figure IV-11 : Fuzzy PD+I-GWO Control 68
Figure IV-12 : Fuzzy PD+I Control 68
Figure IV-13 : Stator Power Response Using FPD+I-GWO Controller at Constant Wind Speed 69
Figure IV-14 : Stator Power Response Using FPD+I-GWO Controller at Variable Wind Speed 69
Figure IV-15 : ITAE-Based Performance Evaluation of the PI-GWO Controller 72
Figure IV-16 : PI-GWO Controller Gains Determined via Offline Optimization 72
Figure IV-17 : ITAE-Based Performance Evaluation of the FPD-GWO Controller 73
Figure IV-18 : FPD-GWO Controller Gains Determined via Offline Optimization 73
Figure IV-19 : ITAE-Based Performance Evaluation of the FPD+I-GWO Controller 74
Figure IV-20 : FPD+I-GWO Controller Gains Determined via Offline Optimization 74
Figure AP-1 : PI Controller 86

List of Table

Table I-1: Americas Installed Power Capacity by Country in 2025 8
Table I-2: Middle East and Africa Installed Power Capacity by Country in 2025 9
Table I-3: Asia Installed Power Capacity by Country in 2025 10
Table I-4: Europe Installed Power Capacity by Country in 2025 11
Table I-5: Wind power capacity in the top 10 countries in 2025 12
Table IV-1: Fuzzy Control Rules 65
Table IV-2: Performance Index of Active and Reactive Power 71
Table IV-3: Optimal Gains of Controllers 74

Abbreviation	Description
DFIG	Doubly-Fed Induction Generator
DFIM	Doubly-Fed Induction Machine
FLC	Fuzzy logic control
GSC	Grid Side Converter
GWO	Grey Wolf Optimizer
IGBT	Insulated Gate Bipolar Transistor
MSC	Machine Side Converter
MOSFET	Metal Oxid Semiconductor Field Effect Transistor
MPPT	Maximum Power Point Tracking
PI	Proportional–Integral
PWM	Pulse width modulation
SFOC	Stator Flux-Oriented Control
VOC	Vector-Oriented Control
WECS	Wind Energy Conversion System
WT	Wind Turbine

Electrical and Mechanical Variables

Symbol	Description
$T_{em}, T_{mec}, T_t, T_f$	Electromagnetic, mechanical, aerodynamic, turbine and viscous friction torque
Ω_t, Ω_g	Turbine, Generator speed
$I_{ds}, I_{qs}, I_{dr}, I_{qr}$	Stator and rotor currents in the d–q reference frame
V_s, V_r, I_s, I_r	Stator and rotor voltages and currents in the abc reference frame
$V_{ds}, V_{qs}, V_{dr}, V_{qr}$	Stator and rotor voltages in the d–q reference frame
Φ_s, Φ_r	Stator and rotor fluxes in the abc reference frame
$\Phi_{ds}, \Phi_{qs}, \Phi_{dr}, \Phi_{qr}$	Stator and rotor fluxes in the d–q reference frame
P_s, Q_s	Stator active and reactive powers
P_w	Wind power
R_s, R_r	Stator and rotor resistances

Symbol	Description
l_s , l_r	Stator and rotor inductances
l_m	Mutual inductance
l_{ms} , l_{mr}	Stator and rotor mutual inductances
l_{msr} , l_{mrs}	Stator–rotor and Rotor–stator mutual inductances
l_{max}	Maximum mutual inductance
J	Moment of inertia
f_r	Viscous friction coefficient
ω_s , ω_r , ω_m	Stator, rotor, and mechanical angular frequencies

Reference Frames and Transformations

Symbol	Description
a b c	Three-phase reference system
d q	d–q rotating reference frame
P(θ)	Park transformation

Wind Turbine and Aerodynamic Parameters

Symbol	Description
B	Pitch angle
λ	Tip speed ratio
λ_{opt}	Optimal tip speed ratio
C_p	Power coefficient
P	Air density
R	Blade radius
P_n	Rated turbine power
V_m	Maximum wind speed
Ω_t	Turbine mechanical speed
f	Turbine viscous friction coefficient

Converters and Control Parameters

Symbol	Description
C	DC bus capacitor
G	Gearbox ratio
K_p	Proportional gain
K_i	Integral gain
m	Modulation index
r	Modulation rate
U_c	Rectifier input voltage
T_s, T_r	Stator and Rotor time constants

General Mathematical Symbols

Symbol	Description
p	Number of pole pairs
P	Laplace operator
g	Slip

General Introduction

Electric energy is universally recognized as a cornerstone of modern civilization, playing a decisive role in enhancing living standards and fostering socio-economic development. The availability of electric energy has been demonstrated to have a direct influence on critical sectors, including healthcare, education, sanitation, transport, and industrial productivity. In recent decades, global electricity demand has increased substantially. This rise can be attributed to several factors, including accelerated industrialization, population growth, and the widespread use of electrical appliances. This continuous increase places significant pressure on existing energy infrastructures and calls for sustainable and reliable energy solutions [1, 2, 3].

Concurrently, the heavy reliance on conventional fossil fuels has raised serious concerns regarding resource depletion, environmental degradation, and climate change. Greenhouse gas emissions, particularly CO_2, are widely recognized as a major contributor to global warming. At the same time, concerns related to nuclear energy, particularly the management and safety of radioactive waste, remain unresolved challenges. These issues have forced governments, researchers, and industries worldwide to intensify efforts toward transitioning to more sustainable and cleaner energy systems [2, 3, 4, 5].

In this context, renewable energy sources such as solar, wind, hydropower, biomass, and geothermal energy are essential for fostering sustainable development. Among all energy sources, wind and solar have been growing the fastest and are poised to dominate the future energy mix, driven by their abundance, scalability, and steadily declining costs. The global transition toward low-carbon energy systems further emphasizes the strategic importance of integrating renewable resources into modern power grids. Projections indicate that these resources will account for a substantial share of electricity generation by mid-century [6, 7, 8].

Wind energy has attracted considerable attention due to its technological maturity, cost-effectiveness, and low environmental impact. Over the past decade, there has been a marked acceleration in the deployment of wind power installations worldwide, driven by advancements in turbine design, power electronics, and control systems, as well as supportive governmental policies. Consequently, wind energy has become one of the most rapidly expanding sources of electricity generation, contributing significantly to newly installed capacity and complementing conventional power plants [9, 10, 11].

Despite its many advantages, the sporadic and fluctuating characteristics of wind, pose significant technical challenges for power system operation. Variations in wind speed can lead to fluctuations in power output, reduced system inertia, and increased stress on grid stability and frequency control. Addressing these challenges requires advanced control strategies capable of

improving power quality, enhancing reliability, and facilitating the smooth integration of wind energy into the grid [12, 13].

Most modern wind energy conversion systems (WECS) use doubly fed induction generators (DFIGs) since they operate efficiently over a broad range of wind speeds. In DFIG-based configurations, the stator connects directly to the grid, while the rotor links through partially rated power electronic converters. This configuration enables independent control of active and reactive power, reduces converter cost, and enhances system flexibility. However, the nonlinear, multivariable, and strongly coupled dynamics of DFIG-based WECS, combined with external disturbances and parameter uncertainties, limit the effectiveness of conventional linear control techniques [14, 15, 16, 17].

Extensive research has been devoted to developing robust and optimal control strategies to address these limitations. Robust control techniques are crucial for ensuring system stability and maintaining acceptable performance in the presence of uncertainties, disturbances, and modeling inaccuracies. Meanwhile, optimal control strategies aim to maximize energy capture, improve power quality, reduce losses, and balance trade-offs between efficiency, mechanical stress, and grid support requirements. The integration of these approaches is therefore crucial for achieving high-performance and reliable operation of modern wind turbines [18 ،19].

Furthermore, intelligent control techniques, particularly fuzzy logic control (FLC), have been widely investigated as effective alternatives due to their ability to handle nonlinearities and uncertainties without requiring precise mathematical models. However, the design of fuzzy controllers leads to complex nonlinear optimization problems involving multiple parameters, such as membership functions, scaling factors, and controller gains [20, 21, 22, 23].

Metaheuristic optimization methods such as particle swarm optimization (PSO), genetic algorithms (GA), and ant lion optimizer (ALO) can assist in this process; however, they may suffer from slow convergence and the possibility of falling in local optima when dealing with high-dimensional search spaces [24, 25, 26, 27].

To overcome these challenges, this thesis proposes a hybrid Fuzzy PD+I controller for active and reactive power control in a DFIG-based WECS, with controller gains optimally tuned offline using the GWO algorithm. The purpose is to design a robust, fast, and accurate power controller capable of handling strong nonlinearities and varying wind conditions, outperforming conventional PI and basic fuzzy controllers while remaining suitable for real-time implementation.

The arrangement of the thesis is given as outlined below:

- The first chapter provides a comprehensive overview of wind energy fundamentals, covering both economic and technical aspects, as well as machine structure and operating modes.
- Chapter Two presents the modeling of variable-speed WECS components, including the DFIG in the d–q reference frame, the machine-side (MSC) and grid-side converters (GSC), and the WT, along with their associated control strategies.
- Chapter Three focuses on the theoretical foundations of the control methods applied to the wind energy system, in addition to the optimization techniques used to enhance their performance.
- Chapter Four presents the implementation of the proposed nonlinear control strategies and their optimization, along with a detailed analysis and discussion of the obtained Simulation Results.
- Finally, the general conclusion summarizes the main findings and outlines directions for future research.

Chapter I : Overview of Wind Energy Systems

I.1 Introduction

Wind power has established itself as a leading renewable energy source for sustainable electricity generation due to its abundance, environmental friendliness, and inexhaustible nature. In the last few decades, wind power technologies have undergone remarkable development, enabling large-scale deployment in both onshore and offshore applications. As a result, wind energy now represents the second-largest contributor to global renewable electricity generation after hydropower and is expected to play a dominant role in future low-carbon energy systems, in line with international emission reduction targets [28].

However, the inherent intermittency and stochastic nature of wind pose significant challenges to power quality, system stability, and grid integration. These challenges have motivated extensive research on WECSs, with a focus on improving energy capture efficiency, reducing capital and operational costs, enhancing reliability, and ensuring compliance with increasingly stringent grid codes. Consequently, the development of modern WECSs emphasizes variable-speed operation, advanced generator technologies, power electronic converters, and intelligent control strategies as key enablers for high-performance wind power generation [29].

This chapter presents a comprehensive overview of wind energy systems, addressing their fundamental principles, technical and economic aspects, in addition to the structural configuration of the doubly-fed induction machine, which has been selected as the generator in our wind power system, and their primary modes of operation.

I.2 Statistics on Scientific Production in Wind Energy

I.2.1 Wind Energy Publication Statistics in the IEEE Database

The growing global interest in alternative energy sources has prompted scientists and researchers to innovate and develop new approaches. This has resulted in the publication of thousands of research studies and scientific articles in this field. The research done in this area and published in the IEEE database is shown in Figure I-1 [30].

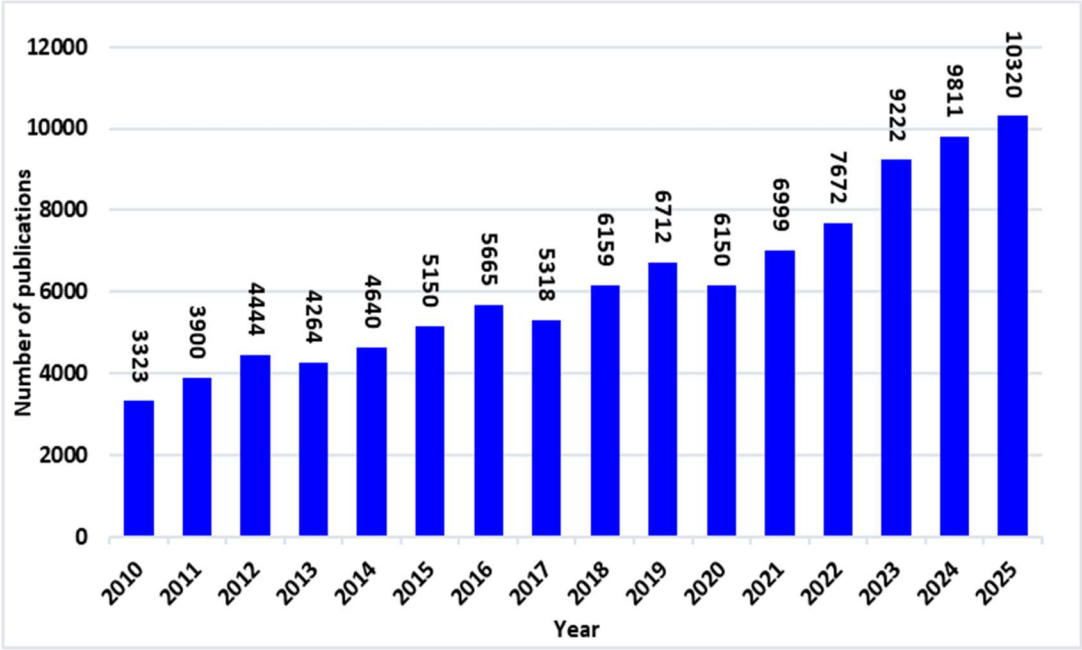

Figure I-1 : Wind Energy Publications in the IEEE Database [30]

I.2.2 Wind Energy Publication Statistics in the ScienceDirect Database

Research on the advancement and enhancement of wind energy use that has been published in the Direct Science database is displayed in Figure I-2 [31].

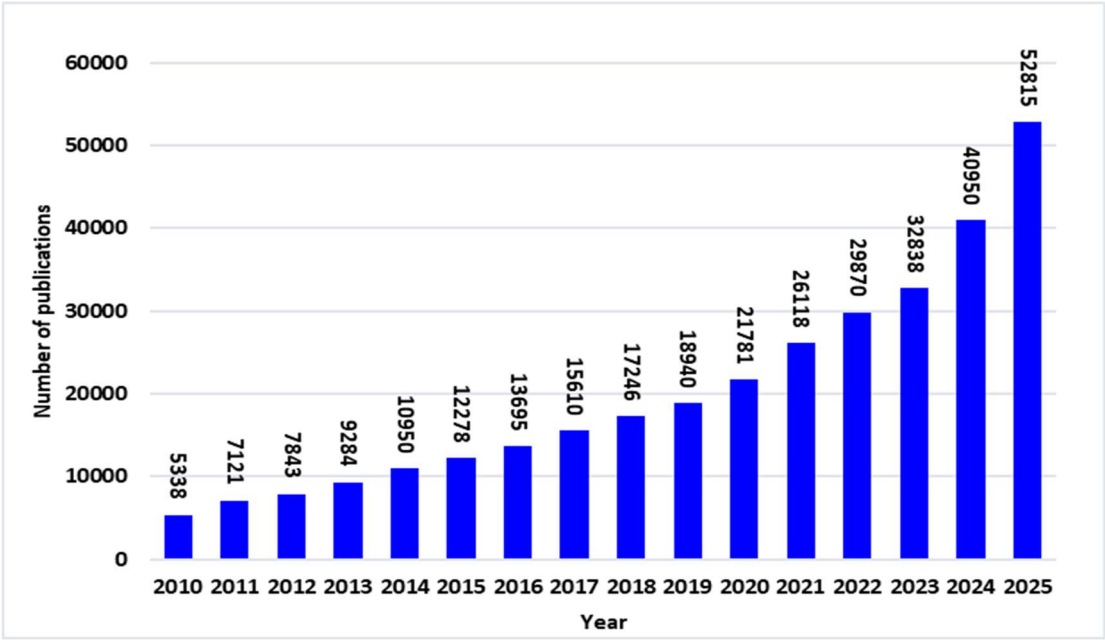

Figure I-2 : Wind Energy Publications in the ScienceDirect Database [31]

I.2.3 Wind Energy Publication Statistics in the Springer Nature Database

Figure I-3 displays studies that have been published in the Springer Nature database about the advancement and enhancement of wind energy utilization [32].

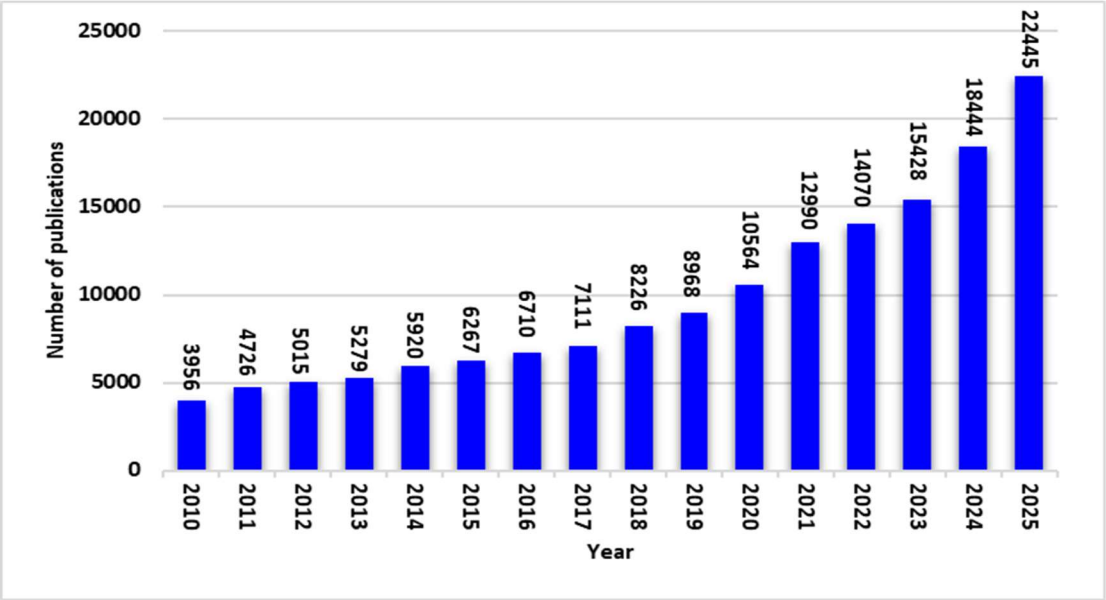

Figure I-3 : Wind Energy Publications in the Springer Nature Database [32]

I.3 Statistics on Wind Energy Installation and Production

Year **2025** was the best year yet for the wind industry, with **164.6 GW** of new wind power capacity added to the grid worldwide. This brings the total installed wind capacity to **1.299 TW**, which is a **14.34%** increase compared with last year [33].

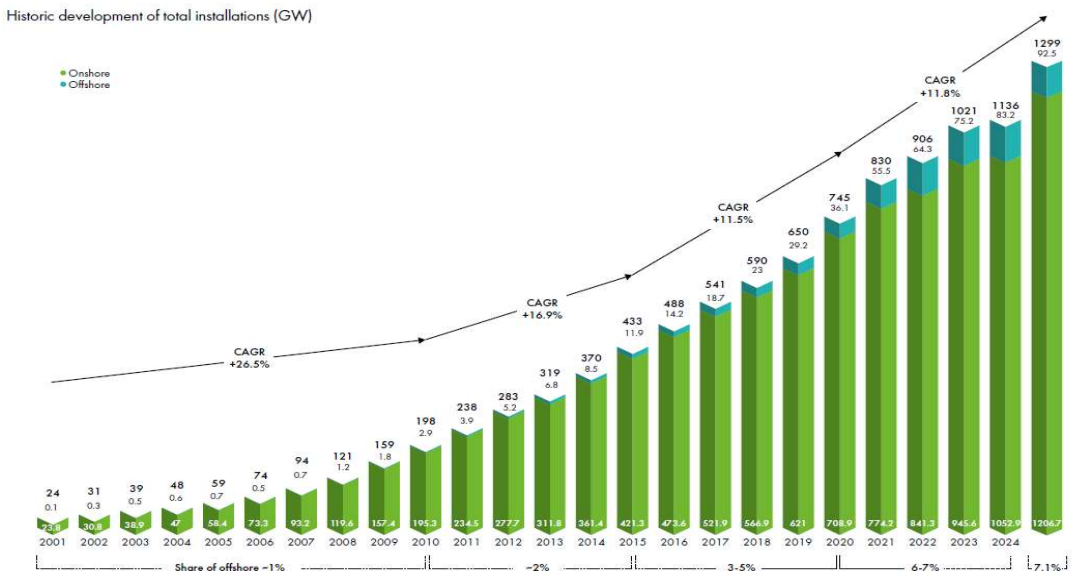

Figure I-4 : Global Growth of Wind Energy Installations (2001–2025) [33]

For the third consecutive year, new onshore wind installations surpassed the **100 GW** milestone, with **155.3 GW** connected to the grid in 2025 marking an all-time high. However, the **9.3 GW** of offshore wind capacity commissioned in 2025 was **16.25%** more than the previous year and the lowest since 2021 [33].

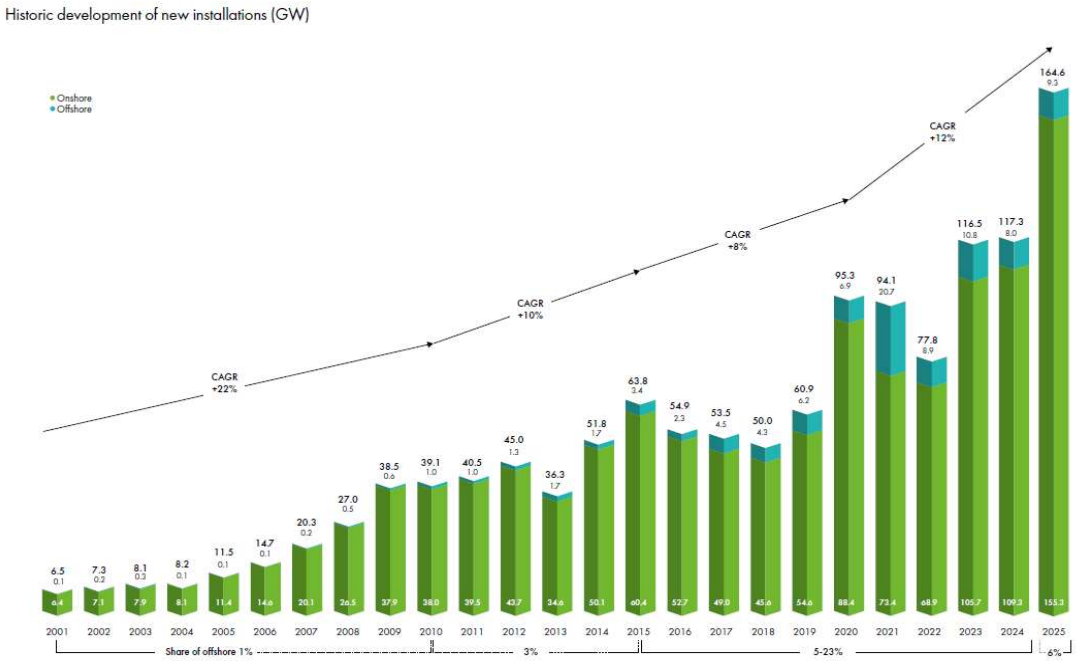

Figure I-5 : Evolution of Onshore and Offshore Wind Installations Worldwide [33]

I.3.1 Wind Energy Advancement in America

In terms of wind energy production in the Americas, the United States dominates the sector with a market share of around 70%, followed by Brazil and Canada, which have not made significant progress in the past year [33].

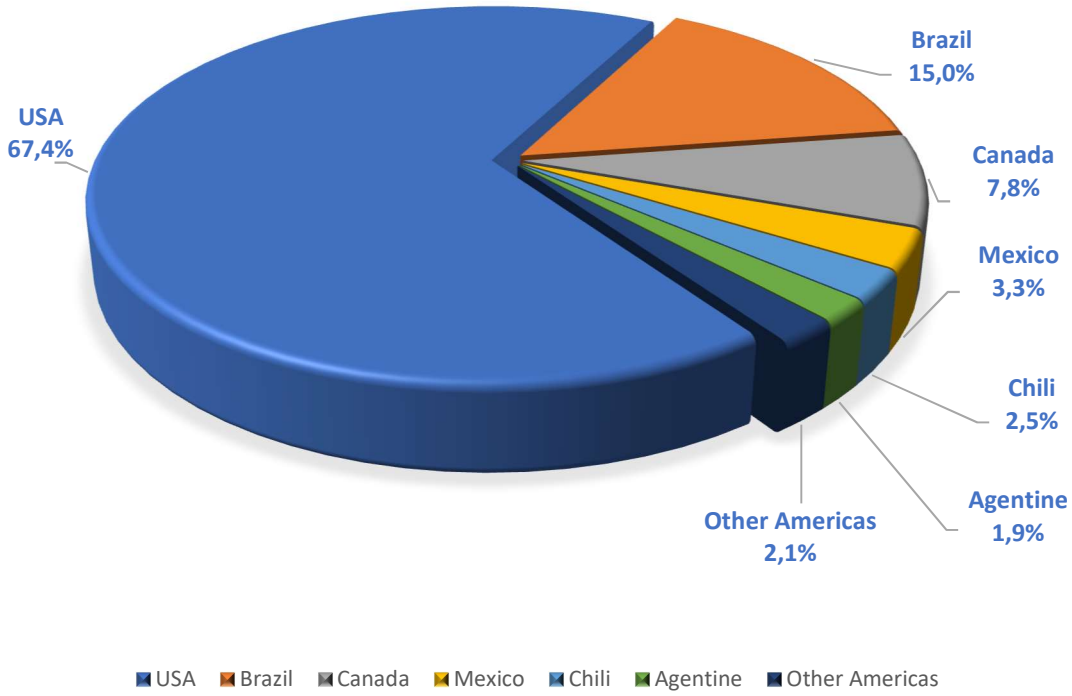

Figure I-6 : Wind Power Capacity in the Americas in 2025 [33]

Table I-1: Americas Installed Power Capacity by Country in 2025 [33]

Country	Year 2025
USA	161028
Canada	18665
Brazil	35980
Mexico	7812
Argentina	4495
Chile	6036
Rest of Americas	4923
Total power installed in GW	238939

I.3.2 Wind Energy Advancement in Africa and the Middle East

Interest in wind energy is growing in Africa and the Middle East, as evidenced by the example of South Africa. This interest has recently spread throughout the Arab world, encompassing nations such as Egypt—recognized as a pioneer in this sector—as well as Morocco and Saudi Arabia, which are also harnessing their natural resources. Furthermore, Kenya has recently shown a growing interest in this energy source [33].

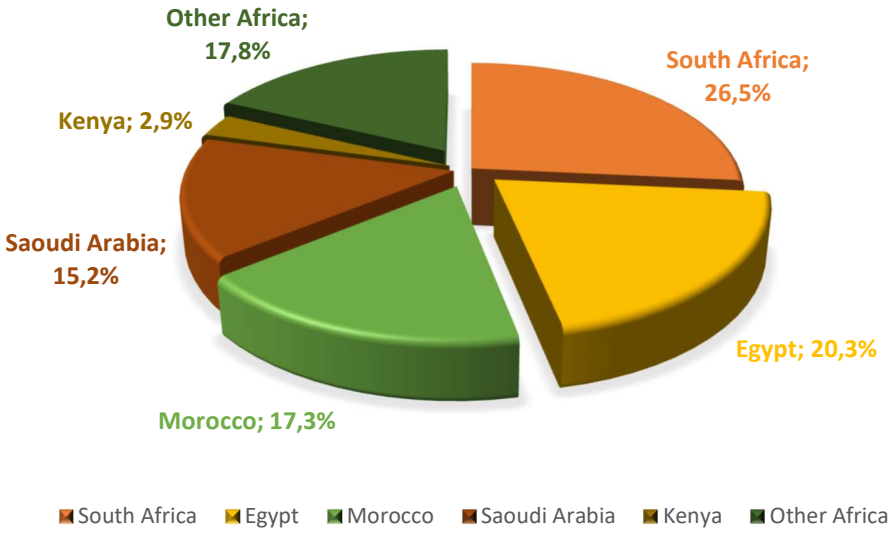

Figure I-7 : Wind Power Capacity in Africa and the Middle East in 2025 [33]

Table I-2: Middle East and Africa Installed Power Capacity by Country in 2025 [33]

Country	Year 2025
South Africa	4037
Egypt	3097
Morocco	2629
Saudi Arabia	2324
Kenya	436
Rest of Africa	2714
Total power installed in GW	15237

I.3.3 Wind Energy Advancement in Asia

The Asian continent accounts for approximately half of global wind energy production, primarily due to China's significant commitment to this sector and its high energy demand. This situation has motivated China to expand and diversify its energy resources while reducing its dependence on conventional energy sources. Interest in this field is also evident in India and Australia [33].

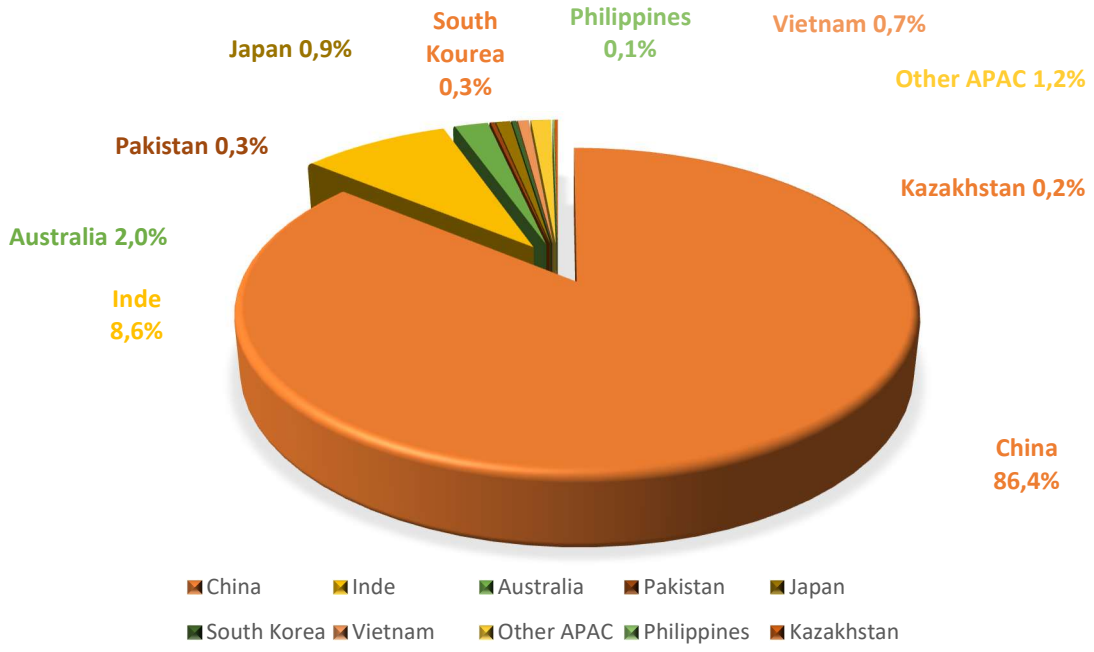

Figure I-8 : Wind Power Capacity in Asia in 2025 [33]

Table I-3: Asia Installed Power Capacity by Country in 2025 [33]

Country	Year 2025
China	592076
India	54511
Australia	13515
Japan	6148
Vietnam	4669
South Korea	2096
Pakistan	1894
Kazakhstan	1430
Philippines	681
Rest of APAC	8060
Total power installed in GW	685080

I.3.4 Wind Energy Advancement in Europe

Despite the variety of energy sources in Europe, the goal is to expand and diversify them, following the example of Germany, which places great emphasis on this sector. This is reflected in the significant amount of energy produced in this sector, as can be seen in France and Spain, which are also interested in this field [33].

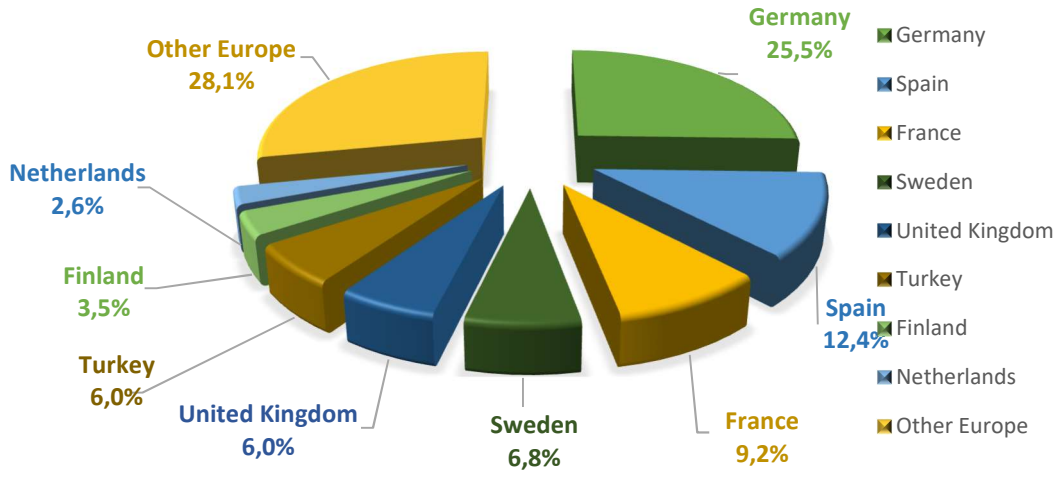

Figure I-9 : Wind Power Capacity in Europe in 2025 [33]

Table I-4: Europe Installed Power Capacity by Country in 2025 [33]

Country	Year 2025
Germany	68066
Spain	33151
France	24464
Sweden	18232
Turkey	15935
United Kingdom	15912
Finland	9433
Netherlands	7054
Rest of Europe	75188
Total power installed in GW	267435

I.4 Global Leaders in Wind Energy Installed Capacity and Market Share

In 2025, worldwide wind energy production surpassed the 1-Terawatt mark for the second time, marking a major milestone in the sector and reflecting the international community's growing interest in this form of energy. However, it should be noted that 80% of global production is concentrated in just 10 countries, highlighting the relative weakness of other countries in terms of production as well as their dependence on conventional energy sources [33].

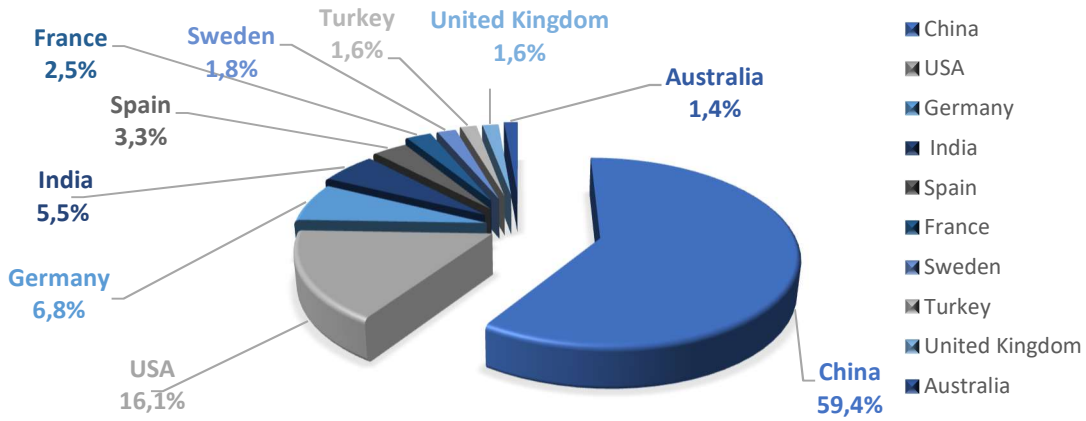

Figure I-10 : Breakdown of Wind Power in the Top 10 Countries in 2025 [33]

Table I-5: Wind power capacity in the top 10 countries in 2025 [33]

Country	Year 2025
China	592076
USA	161028
Germany	68066
India	54511
Spain	33151
France	24464
Sweden	18232
Turkey	15935
United Kingdom	15912
Australia	13515
Total power installed in GW	996890

I.5 Overview of the DFIM

The DFIM is seen as a crucial generator in renewable energy applications, especially within WECSs. Its key advantage is the ability to generate electrical energy at variable speeds, optimizing wind resource utilization and enhancing energy efficiency. This results in improved energy quality and quantity compared to fixed-speed generators. In operation, a converter is inserted between the rotor and the grid, managing power transfer from the stator to the grid, making DFIM suitable for high-power generation across diverse wind speeds [34].

I.5.1 Operation Description of the DFIM

I.5.1.1 DFIM Structure

The DFIM consists of a stator identical to synchronous and asynchronous machines, made of stacked laminations with windings. Its rotor features three windings connected in a star configuration to conductive slip rings, interacting with brushes during rotation, enabling efficient operation in various applications [35].

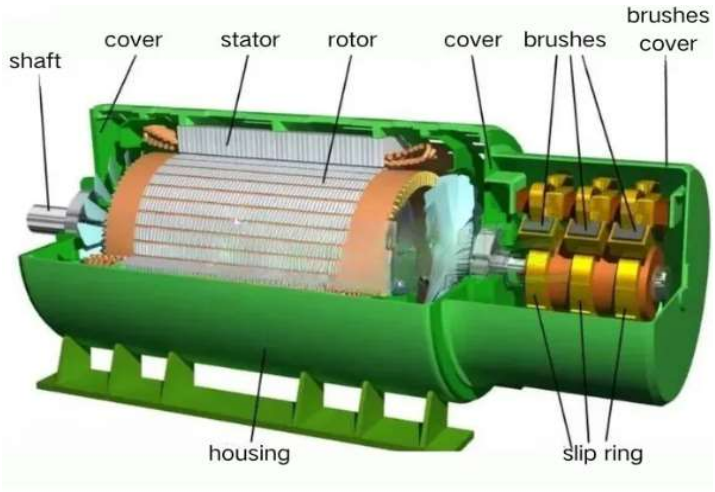

Figure I-11: DFIM Structure

I.5.1.2 Operation in Motor Mode

A DFIM is different from a traditional asynchronous machine, operating as a motor when running below synchronous speed and switching to a generator when running above it. In a DFIM, the operating mode is determined by the control of the rotor voltages. This control regulates the internal magnetic field, enabling operation in both sub-synchronous and super-synchronous regimes, whether in motor or generator mode. Consequently, the machine exhibits four distinct operating modes [36, 37].

- **Sub-Synchronous Motor Mode**

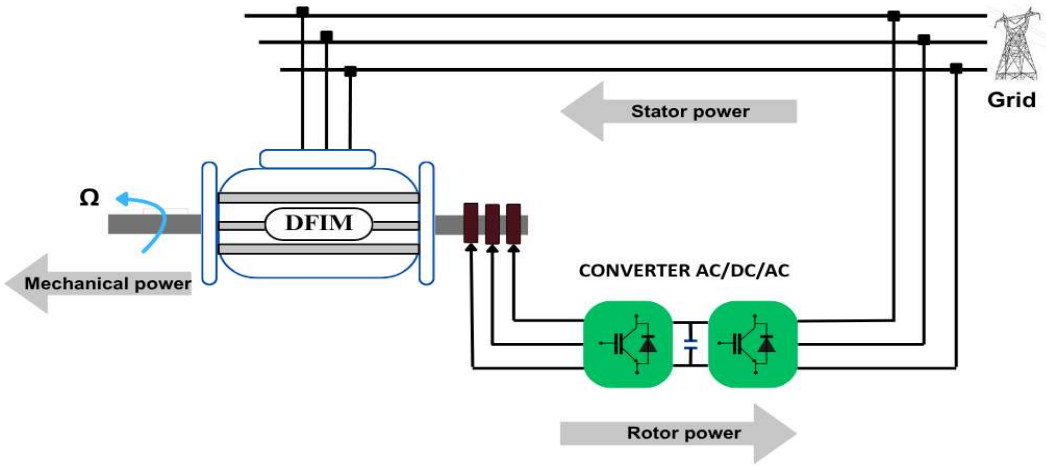

Figure I-12 : Operation in Sub-Synchronous Motor Mode

In this operating mode, the transmission of energy to the stator via the grid leads to the conversion of a portion of this energy into mechanical energy, while the other portion, called slip power, is reinjected into the grid via the rotor contacts. In this so-called situation, the DFIM operates in motor mode at a speed lower than synchronous speed [36, 37].

- **Super-Synchronous Motor Mode**

In this mode, the grid supplies power to the stator and rotor, the latter converting it into mechanical energy. The rotating magnetic field generated by the rotor windings is in opposite phase to that of the stator, allowing the induction motor to operate in motor mode beyond synchronous speed. This mode of operation is not possible for a conventional induction machine [36, 37].

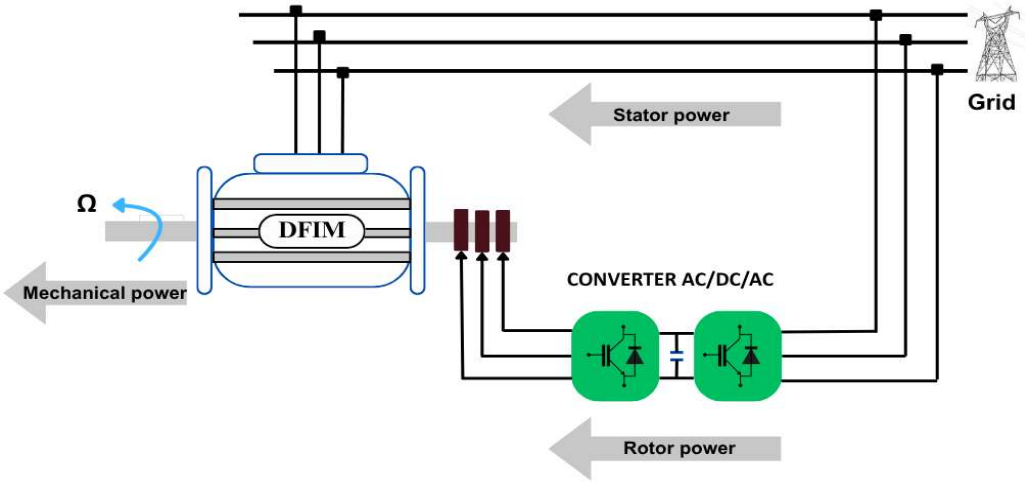

Figure I-13 : Operation in Super-Synchronous Motor Mode

I.5.1.3 Operation in Generator Mode

- **Sub-Synchronous Generator Mode**

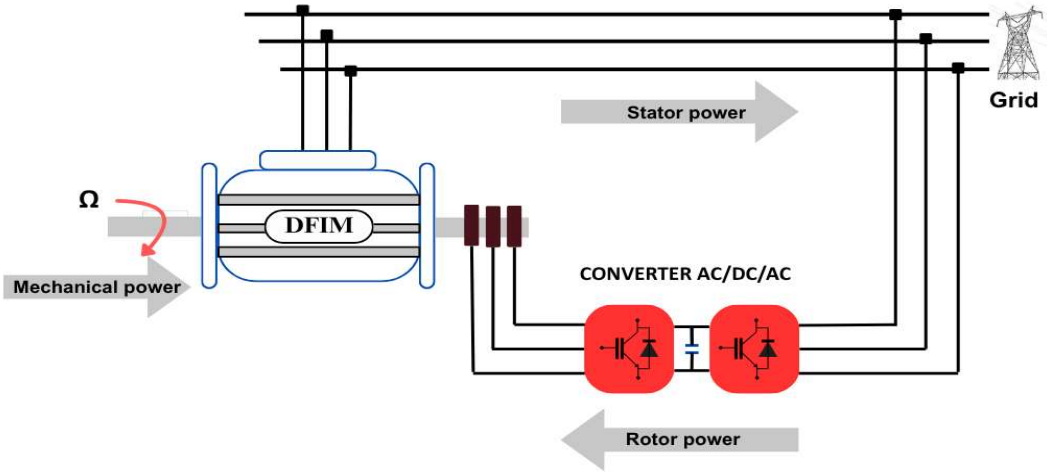

Figure I-14 : Operation in Sub-Synchronous Generator Mode

In this configuration, the conversion to electrical energy is done from the mechanical energy transmitted through the machine's shaft, which is then injected into the grid by the stator. A portion of this power is converted into slip power. The variable-frequency rotor circuit ensures a stable stator frequency, even in the event of rotational speed fluctuations. Furthermore, the

machine operates as a generator when its speed is below the synchronous speed. Operation in this mode is not feasible for a conventional asynchronous machine [19 ،37].

- **Super-Synchronous Generator Mode**

In this type of mode, the machine converts its mechanical energy into electrical energy, which is entirely injected into the grid via the stator. The slip power is extracted from the rotor to be reintegrated into the grid. The machine operates as a generator above synchronous speed. The traditional asynchronous machine can operate in this way; however, all the slip power is fully dissipated as Joule losses in the rotor [19 ،37].

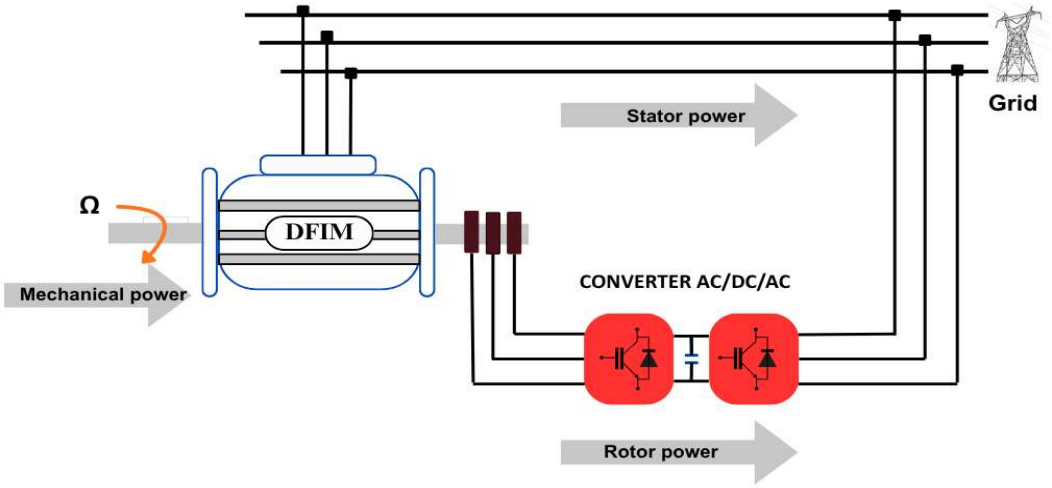

Figure I-15 : Operation in Super-Synchronous Generator Mode

I.5.2 Different Configurations of the DFIM

Like all AC electrical machines, the DFIM is capable of operating in both motor and generator modes. Each operating mode is defined by a specific configuration designed to satisfy a given criterion. In this section, the configurations most commonly reported in the literature for each mode of operation will be presented.

I.5.2.1 Configuration for Motor Mode

The speed variation of conventional synchronous and asynchronous machines requires changing the frequency of the stator currents through a rectifier followed by an inverter. Generally, these two converters are rated to handle the full nominal power of the machine. The use of a DFIM makes it possible to reduce the size of these converters by approximately 70%, by acting on the supply of the rotor windings [38].

Grid-Connected Stator with Machine-Side Inverter

This class is called simple DFIM. The stator windings are connected to the fixed three-phase grid, while the rotor is connected to its own inverter (Single Doubly Fed Induction Machine). This power supply mode is not suitable for operation at low rotor frequencies but the fact of connecting the stator to the grid and powering the rotor through an inverter makes it possible to size the converter on the machine side at 30% of the maximum mechanical power.

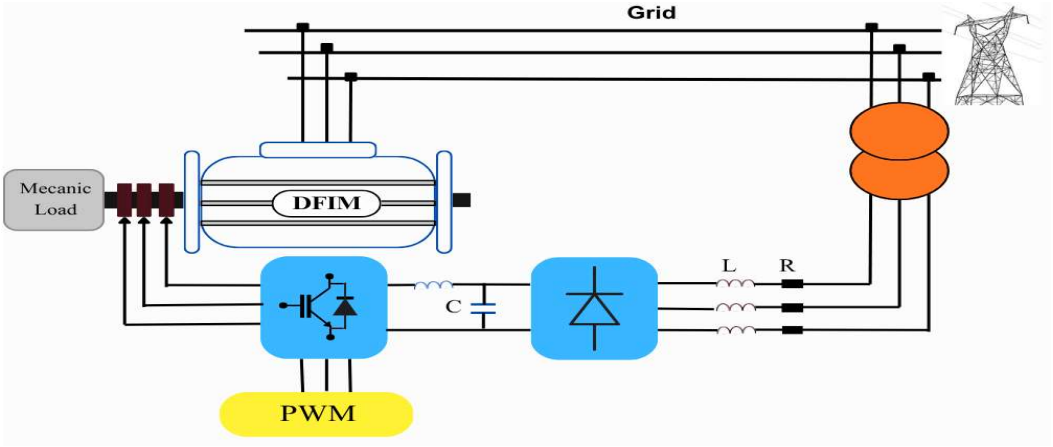

Figure I-16 : Diagram of the DFIM with Its Rotor Powered by an Inverter

Grid-Connected Stator with Machine-Side Cycloconverter

Replacing the rectifier-inverter combination with a cycloconverter allows a bidirectional flow of energy between the rotor and the grid. A cycloconverter works by taking portions of the sinusoidal grid voltages to create a lower frequency wave. However, this process produces significant harmonic disturbances that reduce the device's performance. With advancements in power electronics, cycloconverters have been largely replaced by systems using two controlled IGBT converters.

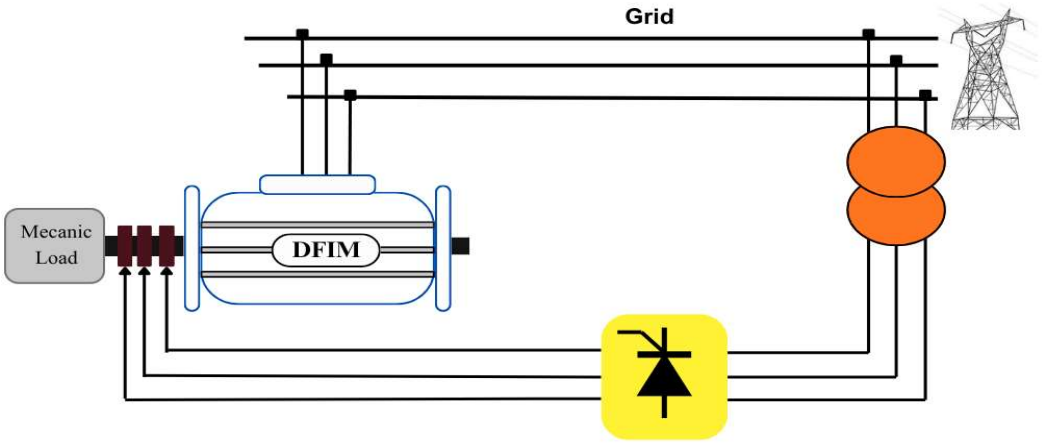

Figure I-17 : Diagram of the DFIM with Its Rotor Powered by a Cycloconverter

Dual-Converter-Fed DFIM Configuration

The structure contains several possible configurations, in which the stator and rotor can be powered in one of three ways: two cycloconverters; two inverters powered by their own rectifiers; or two inverters powered in parallel by a common rectifier. Owing to this type of power supply, the DFIM has four degrees of freedom, which makes its control very flexible. Consequently, the system enables the regulation of essential variables, including torque (speed), stator, rotor, and air-gap flux, slip, and power factor [39].

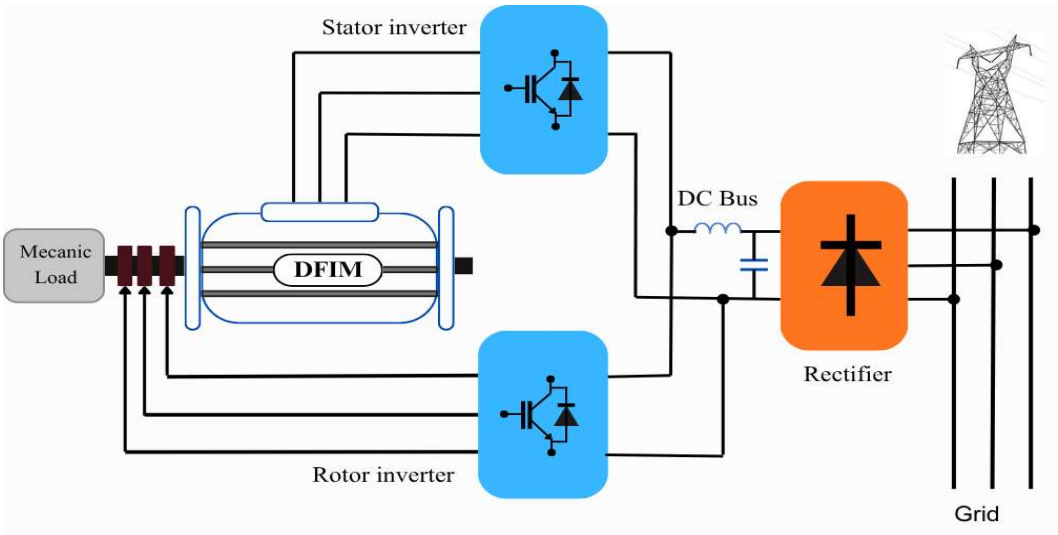

Figure I-18 : Block Diagram for Power Supply via Two Cycloconverters

I.5.2.2 Configuration for Generator Mode

This section looks at the wound-rotor DFIM and how it contributes in producing electrical energy from wind power.

Rotor Resistance Control Configuration

The stator is connected directly to the grid, while the rotor feeds into a rectifier with a resistive load on its output. Adding an IGBT-based chopper lets us control how much energy is dissipated in the rotor winding, allowing variable-speed operation while staying within the stable range of the asynchronous machine's torque/speed curve. This setup adjusts the slip based on the engine's rotation speed.

If the slip becomes significant, the power extracted from the rotor is high and it is entirely dissipated in the resistance, which harms the efficiency of the system [40].

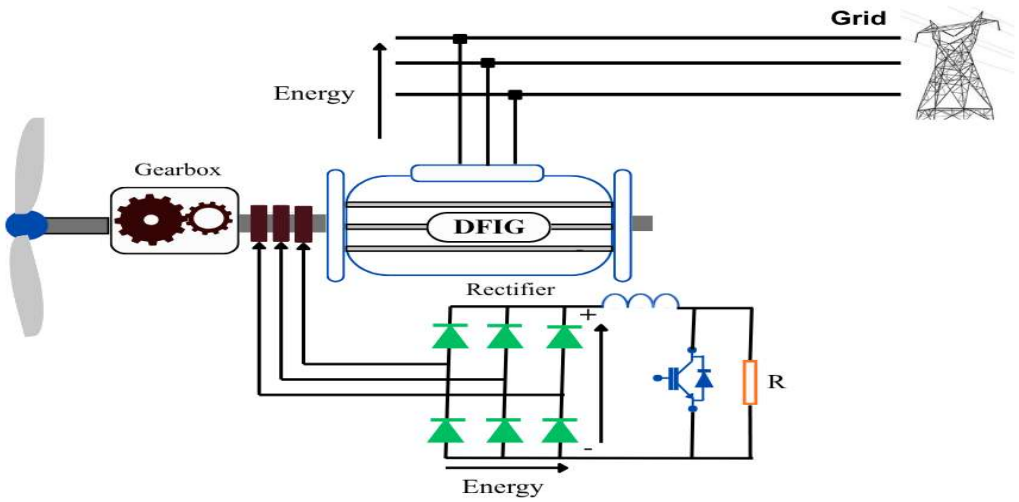

Figure I-19 : DFIM with Slip Control by Dissipated Energy

Kramer Slip Power Recovery Configuration

To enhance the design of the previous system and cut down on energy losses, the chopper and resistor are replaced with an inverter that feeds the slip energy back into the grid.

This configuration enables a reduction in the converter rating relative to the nominal power of the machine. The use of thyristor for the inverter harms the power factor, moreover the rectifier is unidirectional (transfer of energy only from the rotor of the machine to the grid). The system can only produce energy for rotation speeds higher than that of synchronism (Super- synchronous) [41, 40].

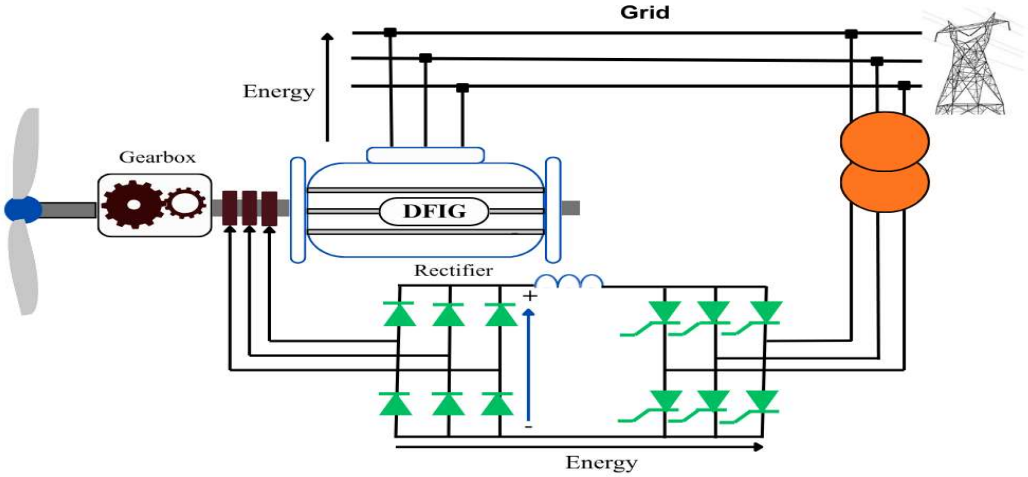

Figure I-20 : DFIM (Kramer Structure)

Cycloconverter-Based Scherbius Configuration

To facilitate reversible energy transfer between the rotor and the grid, the rectifier and inverter are replaced with a cycloconverter. This setup allows for a rotation speed range of roughly

±30% around synchronous speed. However, it also produces significant harmonic disturbances, which lower the device's power factor [40].

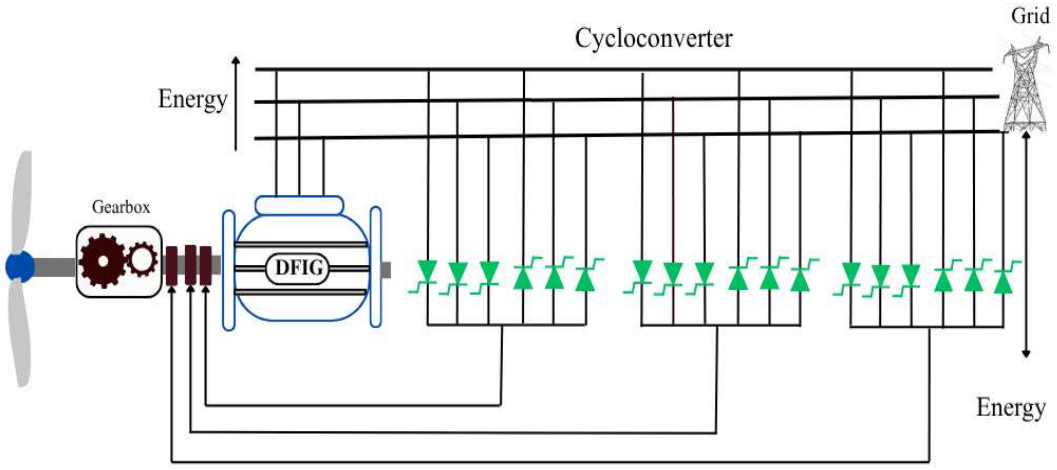

Figure I-21 : Scherbius Structure with Cycloconverter

PWM Converter-Based Scherbius Configuration

Advances in power electronics have made it possible to use switches like IGBTs, which can be precisely controlled for opening and closing at high switching frequencies. Converters based on these switches push the first harmonics toward higher frequencies, reducing harmonic disturbances and making filtering easier. The rotor converter's power reversibility enables both super- and sub-synchronous operation, as well as control of the grid-side power factor. When slip stays within ±30% of synchronism, the converters can be sized for just one-third of the machine's nominal power, with losses under 1% of that power. In super-synchronous mode, the stator and rotor can both feed energy into the grid, allowing the total output to surpass the machine's rated power while keeping a unit power factor [40].

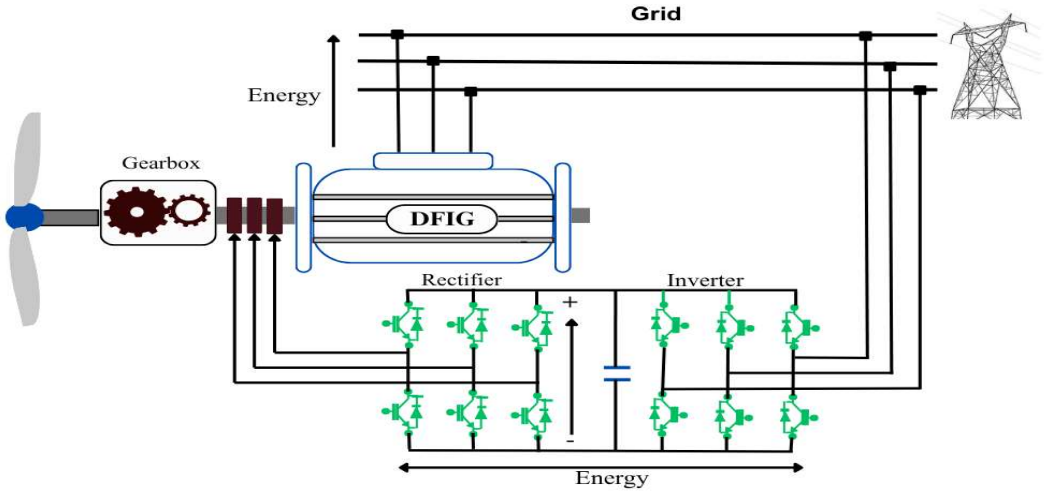

Figure I-22 : Scherbius Structure with PWM Converters

I.5.3 DFIM Applications

The DFIM finds application in multiple fields, functioning both as a motor and as a generator. The subsequent discussion presents the uses most often highlighted in the industry.

I.5.3.1 Motor Applications

The DFIM offers a modern approach for high-power drive systems, especially in applications needing a wide constant-power range and significant speed variation, including rolling mills, railway traction, and marine propulsion [42, 43]

I.5.3.2 Generator Applications

The DFIM is ideal for wind energy since it can operate efficiently over a wide range of speeds. By supplying the rotor circuit with a variable frequency, the stator voltage stays at a steady frequency and amplitude regardless of the shaft's speed. This makes it an excellent alternative to traditional synchronous machines in many decentralized energy setups, such as onboard power for ships or aircraft, hydraulic plants with varying flow and speed, wind or tidal turbines with fluctuating speeds, and generator sets that can slow down during low demand to save fuel [44, 45, 46].

I.5.4 Advantages and Disadvantages of the DFIM

The DFIM, often known as a generalized machine, is designed so its behavior can resemble that of a standard induction machine when the rotor windings are short-circuited, or that of a synchronous machine—though instead of a DC-excited salient pole or permanent magnet, it uses a three-phase winding powered by alternating current. This setup is also referred to as an "AC-excited synchronous machine".

I.5.4.1 Advantages of the DFIM

Access to the rotor enables control of its electrical variables, such as current and voltage, providing high flexibility and precise regulation of both electromagnetic torque and magnetic flux.

- The capability to operate at constant torque beyond the synchronous speed.
- A configuration in which the two converters supplying the machine allow operation under degraded conditions (if one of the inverters fails).
- In motor operation, using two converters lets the magnetizing current be shared between the two windings, while also splitting the mechanical power supplied to the load.

- Dual feeding reduces the size of the static converters, thereby lowering the machine's iron losses and improving its efficiency.
- Bidirectional transfer of rotor power.
- Operation below or above synchronous speed provides a broad range of speed changes.

The DFIM combines the advantages of both synchronous and asynchronous machines, namely:

- Variable-speed operation.
- Decoupled control of active and reactive power [47, 48].

I.5.4.2 Disadvantages of the DFIM

- The machine is larger than a standard induction machine, typically longer because of the brushes.
- It involves the use of a greater number of static converters than a conventional machine.
- Its total cost is higher in comparison with other electrical machines [49].

I.6 Conclusion

This chapter presents a comprehensive review of the state-of-the-art developments in WECSs, begins by describing the scientific and commercial statistics in this field, as well as providing a descriptive overview of the state of the art regarding the double-fed asynchronous machine, which has been selected as the generator in our wind power system and will be the subject of this study. A description of its structure, operating modes, power supply configurations and its applications as both a motor and a generator are presented. The remainder of this work is primarily devoted to the modelling and control of this system.

Chapter II : Wind Energy Conversion System Modeling

II.1 Introduction

Comprehending the operation of any system can be challenging, as it requires a thorough understanding of its underlying model to accurately predict its behavior under various operating conditions through simulation. Therefore, the availability of a precise mathematical model that faithfully represents the system's real-world dynamics is of paramount importance [50, 51].

A WECS typically consists of a wind turbine, a doubly-fed induction generator (DFIG), a direct current (DC) bus, and two static power converters. The wind turbine (WT) incorporates a gearbox (speed multiplier) to adapt the low rotational speed of the turbine to the higher speed required by the generator, enabling operation over a range of wind velocities [52]. In this configuration, the stator of the DFIG is directly connected to the electrical grid, while the rotor is interfaced through two back-to-back bidirectional power converters linked via a DC bus [53].

This chapter focuses on the modeling of the WECS components to describe the process of converting wind kinetic energy into electrical energy. It begins with the aerodynamic modeling of the wind turbine, followed by the modeling of the mechanical drive train and the electrical behavior of the DFIG.

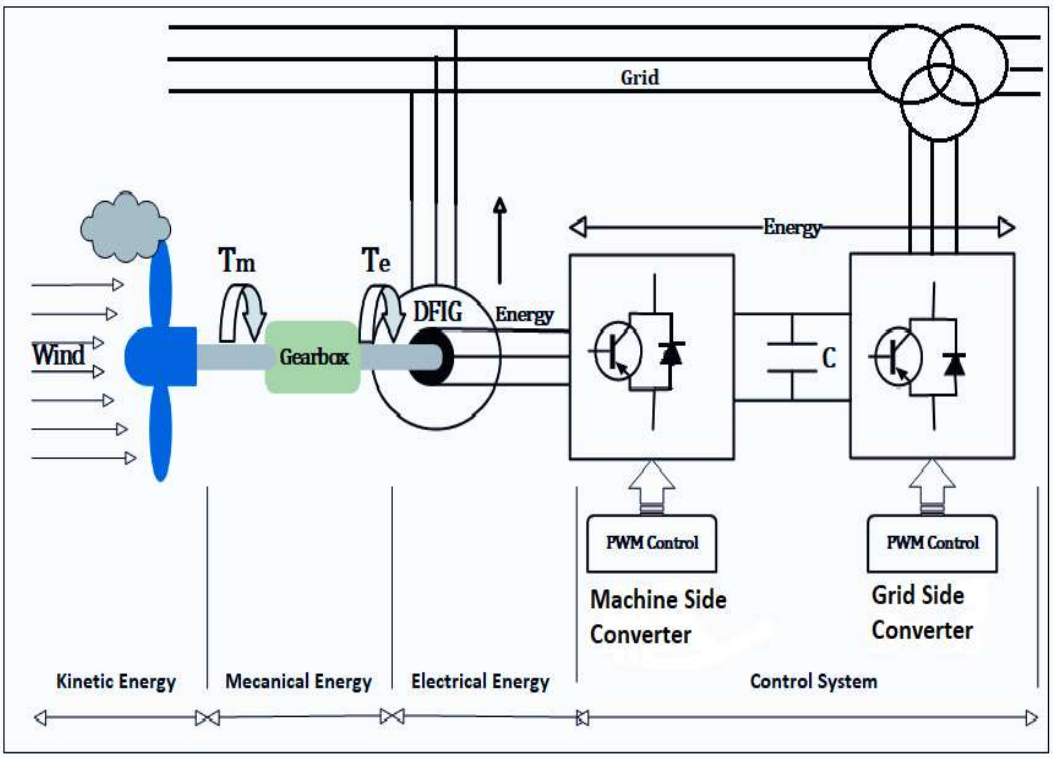

Figure II-1 : WECS Block Diagram

II.2 DFIM Modeling

The DFIM is a conventional induction machine with an accessible rotor winding similar to that of the stator. Consequently, its mathematical model is identical to that of a squirrel-cage induction machine, except for the presence of non-zero rotor voltages [54, 55].

II.2.1 Simplifying Assumptions

To facilitate the analysis of the machine, the following assumptions are made [56, 57]:

- The machine exhibits perfect structural symmetry;
- The air gap is of uniform thickness;
- Skin and slotting (notching) effects are neglected;
- The stator and rotor have the same number of phases;
- Ferromagnetic losses are negligible;
- Magnetic saturation is neglected;
- The magnetomotive forces in the air gap have a sinusoidal spatial distribution;
- The resistances of the machine windings are assumed constant.

II.2.2 Mathematical Equations of the DFIM in (a b c) System

Figure II-2 illustrates the schematic of a DFIM in the three-phase reference frame [58].

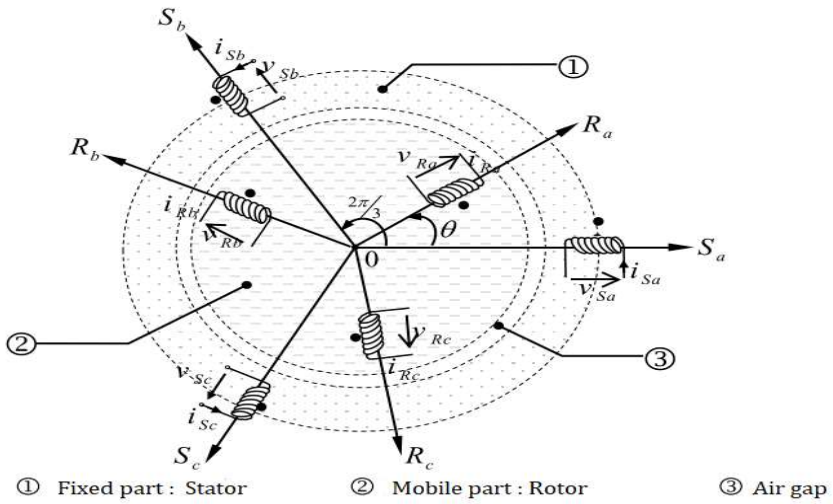

Figure II-2 : DFIM Representation in the Three-Phase Reference Frame

II.2.2.1 Electrical Equations

Each winding of the Doubly-Fed Induction Machine (DFIM) can be represented by an equivalent electrical circuit. The stator circuit is typically modeled as a series combination of a

resistance and an inductance. According to ***Faraday***'s law, the induced electromotive force (EMF) across the inductance is directly related to the time variation of the magnetic flux linkage, establishing the fundamental relationship between voltage and flux in the machine [51, 52].

$$-e = \frac{\mathrm{d}\Phi}{\mathrm{dt}} \qquad \mathrm{II}-1$$

The application of the mesh law to this circuit gives:

$$-e = \frac{\mathrm{d}\Phi_{sa}}{\mathrm{dt}} = V_{sa} - R_s I_{sa} \qquad \mathrm{II}-2$$

Based on the previous assumptions, and by employing ***Kirchhoff***'s law to the three stator and rotor windings, the equations are expressed in matrix form as follows:

Stator equations:

$$\begin{bmatrix} V_{sa} \\ V_{sb} \\ V_{sc} \end{bmatrix} = \frac{d}{dt}\begin{bmatrix} \Phi_{sa} \\ \Phi_{sb} \\ \Phi_{sc} \end{bmatrix} + \begin{bmatrix} R_s & 0 & 0 \\ 0 & R_s & 0 \\ 0 & 0 & R_s \end{bmatrix}\begin{bmatrix} I_{sa} \\ I_{sb} \\ I_{sc} \end{bmatrix} \qquad \mathrm{II}-3$$

Rotor equations:

$$\begin{bmatrix} V_{ra} \\ V_{rb} \\ V_{rc} \end{bmatrix} = \frac{d}{dt}\begin{bmatrix} \Phi_{ra} \\ \Phi_{rb} \\ \Phi_{rc} \end{bmatrix} + \begin{bmatrix} R_r & 0 & 0 \\ 0 & R_r & 0 \\ 0 & 0 & R_r \end{bmatrix}\begin{bmatrix} I_{ra} \\ I_{rb} \\ I_{rc} \end{bmatrix} \qquad \mathrm{II}-4$$

II.2.2.2 Magnetic Equations

The equations of stator and rotor flux respectively are as follows:

$$\begin{bmatrix} \Phi_{sa} \\ \Phi_{sb} \\ \Phi_{sc} \end{bmatrix} = \begin{bmatrix} l_s & l_{ms} & l_{ms} \\ l_{ms} & l_s & l_{ms} \\ l_{ms} & l_{ms} & l_s \end{bmatrix}\begin{bmatrix} I_{sa} \\ I_{sb} \\ I_{sc} \end{bmatrix} + [l_{msr}]\begin{bmatrix} I_{ra} \\ I_{rb} \\ I_{rc} \end{bmatrix} \qquad \mathrm{II}-5$$

And

$$\begin{bmatrix} \Phi_{ra} \\ \Phi_{rb} \\ \Phi_{rc} \end{bmatrix} = \begin{bmatrix} l_r & l_{mr} & l_{mr} \\ l_{mr} & l_r & l_{mr} \\ l_{mr} & l_{mr} & l_r \end{bmatrix}\begin{bmatrix} I_{ra} \\ I_{rb} \\ I_{rc} \end{bmatrix} + [l_{mrs}]\begin{bmatrix} I_{sa} \\ I_{sb} \\ I_{sc} \end{bmatrix} \qquad \mathrm{II}-6$$

$$[l_{msr}] = [l_{mrs}]^T = l_{max}\begin{bmatrix} \cos(\theta) & \cos\left(\theta + \frac{2\pi}{3}\right) & \cos\left(\theta - \frac{2\pi}{3}\right) \\ \cos\left(\theta - \frac{2\pi}{3}\right) & \cos(\theta) & \cos\left(\theta + \frac{2\pi}{3}\right) \\ \cos\left(\theta + \frac{2\pi}{3}\right) & \cos\left(\theta - \frac{2\pi}{3}\right) & \cos(\theta) \end{bmatrix} \qquad \mathrm{II}-7$$

Where:

l_s & l_r are the self-inductances of the stator and rotor phases, respectively.

l_{ms} & l_{mr} are the mutual inductances between the stator and rotor phases, respectively.

l_{msr} is the mutual inductance matrix, also known as the stator-rotor coupling matrix, defined by:

l_{max} is the maximum mutual inductance between a stator phase and a rotor phase.

II.2.2.3 Mechanical Equations

The mechanical dynamics of the DFIM are governed by the following equation:

$$T_{em} = T_r + f_r.\Omega + J.\frac{d\Omega}{dt} \qquad \text{II} - 8$$

II.2.3 Park Transformation

An asynchronous (induction) machine exhibits strong coupling among its electrical and magnetic variables, which makes its representation in the three-phase (a b c) system relatively complex. To accurately predict its behavior while maintaining analytical tractability, it is advantageous to adopt a modeling approach that balances precision and simplicity. The Park transformation provides an effective mathematical tool for this purpose by converting a three-phase system into an equivalent two-axis representation. This transformation maps the variables from the (a b c) frame to either a stationary orthogonal frame (α-β) or a rotating reference frame (d–q). The (α-β) frame remains fixed with respect to the stator, whereas the (d-q) frame rotates at an angular position θ relative to the stationary frame, commonly referred to as the Park angle [51, 52, 54].

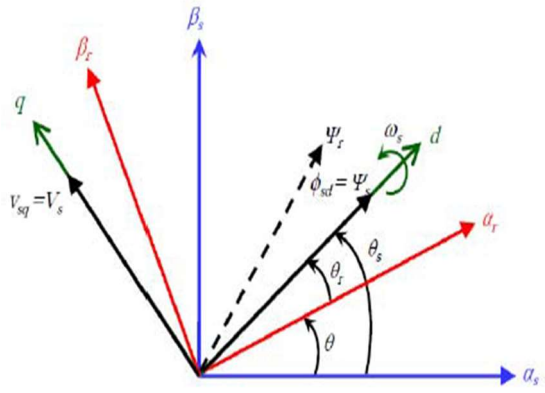

Figure II-3 : Park Reference Orientation

The transformation matrix P(θ) preserves power when converting from three phases to two phases and is defined as follows.

$$\begin{bmatrix} x_d \\ x_q \\ x_0 \end{bmatrix} = P(\theta) \begin{bmatrix} x_a \\ x_b \\ x_c \end{bmatrix} \qquad \text{II} - 9$$

The new model is formed by multiplying the equations for tensions, currents, and fluxes with the Park matrix, defined as

$$P(\theta) = \sqrt{\frac{2}{3}}. \begin{bmatrix} \cos(\theta) & \cos\left(\theta - \frac{2\pi}{3}\right) & \cos\left(\theta - \frac{4\pi}{3}\right) \\ -\sin(\theta) & -\sin\left(\theta - \frac{2\pi}{3}\right) & -\sin\left(\theta - \frac{4\pi}{3}\right) \\ \frac{1}{\sqrt{2}} & \frac{1}{\sqrt{2}} & \frac{1}{\sqrt{2}} \end{bmatrix} \qquad \text{II} - 10$$

The inverse transformation is defined by:

$$\begin{bmatrix} x_a \\ x_b \\ x_c \end{bmatrix} = P^{-1}(\theta) \begin{bmatrix} x_d \\ x_q \\ x_0 \end{bmatrix} \qquad \text{II} - 11$$

The inverse Park transformation matrix is defined by:

$$P^{-1}(\theta) = \sqrt{\frac{2}{3}}. \begin{bmatrix} \cos(\theta) & -sin(\theta) & \frac{1}{\sqrt{2}} \\ cos\left(\theta - \frac{2\pi}{3}\right) & -\sin\left(\theta - \frac{2\pi}{3}\right) & \frac{1}{\sqrt{2}} \\ cos\left(\theta - \frac{4\pi}{3}\right) & -sin\left(\theta - \frac{4\pi}{3}\right) & \frac{1}{\sqrt{2}} \end{bmatrix} \qquad \text{II} - 12$$

$P(\theta)$and $P^{-1}(\theta)$ refer to Park's transition matrix and its inverse, respectively.

II.2.4 Mathematical Equations of the DFIM in (d–q) System

II.2.4.1 Electrical Equations

Hence, the general electrical model of the asynchronous machine, obtained through the Park transformation, is expressed by the stator and rotor equations [59, 60].

Stator and rotor tensions:

$$\begin{cases} V_{ds} = R_s I_{ds} + \frac{d}{dt}\phi_{ds} - \omega_s \phi_{qs} \\ V_{qs} = R_s I_{qs} + \frac{d}{dt}\phi_{qs} + \omega_s \phi_{ds} \\ V_{dr} = R_r I_{dr} + \frac{d}{dt}\phi_{dr} - \omega_r \phi_{qr} \\ V_{qr} = R_r I_{qr} + \frac{d}{dt}\phi_{qr} + \omega_r \phi_{dr} \end{cases} \qquad \text{II} - 13$$

II.2.4.2 Magnetic Equations

The fluxes of the stator and the rotor

$$\begin{cases} \phi_{ds} = l_s I_{ds} + l_m I_{dr} \\ \phi_{qs} = l_s I_{qs} + l_m I_{qr} \\ \phi_{dr} = l_r I_{dr} + l_m I_{ds} \\ \phi_{qr} = l_r I_{qr} + l_m I_{qs} \end{cases} \quad \text{II} - 14$$

II.2.4.3 Mechanical Equations

The electromagnetic torque is defined by:

$$T_{em} = p\frac{l_m}{l_s}(\phi_{ds} I_{qr} - \phi_{qs} I_{dr}) \quad \text{II} - 15$$

II.2.5 Reference Frame Selection

A reference frame aligned with the rotating magnetic field is adopted owing to its advantages. This frame, known as the synchronous rotating reference frame, operates at synchronous angular speed. Under this representation, the relative components of the machine remain constant, which explains its widespread use in the control of asynchronous machines: The relationship between the electrical angular positions is expressed as [61]:

$$\frac{d\theta_s}{dt} = \frac{d\theta_r}{dt} + \frac{d\theta}{dt} = \omega_s = \omega_r + \omega \quad \text{II} - 16$$

II.2.6 State-Space Representation of the DFIM Model

The dynamic model of the DFIM is given by the following state-space equation:

$$[\dot{X}] = [A].[X] + [B].[U] \quad \text{II} - 17$$

With $[X] = [\phi_{ds}\ \phi_{qs}\ i_{dr}\ i_{qr}]^T$; $[U] = [V_{ds}\ V_{qs}\ V_{dr}\ V_{qr}]^T$ II − 18

$$[A] = \begin{bmatrix} -\frac{1}{T_s} & \omega_s & \frac{l_m}{T_s} & 0 \\ -\omega_s & -\frac{1}{T_s} & 0 & \frac{l_m}{T_s} \\ \alpha & -\beta(\omega_s - \omega_r) & -\delta & \omega_r \\ \beta(\omega_s - \omega_r) & \alpha & -\omega_r & -\delta \end{bmatrix} [B] = \begin{bmatrix} 1 & 0 & 0 & 0 \\ 0 & 1 & 0 & 0 \\ -\frac{l_m}{\sigma l_r l_s} & 0 & \frac{1}{\sigma l_r} & 0 \\ 0 & -\frac{l_m}{\sigma l_r l_s} & 0 & \frac{1}{\sigma l_r} \end{bmatrix} \quad \text{II} - 19$$

α, β, and δ are constants represented as follows:

$$\alpha = \frac{l_m}{\sigma T_s l_s l_r}; \qquad \beta = \frac{l_m}{\sigma l_s l_r}; \qquad \delta = \frac{1}{\sigma}\left(\frac{1}{T_r} + \frac{{l_m}^2}{T_s l_s l_r}\right) \quad \text{II} - 20$$

In order to facilitate the simulation, the matrix [A] is decomposed as follows:

$$[A] = [A_1] + \omega_s.[A_2] + \omega_r.[A_3] \qquad \text{II} - 21$$

$$[A_1] = \begin{bmatrix} -\frac{1}{T_s} & 0 & \frac{l_m}{T_s} & 0 \\ 0 & -\frac{1}{T_s} & 0 & \frac{l_m}{T_s} \\ \alpha & 0 & -\delta & 0 \\ 0 & \alpha & 0 & -\delta \end{bmatrix}, [A_2] = \begin{bmatrix} 0 & 1 & 0 & 0 \\ -1 & 0 & 0 & 0 \\ \alpha & -\beta & 0 & 0 \\ \beta & \alpha & 0 & 0 \end{bmatrix}, [A_3] = \begin{bmatrix} 0 & 0 & 0 & 0 \\ 0 & 0 & 0 & 0 \\ \alpha & \beta & 0 & 1 \\ -\beta & \alpha & -1 & 0 \end{bmatrix} \quad \text{II} - 22$$

II.3 Machine Side Converter Modeling and Control

WECSs based on a DFIM require a power electronic converter to supply the rotor of the machine. This converter primarily functions as a controlled interface between the DC bus and the rotor windings, enabling the regulation of rotor currents. In addition, it allows the implementation of control strategies to manage the active and reactive power generated by the stator and ensures their proper injection into the grid.

II.3.1 Machine Side Converter Modeling

The rotor of the DFIM is supplied by a two-level voltage source inverter using semiconductor devices like MOSFETs or IGBTs, each with anti-parallel diodes, forming six bidirectional switching arms. These switches work in complementary pairs to maintain continuous phase currents and avoid short circuits. Assuming the six switches in Figure II-4(a) are ideal, and replacing each transistor–diode pair with an equivalent switch k_i (where i = 1, 2, 3, 4, 5, 6), the simplified converter layout is shown in Figure II-4(b) [19, 20, 62].

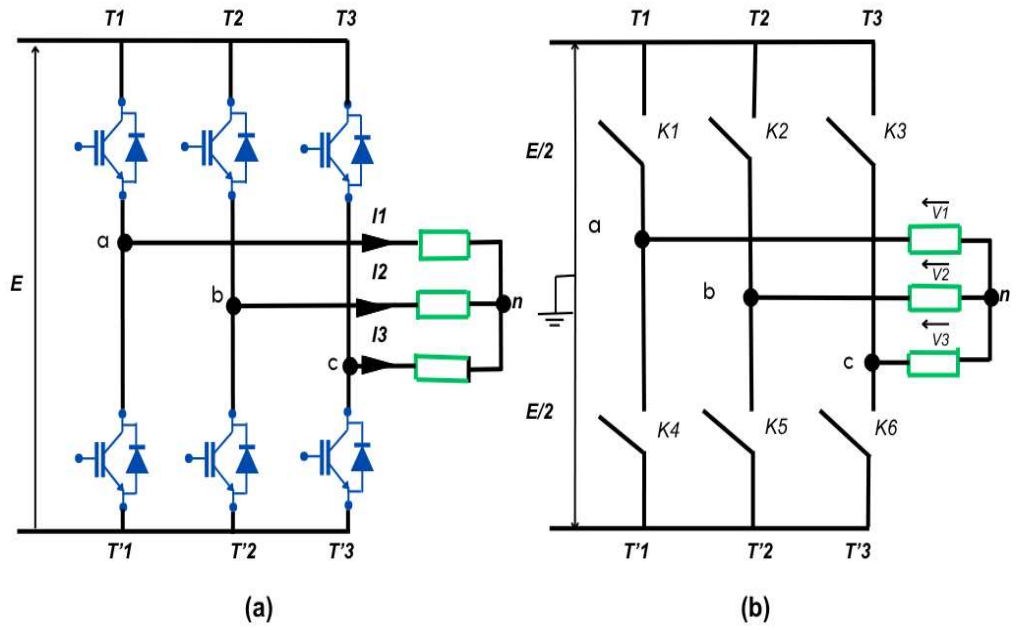

Figure II-4 : Simplified Diagram of a Two-Level Three-Phase Inverter

To simplify the study, a star connection without a neutral blocks third-order harmonic and their multiples, while keeping the three-phase system perfectly balanced at the inverter's output.

The basic voltage equations for the three phases are written as:

$$\begin{cases} V_a = V_{ao} + V_{on} \\ V_b = V_{bo} + V_{on} \\ V_c = V_{co} + V_{on} \end{cases} \quad \text{II} - 23$$

Moreover, one has:

$$V_a + V_b + V_c = V_{ao} + V_{bo} + V_{co} + 3.V_{on} \quad \text{II} - 24$$

Let's assume the stator's three-phase voltage system is perfectly symmetrical.

Then:

$$V_{ao} + V_{bo} + V_{co} + 3.V_{on} = 0 \quad \text{II} - 25$$

So:

$$V_{on} = \frac{1}{3}(V_{ao} + V_{bo} + V_{co}) \quad \text{II} - 26$$

Substituting Equation II-26 into II-23 gives us the following system:

$$\begin{cases} V_a = \frac{2}{3}V_{ao} - \frac{1}{3}V_{bo} - \frac{1}{3}V_{co} \\ V_b = -\frac{1}{3}V_{ao} + \frac{2}{3}V_{bo} - \frac{1}{3}V_{co} \\ V_c = -\frac{1}{3}V_{ao} - \frac{1}{3}V_{bo} + \frac{2}{3}V_{co} \end{cases} \quad \text{II} - 27$$

The system Equations II-27 can be rewritten in the following matrix form:

$$\begin{bmatrix} V_a \\ V_b \\ V_c \end{bmatrix} = \frac{1}{3}\begin{bmatrix} 2 & -1 & -1 \\ -1 & 2 & -1 \\ -1 & -1 & 2 \end{bmatrix}\begin{bmatrix} V_{ao} \\ V_{bo} \\ V_{co} \end{bmatrix} \quad \text{II} - 28$$

By rapidly switching on and off, the inverter generates an alternating voltage composed of a series of rectangular pulses.

$$\begin{cases} V_{ao} = \frac{E}{2}S_1 \\ V_{bo} = \frac{E}{2}S_2 \\ V_{co} = \frac{E}{2}S_3 \end{cases} \quad \text{II} - 29$$

Such as

$$\begin{cases} S_1 = 1 & if & K_1\ closed & Else & S_1 = -1 & if & K_1\ open \\ S_2 = 1 & if & K_2\ closed & Else & S_2 = -1 & if & K_2\ open \\ S_3 = 1 & if & K_3\ closed & Else & S_3 = -1 & if & K_3\ open \end{cases} \quad \text{II} - 30$$

Substituting Equation II-29 into II-28 gives us the following system:

$$\begin{bmatrix} V_a \\ V_b \\ V_c \end{bmatrix} = \frac{E}{6} \begin{bmatrix} 2 & -1 & -1 \\ -1 & 2 & -1 \\ -1 & -1 & 2 \end{bmatrix} \begin{bmatrix} S_1 \\ S_2 \\ S_3 \end{bmatrix} \quad \text{II} - 31$$

The system Equations II-31 represents the mathematical model of the two-level three-phase PWM inverter.

II.3.2 PWM Control

PWM controls the inverter's switching states by comparing three sinusoidal reference voltages with a high-frequency triangular carrier signal. The inverter's control signals (*S1, S2, S3*) are generated at the points where the reference signals meet the carrier wave, setting the switching states of the power devices. This process is defined by two main parameters [63]:

- The modulation index m is the ratio of the carrier frequency f_p to the frequency of the reference voltage.:

$$m = \frac{f_p}{f} \quad \text{II} - 32$$

- The modulation rate r is the ratio between the amplitude of the reference voltage V_{ref} and the amplitude of the carrier U_p.:

$$r = \frac{V_{ref}}{U_p} \quad \text{II} - 33$$

II.4 Grid-Side Converter Modeling and Control

The benefits of the GSC include facilitating bi-directional power flow, enabling active power regulation by maintaining a stable DC bus voltage, and establishing a zero reference for reactive power. This helps achieve grid stability and maintain grid quality, especially by ensuring a unity power factor.

This converter is not designed to provide a regulated and adjustable DC output under varying AC load conditions, nor to support bidirectional power flow. Its primary function is to minimize harmonic distortion and to ensure that the input current remains nearly sinusoidal, thereby maintaining a power factor close to unity.

II.4.1 Grid-Side Converter Modeling

The GSC shares the same design as the previously mentioned MSC. It has three primary components: the load, the converter, and the source, as illustrated in II-5 [22, 64, 65, 62].

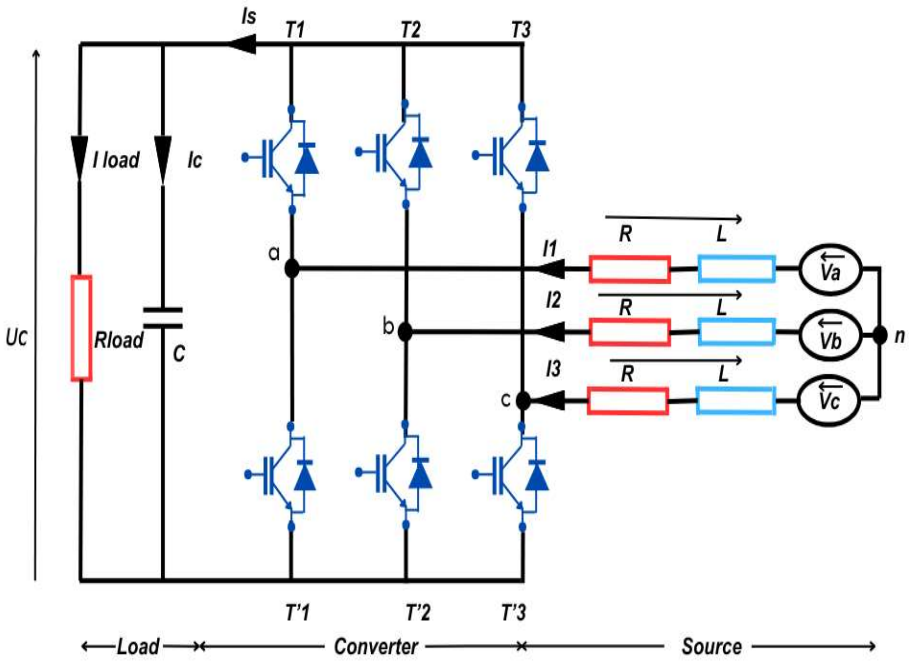

Figure II-5 : GSC Structure

The subsequent equations delineate the model for each component.

The phase voltage equations are given as follows:

$$\begin{cases} V_1 = R.I_1 + L\dfrac{dI_1}{dt} + V_{an} \\ V_2 = R.I_2 + L\dfrac{dI_2}{dt} + V_{bn} \\ V_3 = R.I_3 + L\dfrac{dI_3}{dt} + V_{cn} \end{cases} \qquad \text{II} - 34$$

The line currents can be expressed as:

$$\frac{d}{dt}\begin{bmatrix} I_1 \\ I_2 \\ I_3 \end{bmatrix} = \begin{bmatrix} -\dfrac{R}{L} & 0 & 0 \\ 0 & -\dfrac{R}{L} & 0 \\ 0 & 0 & -\dfrac{R}{L} \end{bmatrix}\begin{bmatrix} I_1 \\ I_2 \\ I_3 \end{bmatrix} + \frac{1}{L}.\begin{bmatrix} V_1 - V_{an} \\ V_2 - V_{bn} \\ V_3 - V_{cn} \end{bmatrix} \qquad \text{II} - 35$$

The converter on the grid side has the same structure as the one on the machine side:

$$\begin{bmatrix} V_a \\ V_b \\ V_c \end{bmatrix} = \frac{U_c}{3}.\begin{bmatrix} 2 & -1 & -1 \\ -1 & 2 & -1 \\ -1 & -1 & 2 \end{bmatrix}\begin{bmatrix} S_1 \\ S_2 \\ S_3 \end{bmatrix} \qquad \text{II} - 36$$

$$I_s = [S_1 \quad S_2 \quad S_3]\begin{bmatrix} I_1 \\ I_2 \\ I_3 \end{bmatrix} \qquad \text{II} - 37$$

$$\frac{dU_C}{dt} = \frac{1}{C}.(I_s - I_L) \qquad \text{II} - 38$$

$$U_C = R_l.I_L \qquad \text{II} - 39$$

$$\frac{U_C}{I_s} = \frac{R_l}{1 + R_l.C.p} \qquad \text{II} - 40$$

The block diagram of the GSC is illustrated from Equations II-34, II-35, II-36, II-37, II-38, II-39 and II-40.

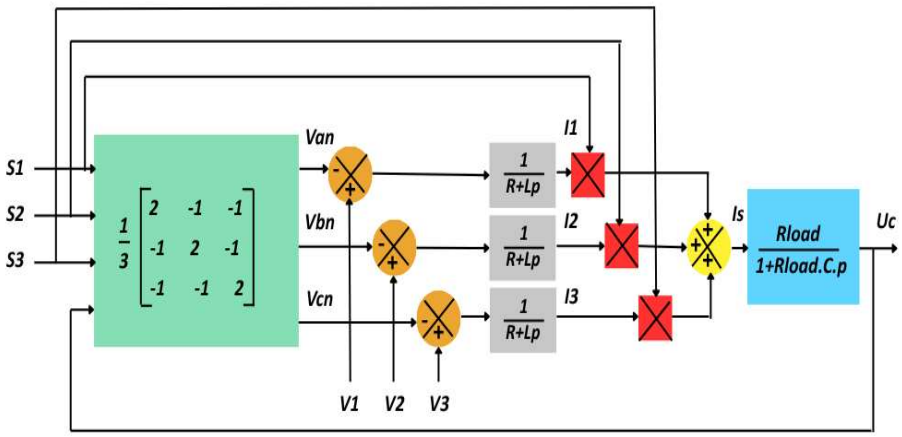

Figure II-6 : GSC Block diagram

II.4.2 Grid-Side Converter Control

The GSC can be controlled using a cascaded control structure, in which two inner control loops regulate the grid currents—typically aligned with the d- and q-axes—to achieve reactive and active power control. An outer control loop is employed to maintain the DC-link voltage at its reference value. In the synchronous d–q (Park) reference frame, the voltages and power expressions of the GSC can be formulated based on the transformed grid variables:

$$\begin{cases} V_{dp} = V_d - R.i_d - L\dfrac{di_d}{dt} + L\omega i_q \\ V_{qp} = V_q - R.i_q - L\dfrac{di_q}{dt} - L\omega i_d \end{cases} \qquad \text{II} - 41$$

$$\begin{cases} P = \dfrac{3}{2}.[V_d i_d + V_q i_q] \\ Q = \dfrac{3}{2}.[V_q i_d - V_d i_q] \end{cases} \qquad \text{II} - 42$$

The system can be presented in the form described above:

$$\begin{bmatrix} P \\ Q \end{bmatrix} = \frac{3}{2} \cdot \begin{bmatrix} V_d & V_q \\ V_q & -V_d \end{bmatrix} \begin{bmatrix} i_d \\ i_q \end{bmatrix} \qquad \text{II} - 43$$

By definition:

$$P_{ref} = U_{cmes} \cdot I_{red_ref}, \qquad Q_{ref} = 0 \qquad \text{II} - 44$$

- The reference voltage U_{cref} is compared with the measured capacitor voltage U_{cmes}.
- The error is processed by a PI controller, allowing regulation of the output voltage and generation of the reference current I_{cref}.
- The required active power is supplied to the capacitor, while the reactive power is maintained at zero to ensure unity power factor.
- Reference currents are determined from the reference powers and measured voltages.
- These currents are compared with the measured currents.
- The resulting current errors are regulated by PI controllers to produce reference voltages.
- These voltages are then compared with the measured voltages.
- Finally, the resulting errors generate control signals used to drive the six switches of the rectifier.

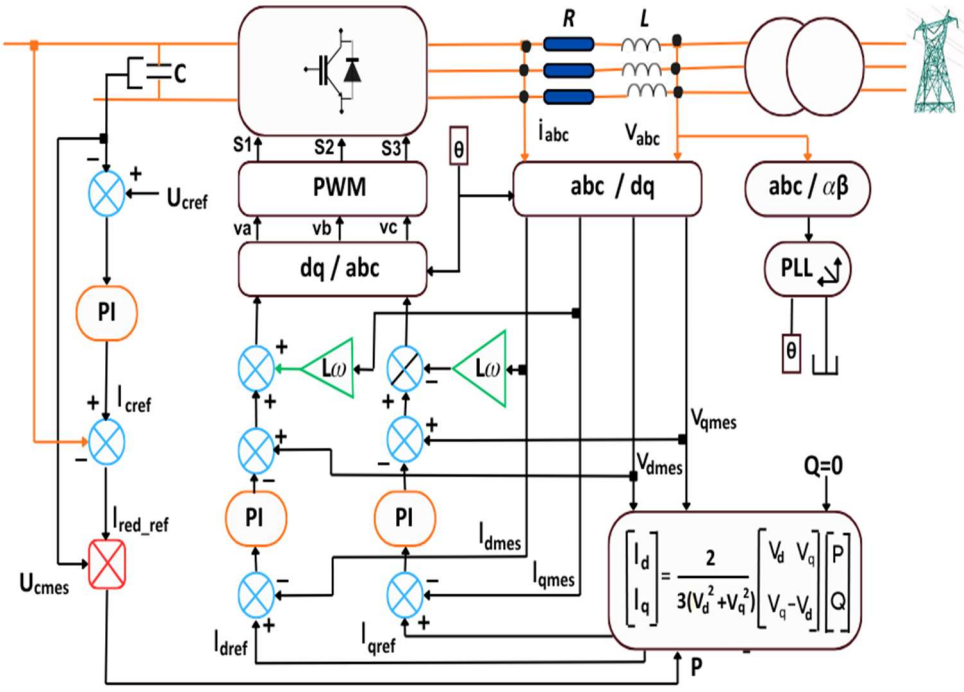

Figure II-7 : GSC Control Block Diagram

II.4.3 Simulation Results

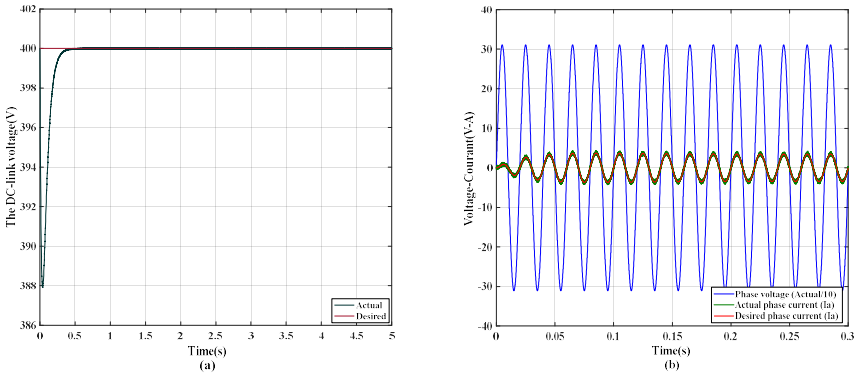

Figure II-8 : (a) DC Bus Voltage, (b) Line Voltage and Line Current

II.4.4 Results Interpretation

Figure II-8 presents: (a) the DC-bus voltage and (b) the line voltage and line current waveforms. The DC-bus voltage accurately follows its reference value, demonstrating effective voltage regulation. Furthermore, the line currents closely track their corresponding reference signals and exhibit smooth sinusoidal waveforms synchronized with the grid voltage, thereby ensuring operation at a unity power factor. These results confirm the effectiveness, stability, and reliability of the voltage-oriented control strategy in achieving accurate power regulation and high-quality grid current injection.

II.5 Wind Turbine Modeling and Control

For smooth operation, it is important to model the turbine accurately and keep its control reliable across varying wind speeds. In variable-speed wind energy systems, Maximum Power Point Tracking (MPPT) and pitch controls are essential for harnessing and managing wind's kinetic energy at both low and high speeds.

II.5.1 Wind Turbine Aerodynamic Modeling

Turbine modeling involves describing the extractable power as a function of wind speed and operating conditions. In WECS, a portion of the kinetic energy of the wind is captured and converted into mechanical energy through the rotation of the turbine rotor. This mechanical energy is transmitted via a gearbox (speed multiplier) and subsequently converted into electrical energy by the generator. Such modeling enables the determination of the aerodynamic torque applied to the turbine's low-speed shaft.

This approach is generally based on established theoretical formulations, supported by data available in the literature as well as technical specifications provided by turbine manufacturers.

The aerodynamic conversion process generates a torque that drives the rotor blades. The mechanical power captured by the turbine primarily depends on three key parameters: the air density ρ, the rotor swept area S, and the wind speed V_w. Among these, air density and wind speed are climate-dependent parameters that vary with location [66, 54, 52].

The incident power, also referred to as the theoretical wind power available at the turbine blades, can be expressed as follows:

$$P_w = \frac{1}{2}\rho S V_w^3 \qquad \text{II} - 45$$

With

$$S = \pi R^2 \qquad \text{II} - 46$$

The aerodynamic power generated by the turbine is given by Equation II−47:

$$P_{aer} = C_p(\lambda, \beta)P_w = \frac{1}{2}C_p(\lambda, \beta)\rho S V_w^3 \qquad \text{II} - 47$$

The nonlinear function known as the power coefficient C_p describes the turbine's aerodynamic efficiency and is specific to each turbine:

$$C_P(\lambda, \beta) = \big(0.5 - 0.0167(\beta - 2)\big)\sin\left[\frac{\pi(\lambda + 0.1)}{18.5 - 0.3(\beta - 2)}\right] - 0.00184(\lambda - 3)(\beta - 2) \qquad \text{II} - 48$$

λ is defined as the quotient of the incoming wind speed and the linear speed of the turbine blade as written in Equation $\text{II} - 49$:

$$\lambda = \frac{R.\Omega_t}{V_w} \qquad \text{II} - 49$$

In 1920, ***Albert Betz*** determined the maximum value of the power coefficient C_P [67]:

$$C_p = \frac{16}{27} = 0.593 \qquad \text{II} - 50$$

Figure II-9 depicts the variations in power coefficient relative to the tip speed ratio at various pitch angles.

To achieve maximum power, $C_{Pmax} = 0.5$ and the pitch angle $\beta = 2$, corresponding to an optimal tip speed ratio $\lambda_{opt} = 9.1$

MPPT is essential to ensure optimal power extraction under varying wind conditions, as the operating point is highly sensitive to wind speed fluctuations. This sensitivity arises from the strong dependence of the aerodynamic performance on the tip speed ratio λ and the pitch angle β [68, 69, 70].

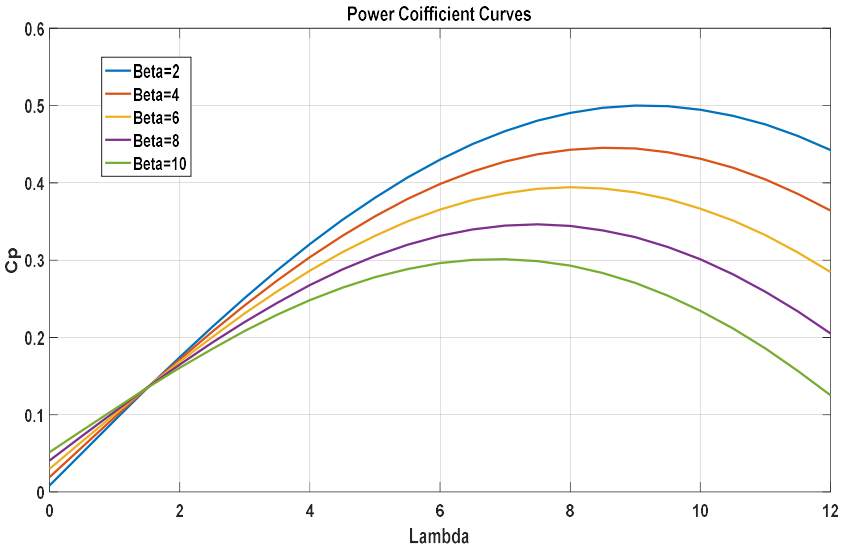

Figure II-9 : Power Coefficient Curves versus Lambda and Beta

II.5.1.1 Wind Turbine Speed Multiplier Modeling

The speed multiplier, or gearbox, connects the WT to the generator. Its main function is to convert the low rotational speed of the turbine into the higher rotational speed required by the generator for efficient process, whereas simultaneously decreasing the high torque produced by the turbine to a level compatible with the generator. Although the gearbox is, in reality, a complex mechanical system, it is here assumed to be perfectly rigid and is modeled as a simple gain, with energy losses considered negligible [71].

Under these assumptions, its behavior can be explained by the following two equations:

$$\Omega_{mec} = G.\Omega_t \qquad \text{II} - 51$$

$$T_g = \frac{T_t}{G} \qquad \text{II} - 52$$

II.5.1.2 Wind Turbine Mechanical Modeling

The mass of the WT is represented on the turbine shaft as an equivalent inertia J_T, which accounts for both the rotor blades and the turbine hub. In the proposed mechanical model, the total inertia J includes the turbine inertia reflected to the generator side, together with the generator's own inertia [72].

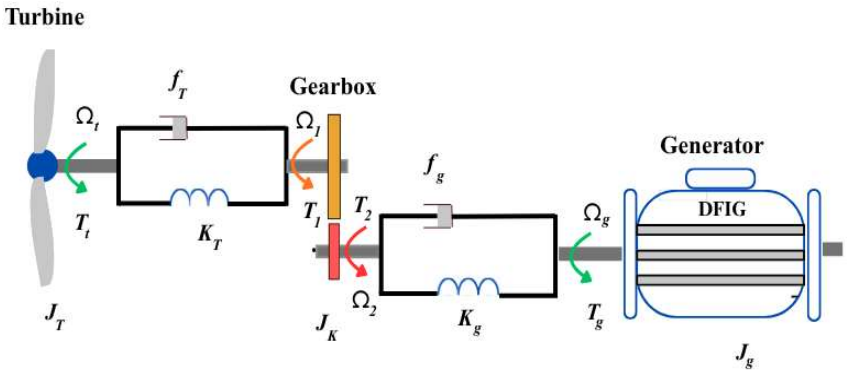

Figure II-10 : Mechanical Model of the Turbine

The equivalent three-mass model of the wind energy conversion chain is illustrated in Figure II-10. These masses correspond respectively to the WT rotor (approximately 90% of the total moment of inertia), the gearbox (about 2–4%), and the generator (approximately 6–8%). Considering the elasticity and friction effects of the two shafts, the following simplifying assumptions can be made:

- The turbine rotor consists of three identical blades of length *R*, rigidly fixed to the hub. The entire assembly is considered as a single equivalent inertia J_T.
- The inertia of the gearbox is negligible compared to that of the turbine and the generator; therefore, it is modeled as a constant speed gain *G*, or equivalently as a torque gain *1/G*.
- The transmission shafts are assumed to be perfectly rigid.

These assumptions lead to a simplified two-mass mechanical model of the WECS.

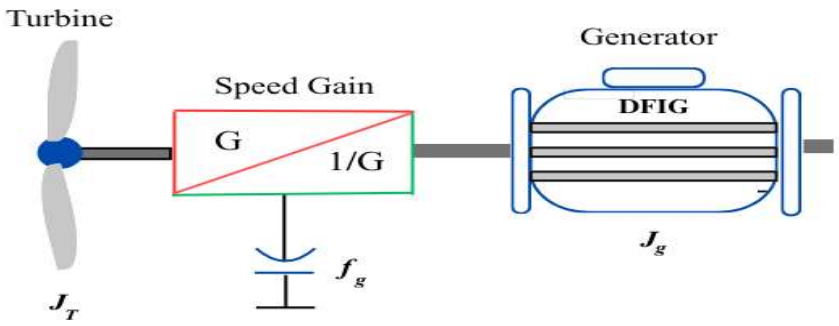

Figure II-11 : Simplified Model of the Turbine

$$J = \frac{J_T}{G^2} + J_g \qquad \text{II} - 53$$

Using the fundamental equation of dynamics, the rotor mechanical speed can be computed from the applied mechanical torque T_{mec}.

$$\sum \mathrm{T} = \mathrm{T_{mec}} = \mathrm{J}.\frac{\mathrm{d}\Omega_{\mathrm{mec}}}{\mathrm{dt}} \qquad \text{II} - 54$$

The mechanical torque is determined by the electromagnetic torque generated by the machine, the viscous friction torque, and the torque transmitted through the gearbox.

$$\mathrm{T_{mec}} = \mathrm{T_g} - \mathrm{T_{em}} - \mathrm{T}_f \qquad \mathrm{II}-55$$

The friction effects of the blades, hub, and shaft are aggregated into a single friction coefficient, normalized to the generator shaft and denoted by *f*.

$$f = \frac{f_T}{G^2} + f_g \qquad \mathrm{II}-56$$

Then:

$$\mathrm{T}_f = f.\Omega_{\mathrm{mec}} \qquad \mathrm{II}-57$$

By combining Equations II-54, II-55, and II-56, the fundamental equation governing the mechanical dynamics of the DFIM shaft is obtained as:

$$\mathrm{T_g} - \mathrm{T_{em}} = \mathrm{J}.\frac{\mathrm{d}\Omega_{\mathrm{mec}}}{\mathrm{dt}} + f.\Omega_{\mathrm{mec}} \qquad \mathrm{II}-58$$

The block diagram for modeling the WT can be easily obtained from the above equations and is shown in Figure II-12.

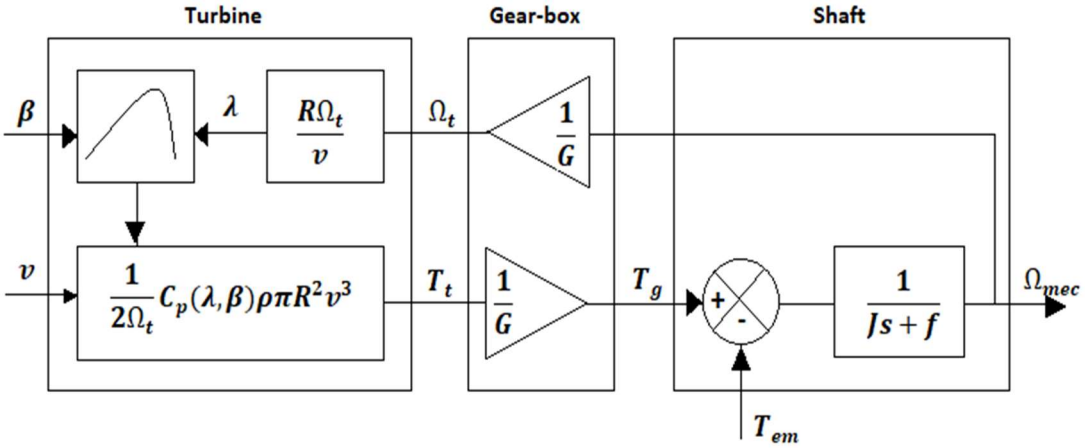

Figure II-12 : WT Model

Figure II-12 illustrates the conversion of wind kinetic energy P_w into aerodynamic torque T_t on the low-speed shaft of the WT. This torque is transmitted through the gearbox, which adapts the rotational speed and drives the high-speed shaft connected to the generator. The generator mechanical speed Ω_{mec} is determined by the balance between the driving torque T_g provided by the gearbox output and the opposing electromagnetic torque T_{em}.

Therefore, the regulation of the electromagnetic torque allows effective control of the generator rotational speed. To improve the energy conversion efficiency, two control techniques are implemented:

- MPPT control technique, which optimizes power extraction under low and medium wind speeds, and
- Pitch angle control technique, which limits aerodynamic power and maintains rated output under high wind speed conditions.

II.5.2 Wind Turbine Control

The behavior of a WT is highly sensitive to wind speed and exhibits strong nonlinearity, as described by aerodynamic models. The power–wind speed characteristic and the corresponding operating regions of a variable-speed WT are typically divided into four distinct zones, as illustrated in Figure II-13.

Zone 1: At very low wind speeds, below the cut-in threshold, the turbine remains idle and does not generate electrical power. In this region, both rotor speed and mechanical power are zero.

Zone 2: In the variable-speed operating region, once the wind speed exceeds the cut-in value, the control system aims to maximize energy capture. This is achieved by maintaining the blade pitch angle at its minimum while adjusting rotor speed to track the optimal tip-speed ratio for maximum power extraction.

Zone 3: At wind speeds above the rated value, the turbine reaches its nominal rotational speed and operates under constant power output. Pitch control is typically activated in this region, increasing the blade angle to intentionally reduce aerodynamic efficiency and limit the captured power to the rated level.

Zone 4: When wind speed exceeds the cut-out threshold, the turbine is shut down by protective control systems to prevent mechanical overload and ensure safe operation [73, 74].

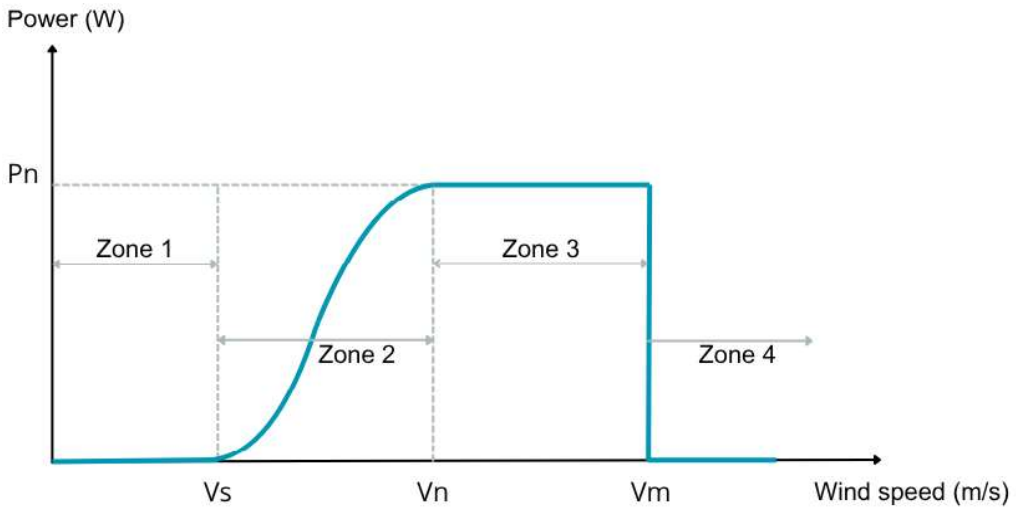

Figure II-13 : Power-speed curve of WT

II.5.2.1 Turbine Control at Low Wind Speeds

At low wind speeds, the available aerodynamic power is below the turbine's rated capacity; therefore, a MPPT technique is employed to extract the maximum possible energy from the wind. In indirect MPPT control, the blade pitch angle and the tip-speed ratio are maintained at their optimal values, βopt and λopt, in order to achieve the maximum power coefficient C_{pmax}.

Since wind speed is inherently variable, the MPPT controller continuously adjusts the operating point to ensure optimal energy capture. In Zone 2 (Figure II-13), the control system regulates the electromagnetic torque to track the maximum power point as wind conditions change, while keeping the blade pitch angle fixed at its optimal minimum value. The main objective is to adapt the generator rotational speed to follow the variations in wind velocity and maintain operation at the optimal tip-speed ratio.

Real-time wind speed estimation plays a crucial role in this strategy, enabling the DFIM to operate at its optimal operating point and maximize energy conversion efficiency.

The estimated wind speed is given by:

$$V_{est} = \frac{R.\Omega_t}{\lambda_{opt}} \qquad \text{II} - 59$$

Substituting Equation $\text{II} - 59$ into $\text{II} - 44$ yields the expression of the reference electromagnetic torque given in Equation $\text{II} - 60$:

$$T_{em}{}^{*} = \frac{1}{2\lambda_{opt}{}^{3}} C_p(\lambda_{opt}) \rho \pi R^{5} \Omega_t^2 \qquad \text{II} - 60$$

The WT model incorporating the MPPT control technique is illustrated in Figure II-14.

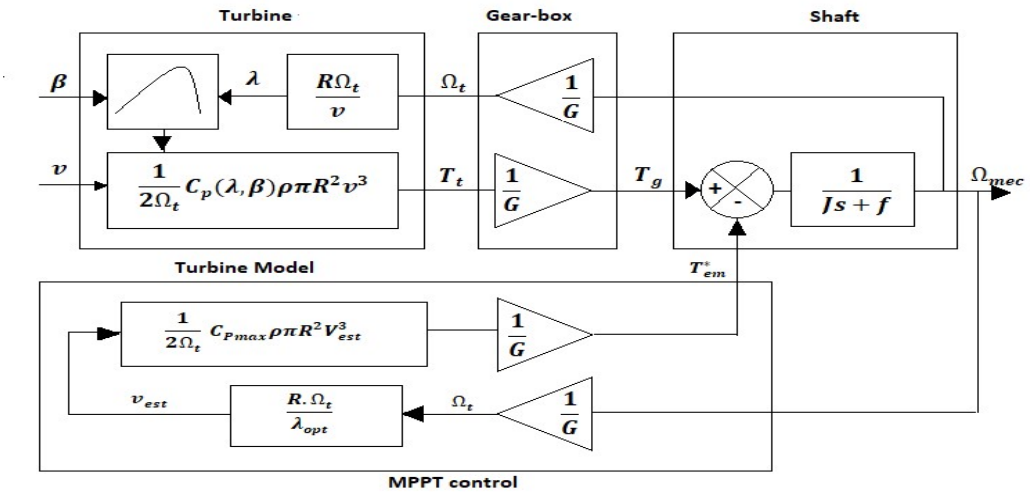

Figure II-14 : WT and MPPT Model

II.5.2.2 Turbine Control at High Wind Speeds

This control approach regulates the turbine's rotational speed during high wind gusts, ensuring that power output remains at its rated value and preventing overload circumstances. This is achieved by regulating the blade pitch angle, either collectively or individually. Adjusting the blade pitch angles allows the system to stabilize power production while protecting both mechanical and electrical components from excessive stress under high wind conditions. Zone 3 in Figure II-13 illustrates this operating mode, where pitch control plays a crucial role in regulating power and enhancing system flexibility.

- **Blade Orientation System**

This system regulates the blade pitch angle β to track its reference value βref, thereby controlling both turbine speed and mechanical power output. Several technologies are used for pitch angle regulation, including hydraulic actuators, which are commonly employed in medium-power turbines, and electric motor-driven systems, which require an external power supply and are typically used in high-power turbines.

Variations in pitch angle directly influence turbine performance by modifying the power coefficient. At low wind speeds, the blades are oriented to maximize aerodynamic capture, whereas at high wind speeds, the blades are pitched away from the wind to reduce the power coefficient and limit power production.

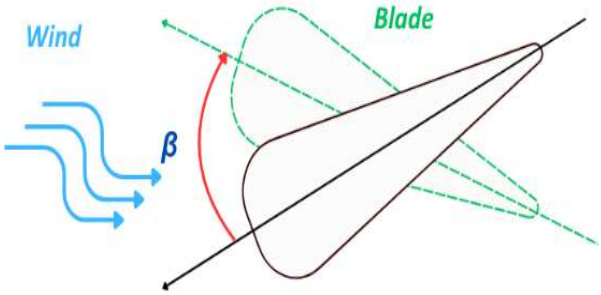

Figure II-15 : Blade Orientation

The blade pitch control system is commonly modeled as a first-order transfer function characterized by a time constant T_β. When simulating this system, it is important to consider the rate of change of the pitch angle β, which is typically limited to approximately 10°/s during normal operation and up to 20°/s under emergency conditions [75].

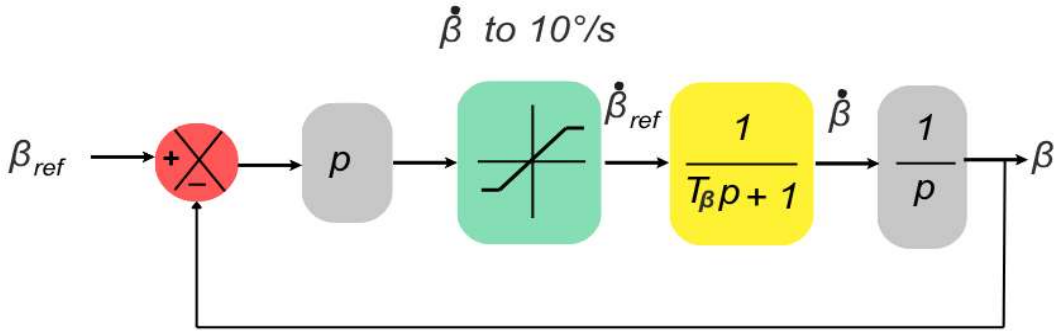

Figure II-16 : Blade Orientation Control System

Pitch control

High wind conditions can cause mechanical stress on WT components and may also disturb the electrical system. For this reason, pitch control plays a key role in optimizing energy capture and limiting excess power during gusts. The blades may be adjusted either collectively or individually to provide greater control flexibility. Zone 3 in Figure II-13 corresponds to this operating region.

The primary aim in this zone is to sustain the active power output at its nominal value P_n, in order to protect the turbine components. This is achieved by increasing the blade pitch angle, which reduces the power coefficient C_p and consequently limits the aerodynamic power conversion.

To generate the reference pitch angle βref, the measured active power P_{mes} is compared with the nominal power P_n, and the error is processed through a PI controller. The resulting control action defines the reference pitch rate βref, which is used to adjust the blade angle toward βref.

The pitch rate βref is subject to saturation limits to ensure safe actuator operation. A $1/p$ integrator is then used to compute the actual pitch angle β, as illustrated in Figure II-17 [75, 76].

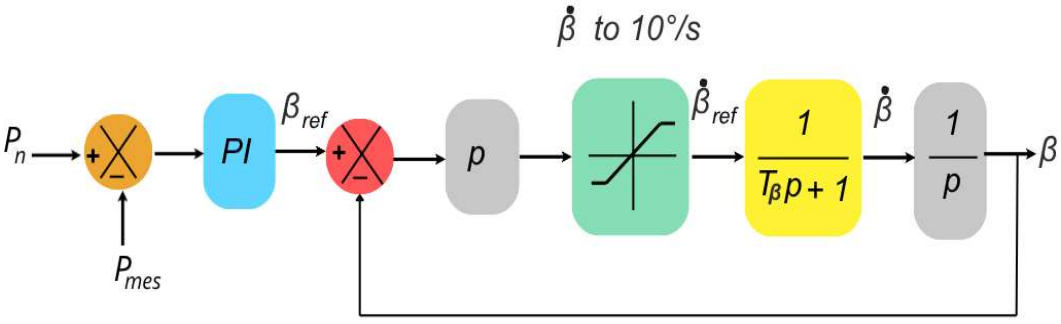

Figure II-17 : Pitch Control System

II.5.3 Simulation Results

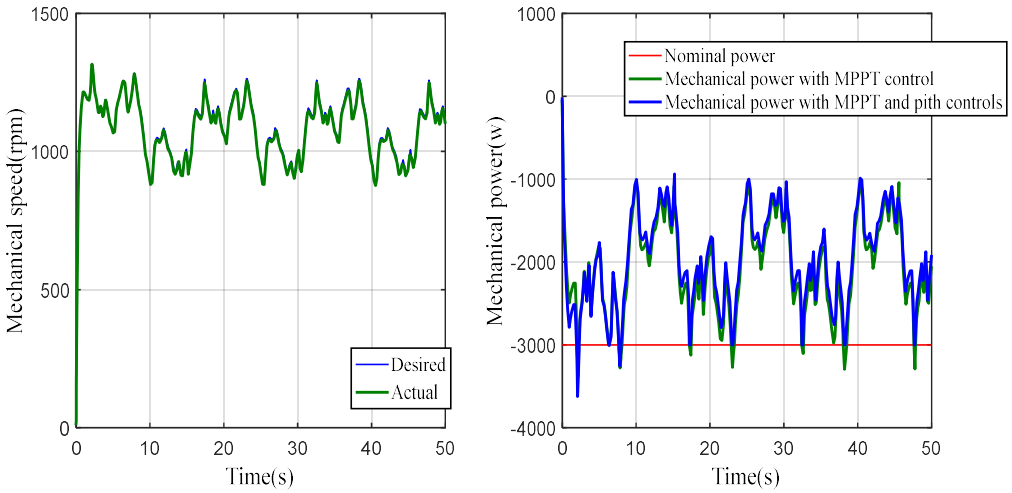

Figure II-18 : Mechanical Speed and Power Generated Signal

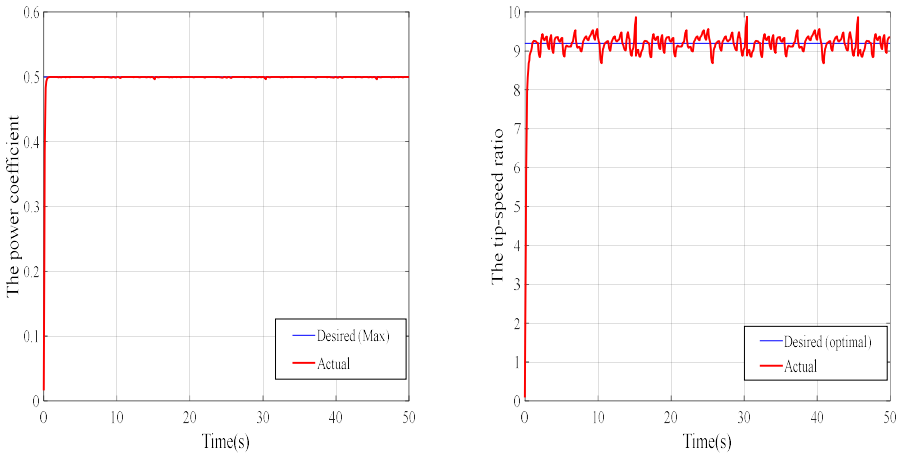

Figure II-19 : Power Coefficient and Specific Speed

II.5.4 Results Interpretation

A simulation study was performed to assess two control systems. The initial approach, known as indirect MPPT, is utilized in low wind speed scenarios. In this area, the tip-speed ratio is sustained at its ideal reference value, enabling the power coefficient to attain its maximum and assuring maximal energy extraction.

The secondary mechanism, referred to as pitch control, is engaged at elevated wind speed. In this operational domain, the mechanical speed is controlled to sustain the generated power at its rated level, therefore safeguarding the WT from overload and guaranteeing safe functionality.

II.6 Conclusion

This chapter presents the modelling of a variable-speed WECS based on a DFIM. The system operates with a variable-speed WT and is regulated by MSC consisting of two back-to-back bidirectional power converters linked by a DC-link.

The modelling technique starts with the depiction of the DFIM in the synchronous rotating reference frame (d–q), which considerably streamlines the mathematical formulation and enhances control design. The MSC regulates power exchange with the rotor, enabling separate regulation of stator active and reactive power. The GSC, together with its corresponding control system, regulates the DC-link voltage at a stable level and enhances the power factor at the grid connection point.

The mechanical aspects of WT dynamics have been modelled, incorporating essential control techniques such as indirect MPPT to optimize energy capture at low wind speeds, and pitch angle control to restrict output power at high wind speeds, so ensuring safe operation.

The entire system has been executed and modelled via MATLAB/Simulink. The results obtained demonstrate strong concordance with those documented in the literature, affirming the validity and efficacy of the suggested model.

The following chapter will present the theoretical foundations of the control technique adopted in this work, as well as the optimization methods used to enhance system performance.

Chapter III : Theoretical Aspects of the Control System and Optimization Method

III.1 Introduction

To ensure high-quality electrical power output from a DFIG-based WT system, an appropriate control technique must be implemented to regulate the stator-generated power. In particular, the active power must track the reference power extracted from the WT in order to maximize energy conversion efficiency, while the reactive power must be controlled according to grid requirements imposed by the operator.

To meet these objectives, a stator flux-oriented control (SFOC) technique based on PI, FPD, and FPD+I controllers is proposed. However, the performance of this control approach is highly dependent on the proper tuning of controller gains. To address this limitation and improve dynamic performance, an optimization technique is introduced to determine the optimal controller parameters.

In this chapter, the theoretical foundations of the proposed control strategy and the selected optimization method are presented. These approaches are then applied to a WECS to achieve optimal regulation of both active and reactive power.

III.2 Stator Flux-Oriented Control

III.2.1 Principle of SFOC

Vector control of AC machines enhances both steady-state and dynamic performance by adopting a control principle analogous to that of DC machines, where flux and torque are independently regulated. In this approach, machine variables are decomposed into two orthogonal components: the direct-axis (d-axis), aligned with the stator flux, and the quadrature-axis (q-axis), which is primarily associated with torque production through current components.

The SFOC technique employs a rotating reference frame defined by two perpendicular axes (d–q), with the d-axis aligned with the stator flux vector. This alignment enables decoupled control of electromagnetic quantities. By maintaining orthogonality between the flux and current components, efficient torque generation is ensured, while allowing independent control of the stator active and reactive power [19].

III.2.2 Different Types of SFOC

In a DFIM, the stator power is linked to the rotor voltage through a first-order transfer function that includes coupling terms of different importance. This relationship leads to two main ways of controlling the machine's power. The direct control approach ignores the coupling terms

and uses separate regulators on each axis to manage active and reactive power independently. On the other hand, the indirect control approach accounts for these coupling effects and adds compensation terms to decouple the system, boosting accuracy and dynamic performance [77].

III.2.2.1 Direct SFOC

The direct method, introduced by ***Felix Blaschke*** around 1970, relies on precise knowledge of the stator flux and its position. It requires several measurements at the drive terminals, with one option being to place sensors in the stator windings to directly measure flux components and determine their magnitude and phase. However, these sensors are delicate and can face significant stress from vibrations and temperature changes, and they also add considerable cost to the system. As a result, most practical setups use flux estimators or observers based on electrical measurements from the drive. The direct method's main advantage is that it's relatively unaffected by changes in machine parameters. In direct vector control, the idea is to independently and directly manage the drive's active and reactive power while ignoring coupling terms. Figure III-1 shows how this direct control method works [77, 78].

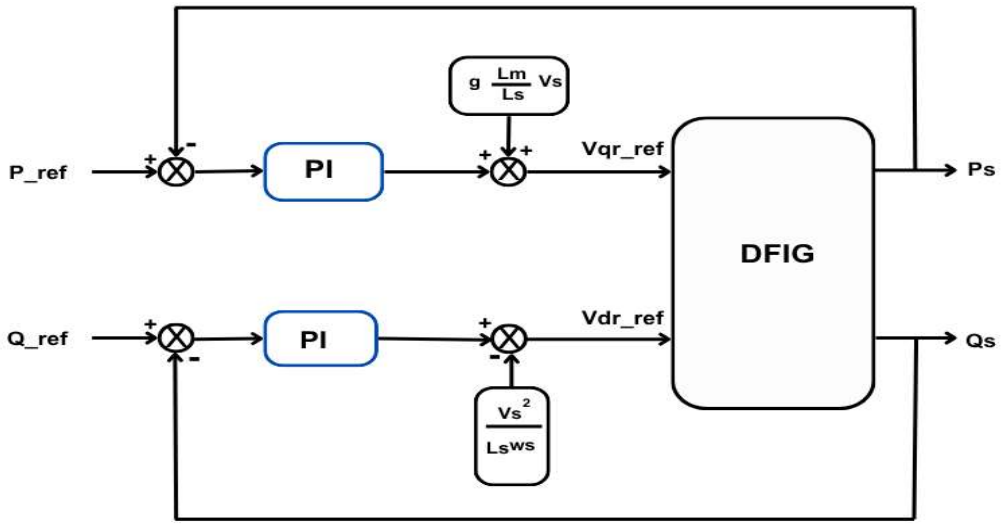

Figure III-1 : Direct Control

III.2.2.2 Indirect SFOC without Power Loop

Within this approach, decoupling is achieved at the outputs of the rotor current control loops without requiring feedback from the stator power, by applying appropriate reference voltages V_{dr} and V_{qr}. Furthermore, indirect control without power feedback (i.e., open-loop with respect to power) enables closed-loop regulation of the rotor currents I_{dr} and I_{qr}, while the stator

active and reactive powers P_s and Q_s are governed in open loop through their dependence on the rotor current components [77].

Figure III-2 illustrates the schematic representation of the machine decoupling control scheme.

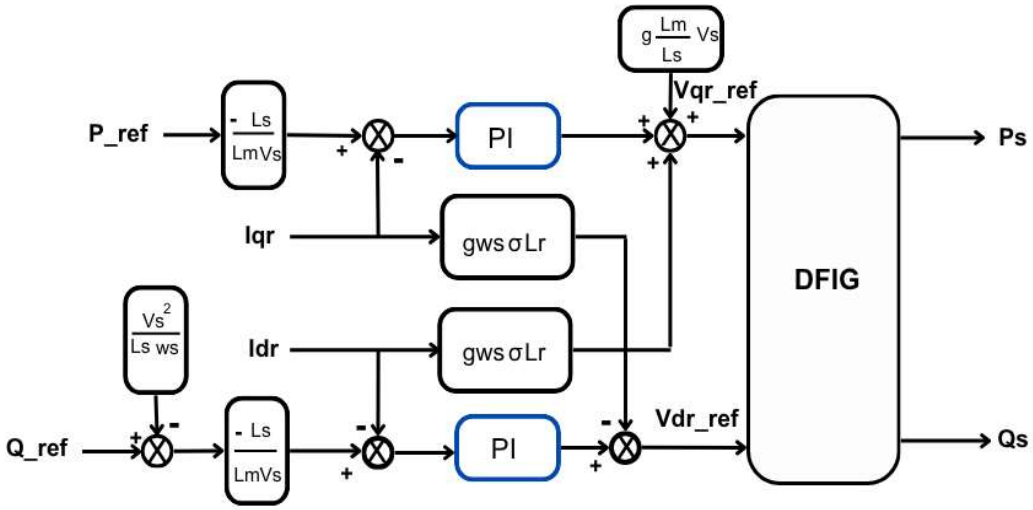

Figure III-2 : Indirect Open-Loop Power Control

III.2.2.3 Indirect SFOC with Power Loop

In this method, decoupling is applied at the rotor current regulator outputs, with system feedback ensuring precise power control. This creates a cascaded loop structure, enabling independent closed-loop regulation of the rotor currents (I_{dr} *and* I_{qr}) and the powers (P_s and Q_s). A simplified diagram of the control–decoupling block and machine assembly is shown in Figure III-3.

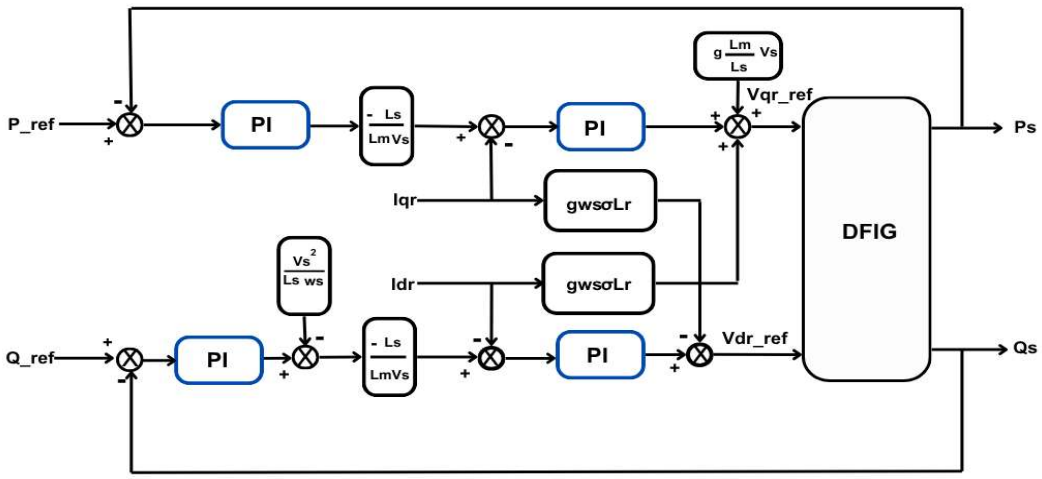

Figure III-3 : Indirect Closed-Loop Power Control

While this configuration complicates the control system, it offers greater robustness against electrical grid disturbances. The proportional–integral controllers used for current and power

regulation are simple to implement and provide satisfactory performance for generator operation [76, 77, 79].

III.2.3 Advantages and Disadvantages of SFOC

SFOC is widely employed in the control of AC machines due to its numerous advantages. One of its main strengths lies in the decoupled control of active and reactive power. Aligning the reference frame with the stator flux makes it possible to control these powers separately, in a manner analogous to DC machine control. Furthermore, this orientation simplifies the control structure, as it reduces the complexity of the mathematical equations compared to other vector control techniques.

Another significant advantage of SFOC is its fast-dynamic response, which allows rapid adjustment of electromagnetic torque and power. This feature makes it especially well-suited for variable-speed uses, like WECSs. In addition, the method ensures improved stability, providing satisfactory performance in both stable and changing operating conditions. From an implementation perspective, SFOC is relatively simple, as it does not require rotor flux estimation based on rotor parameters, unlike rotor flux-oriented control. Moreover, it demonstrates good performance in grid-connected systems, especially in applications such as DFIG-based WTs, where stator variables are directly linked to the grid.

Despite these advantages, SFOC presents several limitations that may affect its performance. One of the main drawbacks is its sensitivity to stator resistance variations. Since stator flux estimation depends on this parameter, any change due to temperature variations can degrade control accuracy. Additionally, flux estimation becomes more challenging at low speeds, where reduced stator voltage leads to decreased estimation precision.

Another limitation is the dependence on integrators for flux calculation. The use of pure integration of voltage signals can introduce drift and offset errors over time. Moreover, the method exhibits limited robustness to parameter uncertainties, which may compromise the effectiveness of decoupling and overall control accuracy. The performance of SFOC can also degrade under external disturbances, such as grid fluctuations or measurement noise, which negatively impact flux estimation.

To mitigate these issues, advanced techniques such as observers, filters, or adaptive compensators are often required. However, the integration of these additional elements increases the overall complexity of the control system.

III.2.4 Different Types of Controllers Used

A variety of controllers are employed in control systems to maintain stability, enhance accuracy, and achieve optimal performance across different operating conditions.

III.2.4.1 PI Controllers

Among the most commonly used controllers, the Proportional (P) controller provides a control action proportional to the error signal, offering a simple and fast response; however, it often leads to steady-state errors. To overcome this limitation, the Proportional–Integral (PI) controller is widely employed, as it combines proportional action with an integral term that eliminates steady-state error and improves accuracy [80].

Figure III-4 depicts a conventional PI controller, whose transfer function is:

$$u(t) = K_p e(t) + K_i \int_0^t e(\tau)\, d\tau \qquad \text{III} - 1$$

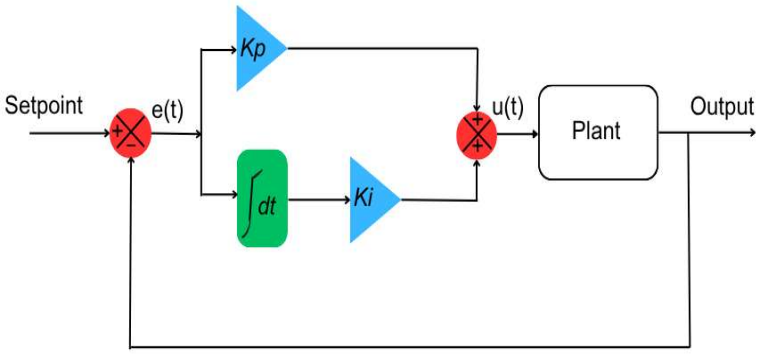

Figure III-4 : PI Controller Structure

where $u(t)$ denotes the control input, k_p and k_i are the proportional and integral gains, respectively, and $\mathrm{e}(\mathrm{t})$ represents the error signal defined as the difference between the reference (set point) and the plant output.

Due to their simple structure and reliable performance, PI controllers are extensively used in industrial process regulation, although their linear nature may limit effectiveness in strongly nonlinear systems.

III.2.4.2 Fuzzy Controllers

- **Fuzzy Logic Control Concept**

Fuzzy set theory, introduced six decades ago by the mathematician ***Lotfi Zadeh***, provides a mathematical framework for handling imprecise and uncertain information in complex systems. It is based on a set of rules designed to model ambiguity and approximate reasoning. Subsequently, ***Ebrahim Mamdani*** pioneered its application in control systems, which led to the widespread adoption of fuzzy logic controllers for nonlinear and uncertain processes [81, 82].

A rule-based framework that includes fuzzification, inference, and defuzzification is the foundation of FLC. Membership functions use expert knowledge of the dynamic behavior of the system, process interpretation, and system knowledge to map the input and output variables to language terms [82].

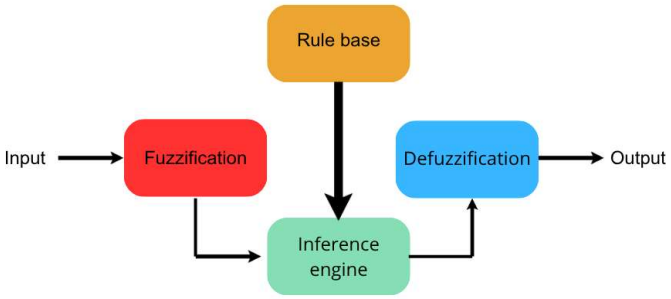

Figure III-5 : Fuzzy Logic System

FPD Controllers

Research on fuzzy controllers is often focused on two-input configurations [83], where ***Ying*** proposed the use of error and error-rate signals as input variables. Fuzzy control is widely regarded as an alternative to conventional PID control, with the most common two-input structures being the PD and PI forms [84].

The fuzzy PD controller provides a fast-dynamic response and strong tracking capability, making it suitable for systems requiring rapid adjustments; however, it may suffer from steady-state errors and sensitivity to noise. The fuzzy PI controller improves steady-state accuracy and ensures smoother control performance, particularly in noisy environments, although it generally exhibits slower response and may introduce overshoot [85, 86].

The fuzzy PID controller combines the advantages of both approaches, offering fast response, reduced steady-state error, and improved robustness. Nevertheless, this improved performance comes at the expense of increased rule-base complexity and a higher risk of oscillations if not properly tuned [87].

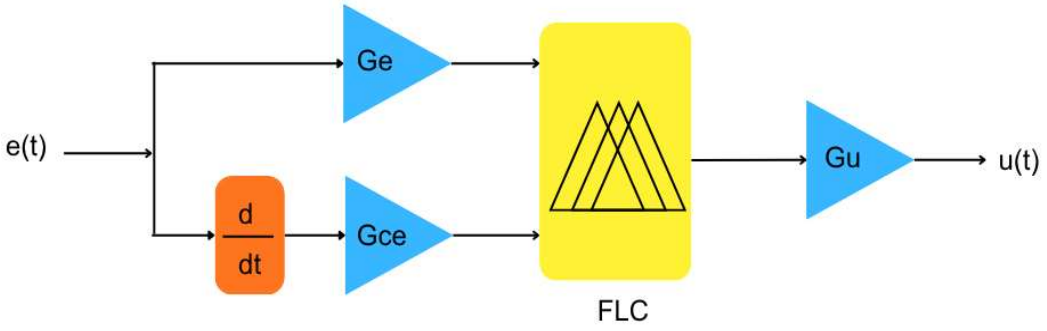

Figure III-6 : Fuzzy PD Controller Structure

FPD+I Controllers

The previously mentioned issues can be overcome by employing a fuzzy PD+I controller, which integrates a fuzzy PD structure with a linear integral (I) component, as shown in Figure III-7.

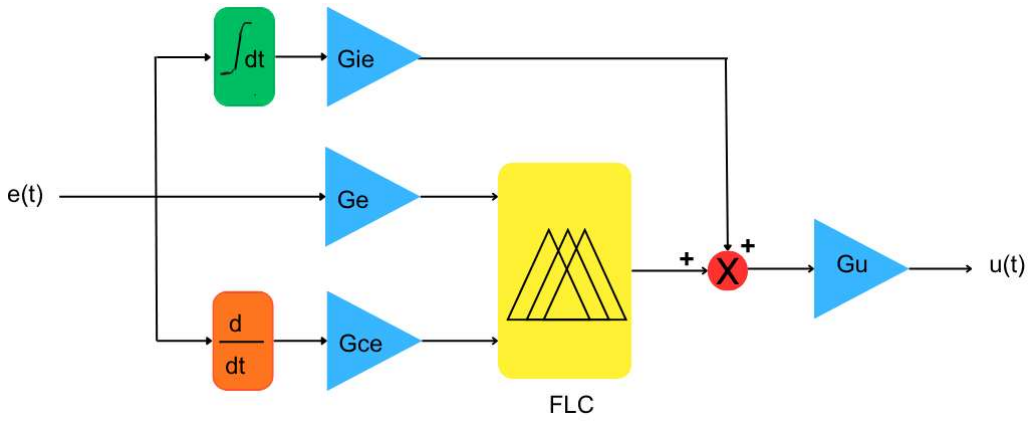

Figure III-7 : Fuzzy PD+I Controller Structure

In this approach, the fuzzy inference system is used together with integral action to form the control signal through the addition of the integral term to the fuzzy output [86, 88, 89, 87].

III.3 Optimization Using the GWO Algorithm

III.3.1 Definition

Grey Wolf Optimization (GWO) is a metaheuristic algorithm inspired by how grey wolves organize and hunt in nature. First introduced by ***Mirjalili*** and colleagues in **2014**, it imitates the pack's leadership hierarchy and hunting techniques to solve complex optimization problems. With its simple design, easy setup, and reliable convergence, GWO has become popular in engineering, especially for tasks like tuning controllers and optimizing energy systems [27, 90, 91].

III.3.2 Principle of the Technique

GWO technique takes inspiration from the hunting and social behavior of grey wolves. Solutions are ranked as alpha, beta, delta, and omega wolves, with the top three leading the search. The process explains in three stages: encircling the prey, hunting, and attacking. First, wolves estimate the prey's (optimal solution's) location and adjust their positions to surround it. During the hunt, each wolf follows the lead of the top three solutions, moving toward promising areas. In the attack stage, wolves close in as exploration slows. Gradually adjusted parameters shift the focus from wide searching to precise fine-tuning, helping GWO balance exploration and exploitation for effective convergence on the best or near-best solution [27, 90, 91].

III.3.3 Operators

The GWO algorithm relies on a set of mathematical operators that model the social behavior and hunting mechanisms of grey wolves. These operators include encircling, hunting, and attacking (exploitation) as well as exploration.

III.3.3.1 Social Hierarchy

The algorithm takes inspiration from a wolf pack's social hierarchy, made up of four types: alpha, beta, delta, and omega. The alpha represents the top candidate solution and leads the search, while the beta and delta—second- and third-best solutions—support the alpha in decision-making. The rest, known as omegas, follow the lead of the dominant wolves. This structure helps the search focus on promising areas while keeping the population diverse. The GWO works in three main stages: encircling, hunting, and attacking the prey [27, 90, 91].

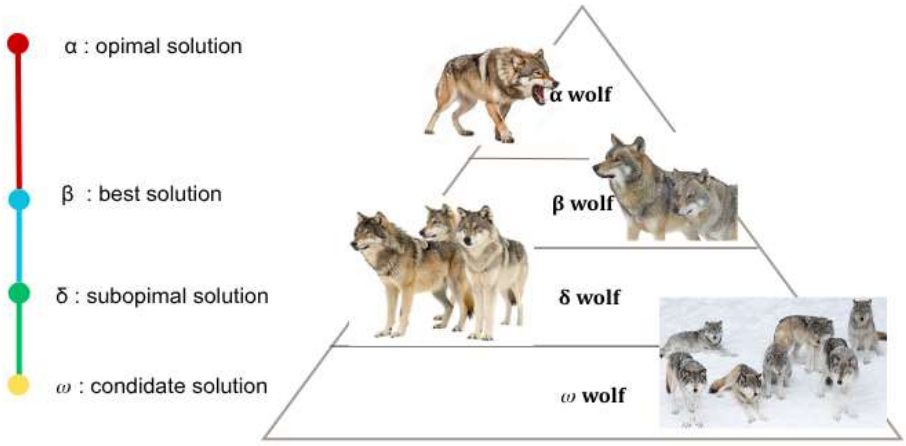

Figure III-8 : Hierarchy of a Grey Wolf Pack

III.3.3.2 Encircling Phase

Encircling models how wolves surround their prey. Since the exact location of the prey (or best solution) isn't known, wolves move based on estimates from the best solutions so far. Coefficient vectors control the distance and direction of movement, letting the wolves adjust their positions as they explore the search space [27, 90, 91].

III.3.3.3 Hunting Phase

Hunting uses the combined knowledge of the alpha, beta, and delta wolves. Instead of following just one leader, each wolf updates its position based on all three top solutions. This teamwork makes the algorithm more reliable, less likely to get stuck in local optima, and helps it find better solutions faster [27, 90, 91].

III.3.3.4 Attacking Phase

The attacking phase is the exploitation stage. As wolves get closer to the prey, their moves become more precise and focused. This behavior marks the final push toward the optimal solution.

In addition to these mechanisms, GWO relies on mathematical operators that control exploration and exploitation throughout the optimization process. Exploration is promoted when the search agents are encouraged to move away from current best solutions, allowing the algorithm to investigate new regions of the search space. Conversely, exploitation occurs when the agents converge toward the best solutions, refining them iteratively. The adaptive adjustment of control parameters ensures an effective balance between these two phases, contributing to the overall efficiency and robustness of the algorithm [27, 90, 91].

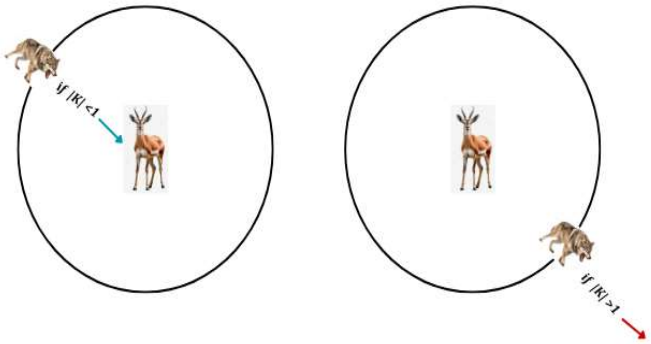

Figure III-9 : Attacking Prey versus Searching Prey

III.3.4 Mathematical Model of the GWO Technique

In the encircling phase, wolves close in on their prey using mathematical models to calculate the distance vector $\vec{l}$ and the prey position vector $\overrightarrow{y}$ defined in equations III-2 and III-3. These are determined by the coefficient vectors $\vec{b}$ and $\vec{k}$. The coefficients are derived from the random vectors $\overrightarrow{r_1}$ and $\overrightarrow{r_2}$, uniformly distributed in an interval [0,1], which stochastically guide the w*ol*ves' movements toward the prey [27, 90, 91].

$$\vec{l} = \left|\vec{b}.\overrightarrow{y_P}\,(i) - \vec{y}(i)\right| \qquad \text{III} - 2$$

$$\vec{y}(i+1) = \left|\overrightarrow{y_p}(i) - \vec{k}\,.\vec{l}\right| \qquad \text{III} - 3$$

Equations III-4 and III-5 describe the computation of the vectors $\vec{k}$ and $\vec{b}$, respectively:

$$\vec{k} = 2.\vec{a}.\overrightarrow{r_1} - \vec{a} \qquad \text{III} - 4$$

$$\vec{b} = 2.\overrightarrow{r_2} \qquad \text{III} - 5$$

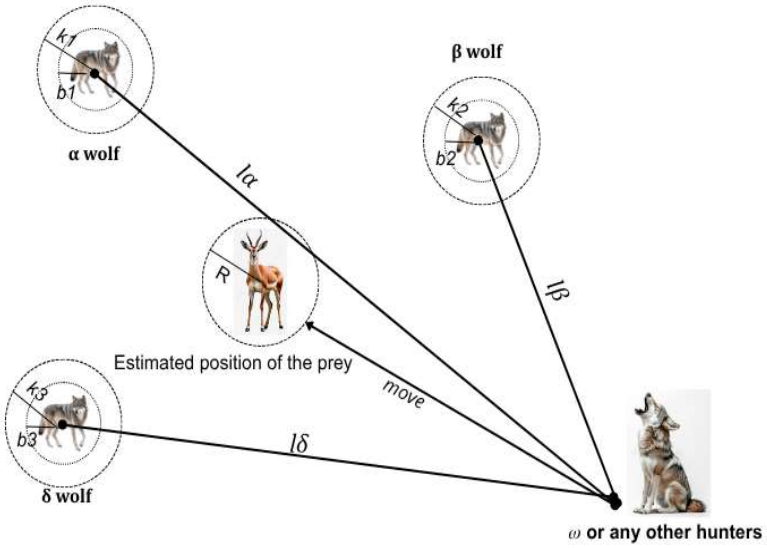

Figure III-10 : Position Updating in GWO

The positions of the α, β, and δ wolves are updated using Equations III-9, III-10, and III-11, respectively, based on the random coefficient vectors $\overrightarrow{k_1}$, $\overrightarrow{k_2}$, and $\overrightarrow{k_3}$, as well as the current iteration index.

$$\overrightarrow{l_\alpha} = \left|\overrightarrow{b_1} . \overrightarrow{y_{\alpha.}} - \vec{y}\right| \qquad \text{III} - 6$$

$$\overrightarrow{l_\beta} = \left|\overrightarrow{b_2} . \overrightarrow{y_{\beta.}} - \vec{y}\right| \qquad \text{III} - 7$$

$$\overrightarrow{l_\delta} = \left|\overrightarrow{b_3} . \overrightarrow{y_{\delta.}} - \vec{y}\right| \qquad \text{III} - 8$$

$$\overrightarrow{y_1} = \overrightarrow{y_\alpha} - \overrightarrow{k_1} . \overrightarrow{l_\alpha} \qquad \text{III} - 9$$

$$\overrightarrow{y_2} = \overrightarrow{y_\beta} - \overrightarrow{k_2} . \overrightarrow{l_\beta} \qquad \text{III} - 10$$

$$\overrightarrow{y_3} = \overrightarrow{y_\delta} - \overrightarrow{k_3} . \overrightarrow{l_\delta} \qquad \text{III} - 11$$

$$\vec{y}(i+1) = \frac{\overrightarrow{y_1} + \overrightarrow{y_2} + \overrightarrow{y_3}}{3} \qquad \text{III} - 12$$

In the exploration (divergence) phase, the coefficient vector k takes values outside the interval [−1,1], boosting global search capability to cover a broader area of the search space and lowering the chance of getting stuck in local optima.

During the exploitation phase, the wolves gradually close in on the prey by reducing the control parameter $\vec{a}$, which narrows the range of $\vec{k}$ to [−2a⃗, 2a⃗]. When $\vec{k}$ falls within interval [−1,1], the agents switch to a localized search (pursuit) mode around the top solutions. The overall optimization process is illustrated in the flowchart in Figure III-11.

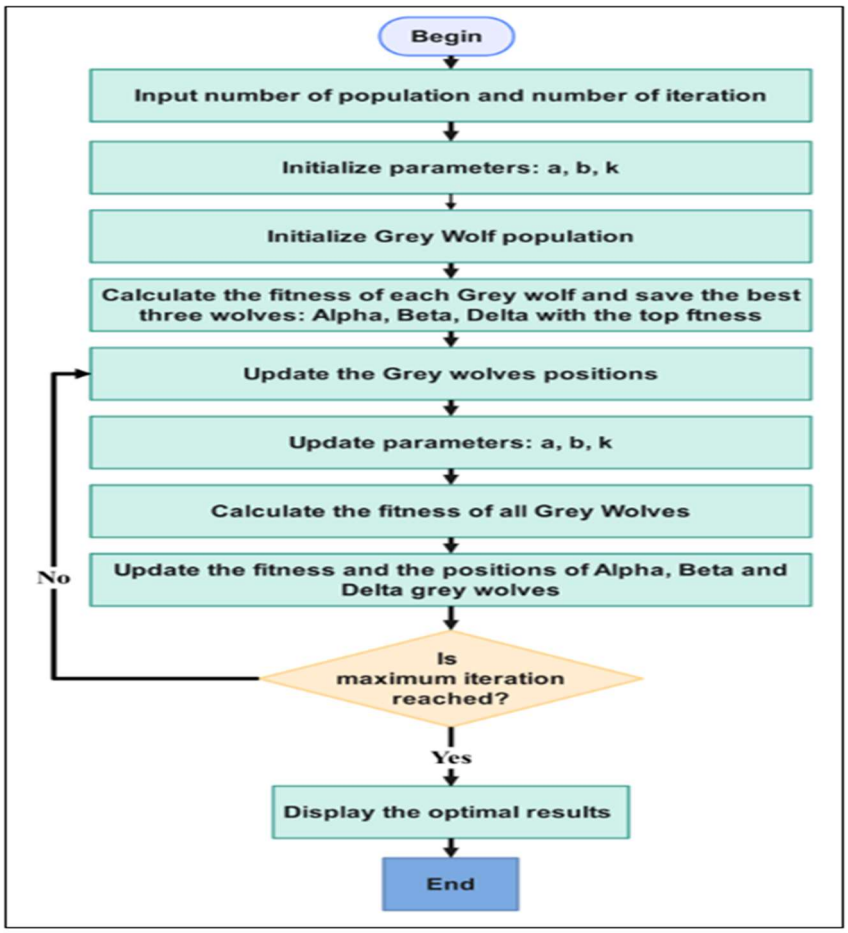

Figure III-11 : GWO Algorithm Flowchart

III.3.5 Objective Function for the Grey Wolf Optimizer

The performance of the GWO depends on the definition of an appropriate objective (fitness) function that quantitatively evaluates the quality of each candidate solution. In this work, the optimization objective is to determine the controller parameters that provide the best dynamic performance of the DFIM-based WECS while ensuring accurate active and reactive power tracking.

To achieve this objective, the Integral of Time-weighted Absolute Error (ITAE) is selected as the fitness function due to its ability to assign greater penalties to errors that persist over time. Accordingly, the optimization problem is formulated as follows:

$$J = \int_0^T t.|e(t)|dt \qquad III-13$$

where

J is the objective (fitness) function;

T is the simulation duration;

$e(t)$ is the power tracking error:

For each search agent (grey wolf), the candidate controller parameters are applied to the DFIM control system in MATLAB/Simulink, and the complete simulation is executed over the specified operating conditions. The resulting ITAE value is computed and assigned as the fitness of that candidate solution. The optimization process seeks the parameter set that minimizes the objective function while satisfying the prescribed bounds of the controller parameters.

Accordingly, the optimization problem for PI controller can be expressed as

$$\min_{x} \; J(x) = \int_0^T t.|e(t)|dt \qquad III-14$$

$$\text{s.t.} \quad x = \begin{bmatrix} k_p \\ k_i \end{bmatrix}$$

$$k_{p,min} < k_p < k_{p,max}$$

$$k_{i,min} < k_i < k_{i,max}$$

whereas for the FPD and FPD+I controllers, the decision vector additionally includes the input and output scaling factors and the integral gain. During the optimization process, the GWO algorithm iteratively updates these parameters until the minimum objective function is obtained. The optimal parameter set corresponding to the alpha wolf is then retained and used in the subsequent simulations of the WECS.

The use of the ITAE criterion enables the optimized controllers to achieve faster transient response, reduced oscillations, lower overshoot, and improved steady-state accuracy compared with conventionally tuned controllers.

III.4 Conclusion

In this chapter, we have outlined the theoretical principles of stator flux-oriented control, which allows the regulation of generated power to be decoupled, and defined the various types of this control system, the most commonly used for controlling active and reactive power. We have chosen Indirect SFOC without Power Loop for its simplicity of implementation and for the ability to control and limit currents in order to protect the machine's rotor winding. We then defined the different types of controllers used in this control system PI, FPD and FPD+I. Finally, we presented the theory behind the optimization techniques used to improve the performance of these controllers.

Chapter IV : Control System Implementation and Optimization Technique

IV.1 Introduction

The SFOC approach is an effective and relatively straightforward method of controlling AC machines, particularly in wind energy applications. However, accurate flux estimation and an understanding of the parameters are essential for achieving optimal performance, which requires the application of advanced optimization techniques. GWO provides a powerful and flexible framework for solving nonlinear and complex optimization problems. Its ability to balance exploration and exploitation, combined with its simple structure, makes it particularly well-suited to such problems.

This chapter will demonstrate the application of the proposed control method to various regulators PI, FPD, and FPD+I, as well as the optimization technique employed to enhance their performance, specifically in a wind power system for the optimal control of active and reactive energy.

IV.2 SFOC Algorithm

The control approach enhances the quality of energy supplied to the grid by employing a SFOC algorithm that correlates stator power with rotor voltages from the inverter. These connections provide the independent adjustment of active and reactive power via the rotor current components. The DFIG operates analogously to a separately stimulated DC machine: active power is associated with the quadrature rotor current I_{qr}, whilst reactive power is linked to the direct rotor current I_{dr}.

Keep in mind the system of differential equations:

$$\begin{cases} V_{ds} = R_s I_{ds} + \dfrac{d}{dt}\phi_{ds} - \omega_s \phi_{qs} \\ V_{qs} = R_s I_{qs} + \dfrac{d}{dt}\phi_{qs} + \omega_s \phi_{ds} \\ V_{dr} = R_r I_{dr} + \dfrac{d}{dt}\phi_{dr} - \omega_r \phi_{qr} \\ V_{qr} = R_r I_{qr} + \dfrac{d}{dt}\phi_{qr} + \omega_r \phi_{dr} \end{cases} \qquad \text{IV} - 1$$

When the direct stator flux ϕ_{ds} is held constant at ϕ_s, the quadrature stator flux ϕ_{qs} becomes zero, and with the resistance R_s considered negligible—a typical assumption for high-power wind energy machines—the machine's voltage equations can be simplified as follows.

$$\begin{cases} V_{ds} = 0 \\ V_{qs} = V_s = \omega_s \phi_s \\ V_{dr} = R_r I_{dr} + \dfrac{d}{dt}\phi_{dr} - \omega_r \phi_{qr} \\ V_{qr} = R_r I_{qr} + \dfrac{d}{dt}\phi_{qr} + \omega_r \phi_{dr} \end{cases} \quad \text{IV} - 2$$

Similar to the tensions, the equations for the flux are as follows:

$$\begin{cases} \phi_{ds} = \phi_s = l_s I_{ds} + l_m I_{dr} \\ \phi_{qs} = 0 = l_s I_{qs} + l_m I_{qr} \\ \phi_{dr} = l_r I_{dr} + l_m I_{ds} \\ \phi_{qr} = l_r I_{qr} + l_m I_{qs} \end{cases} \quad \text{IV} - 3$$

IV.2.1 Stator–Rotor Current Relationship under SFOC

According to Equations IV-3 for the direct and quadrature components of the stator flux, the correlations between the stator and rotor currents can be articulated as:

$$\begin{cases} I_{ds} = \dfrac{\Phi_s}{l_s} - \dfrac{l_m}{l_s} I_{dr} \\ I_{qs} = -\dfrac{l_m}{l_s} I_{qr} \end{cases} \quad \text{IV} - 4$$

IV.2.2 Stator Power–Rotor Current Relationship under SFOC

In a two-phase reference frame, the stator's active and reactive power in an asynchronous machine can be articulated as follows:

$$\begin{cases} P_s = V_{ds} I_{ds} + V_{qs} I_{qs} \\ Q_s = V_{qs} I_{ds} - V_{ds} I_{qs} \end{cases} \quad \text{IV} - 5$$

In a SFOC, this system of equations reduces to the form:

$$\begin{cases} P_s = V_s I_{qs} \\ Q_s = V_s I_{ds} \end{cases} \quad \text{IV} - 6$$

Incorporating the formulae for the direct and quadrature stator currents into the equations for active and reactive power yields the following results:

$$\begin{cases} P_s = -\dfrac{l_m V_s}{l_s} I_{qr} \\ Q_s = \dfrac{{V_s}^2}{\omega_s l_s} - \dfrac{l_m V_s}{l_s} I_{dr} \end{cases} \quad \text{IV} - 7$$

Expression IV-7 demonstrates a distinct separation between the control of stator active and reactive power. Assuming constant magnetizing inductance and a robust grid, the stator active power is directly proportional to the q-axis component of the rotor current. Conversely, the reactive

power is ascertained by the d-axis component of the rotor current, supplemented by an offset term influenced by the grid conditions.

IV.2.3 Rotor Voltage–Current Relationship under SFOC

Substituting the system of equations IV-4 into IV-3, the rotor flux expressions can be written as:

$$\begin{cases} \phi_{dr} = \left(l_r - \frac{{l_m}^2}{l_s}\right) I_{dr} + \frac{l_m V_s}{l_s \omega_s} \\ \phi_{qr} = \left(l_r - \frac{{l_m}^2}{l_s}\right) I_{qr} \end{cases} \quad \text{IV} - 8$$

$$\begin{cases} V_{dr} = R_r I_{dr} + \left(l_r - \frac{{l_m}^2}{l_s}\right)\frac{d}{dt} I_{dr} - g\omega_s \left(l_r - \frac{{l_m}^2}{l_s}\right) I_{qr} \\ V_{qr} = R_r I_{qr} + \left(l_r - \frac{{l_m}^2}{l_s}\right)\frac{d}{dt} I_{qr} + g\omega_s \left(l_r - \frac{{l_m}^2}{l_s}\right) I_{dr} + g\frac{l_m V_s}{l_s} \end{cases} \quad \text{IV} - 9$$

In steady state, the derivatives of the two-phase rotor currents become zero, allowing them to be expressed as:

$$\begin{cases} V_{dr} = R_r I_{dr} - g\omega_s \left(l_r - \frac{{l_m}^2}{l_s}\right) I_{qr} \\ V_{qr} = R_r I_{qr} + g\omega_s \left(l_r - \frac{{l_m}^2}{l_s}\right) I_{dr} + g\frac{l_m V_s}{l_s} \end{cases} \quad \text{IV} - 10$$

Applying the Laplace transform to these two equations gives us:

$$\begin{cases} V_{dr} = \left[R_r + \left(l_r - \frac{{l_m}^2}{l_s}\right) p\right] I_{dr} - g\omega_s \left(l_r - \frac{{l_m}^2}{l_s}\right) I_{qr} \\ V_{qr} = \left[R_r + \left(l_r - \frac{{l_m}^2}{l_s}\right) p\right] I_{qr} + g\omega_s \left(l_r - \frac{{l_m}^2}{l_s}\right) I_{dr} + g\frac{l_m V_s}{l_s} \end{cases} \quad \text{IV} - 11$$

$$\sigma l_r = \left(l_r - \frac{{l_m}^2}{l_s}\right) \quad \text{IV} - 12$$

Where:

V_{dr} and V_{qr} are the two-phase rotor voltage components applied to the machine to produce the desired rotor currents.

$g\omega_s \left(l_r - \frac{{l_m}^2}{l_s}\right)$ is the coupling term between the two axes, it represents an electromotive force dependent on the rotational speed.

The term g represents the slip in an asynchronous machine.

Equation IV-11 indicates that the SFOC method entails the regulation of active and reactive powers P_s and Q_s via the rotor voltage components V_{dr} and V_{qr}.

Utilizing equations IV-7 and IV-11, the block diagram of the DFIG can be constructed, as illustrated in Figure IV-1.

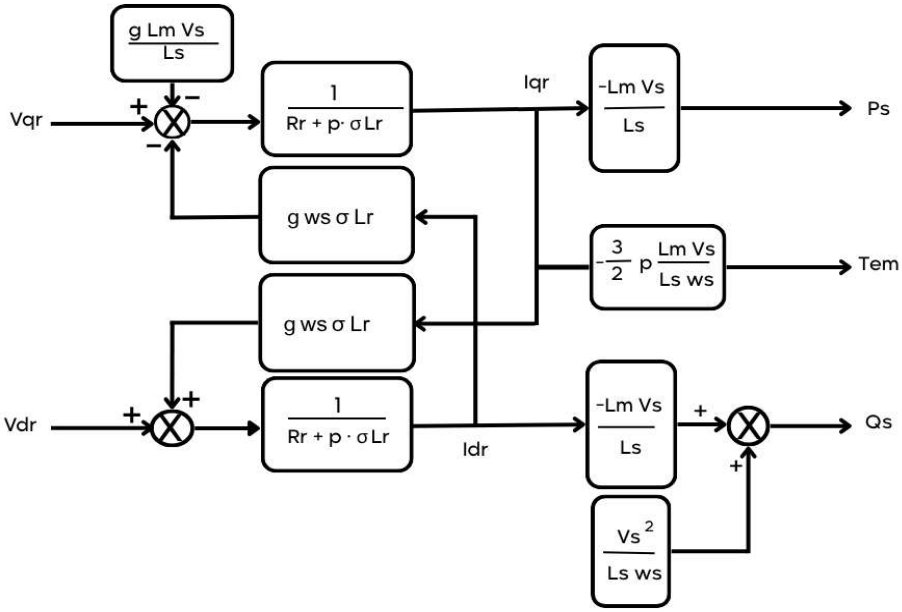

Figure IV-1 : Block Diagram of the Simplified DFIG Model

From this block diagram, it's clear that rotor currents relate to active and reactive powers via the term $\frac{l_m V_s}{l_s}$. The model exhibits nonlinear behavior due to the presence of the coupling terms $g\omega_s \left(l_r - \frac{{l_m}^2}{l_s}\right) I_{rd}$ and $g\omega_s \left(l_r - \frac{{l_m}^2}{l_s}\right) I_{rq}$. These terms are generally regarded as disturbances that must be compensated to achieve decoupled control, thereby eliminating the interactions between the direct and quadrature power components

To implement closed-loop control, a controller is used to ensure zero steady-state error and a satisfactory dynamic response.

IV.3 Implementation of the GWO Algorithm in the Simulation

The GWO is employed as an offline optimization technique to determine the optimal parameters of the proposed controllers prior to the dynamic simulation of the DFIM-based WECS. The optimization is performed externally in MATLAB, while the optimized parameters are subsequently implemented in the Simulink model to evaluate the system performance under different operating conditions.

The implementation procedure consists of the following steps:

1. **Initialization of the search agents:**

A population of grey wolves is randomly generated, where each wolf represents a candidate solution containing a set of controller parameters. For the PI controller, the decision variables are the proportional and integral gains (k_p, k_i). For the FPD controller, the decision variables include the input scaling factor (G_e), the change-in-error scaling factor (G_{ce}), and the output scaling factor (G_u). For the FPD+I controller, the decision variables comprise the input scaling factor (G_e), the change-in-error scaling factor (G_{ce}), the integral-error scaling factor (G_{ie}), and the output scaling factor (G_u).

2. **Definition of the objective function:**

Each candidate solution is assessed using the Integral of Time-weighted Absolute Error (ITAE), defined in Equation (III-13), where e(t) represents the active- or reactive-power tracking error. Minimizing the ITAE improves transient performance by reducing overshoot, oscillations, settling time, and steady-state error.

3. **Fitness evaluation:**

The controller parameters represented by each wolf are applied to the SFOC controller, and the Simulink model is executed over the specified simulation interval. The resulting ITAE value is assigned as the fitness of the corresponding wolf.

4. **Position updating:**

After evaluating all search agents, the three best solutions are identified as the alpha, beta, and delta wolves. The remaining wolves update their positions according to the standard GWO update equations, balancing exploration and exploitation throughout the search process.

5. **Termination of optimization:**

The optimization process continues until the maximum number of iterations is reached or the improvement in the objective function becomes negligible. The parameter set corresponding to the alpha wolf is selected as the optimal solution.

6. **Performance evaluation:**

The optimized controller gains are then fixed and inserted into the Simulink model. The optimization algorithm is no longer executed during the simulation. Instead, the WECS operates using these optimal parameters under different operating conditions, including constant wind speed, variable wind speed, and robustness tests involving parameter uncertainties and external disturbances.

Consequently, the GWO algorithm serves exclusively as an offline parameter-tuning method, while the dynamic simulations assess the real-time behavior of the DFIM-based WECS using the

optimized controller parameters. This strategy eliminates the computational burden of online optimization while ensuring high controller performance.

IV.3.1 SFOC Based on PI-GWO Controllers

Proportional–integral (PI) controllers are widely employed in industrial process regulation due to their simple structure and reliable performance under various operating conditions. However, their linear nature may limit their effectiveness when dealing with highly nonlinear systems.

As shown in Figure IV-2, SFOC of a DFIG operating in generator mode employs separate PI controllers for each axis. These controllers independently regulate active and reactive power by minimizing the error between reference and measured values. The proportional k_p and integral k_i gains of each controller are tuned offline using the GWO algorithm.

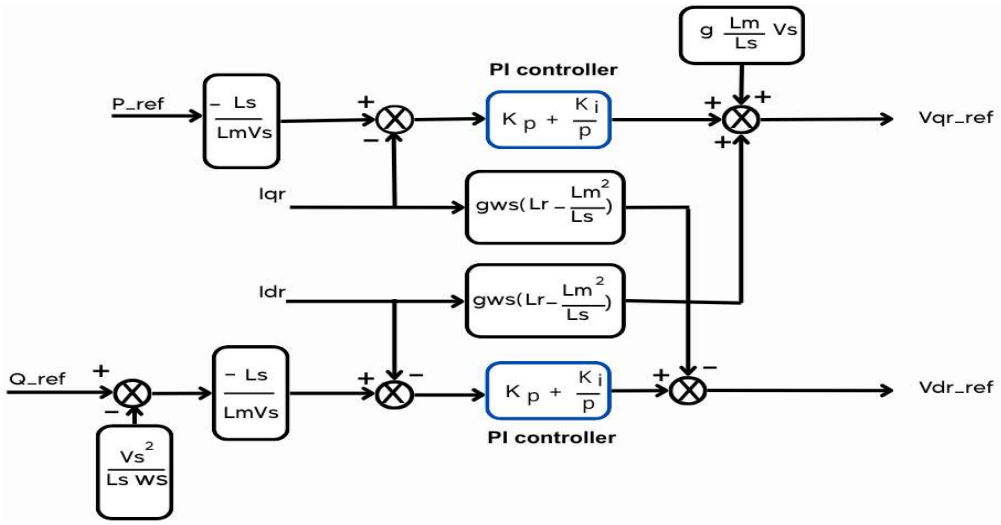

Figure IV-2 : PI Control

IV.3.1.1 Simulation Results for Constant Speed

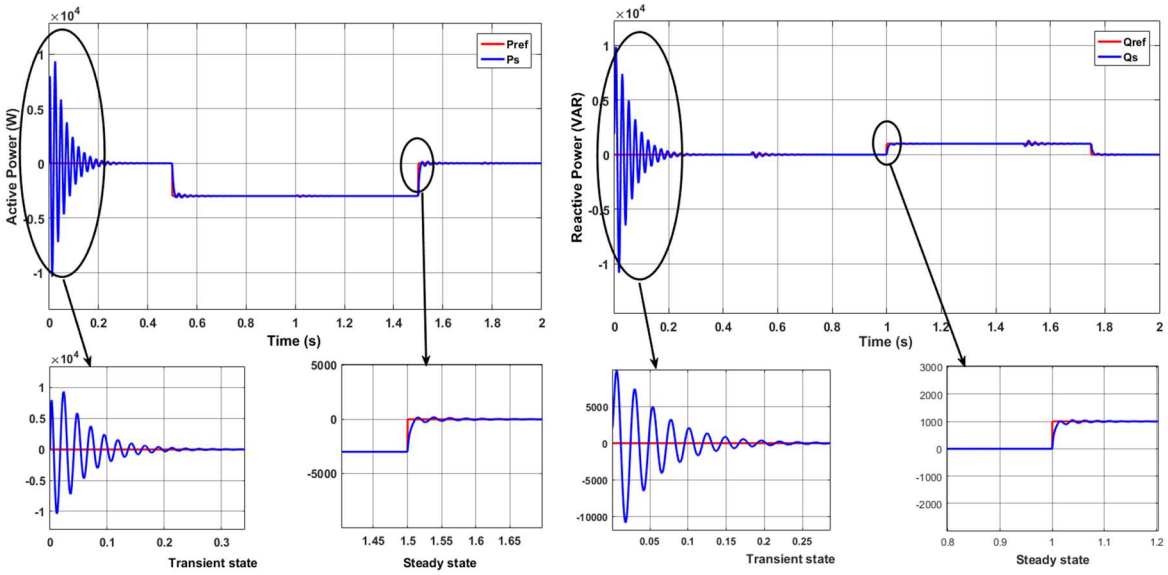

Figure IV-3: Stator Power Response Using PI–GWO Controller at Constant Wind Speed

IV.3.1.2 Interpretation of Results

At a constant rotational speed of 1440 rpm, the PI–GWO controller exhibits noticeable overshoot and relatively slow dynamic behavior when subjected to step changes in active and reactive power. Following the disturbance at t=0.5 s, a significant overshoot occurs, and the system requires approximately 0.15 s to reach steady state. Although the steady-state error remains negligible, the transient response is slower compared to fuzzy-based control approaches.

IV.3.1.3 Simulation Results for Variable Speed

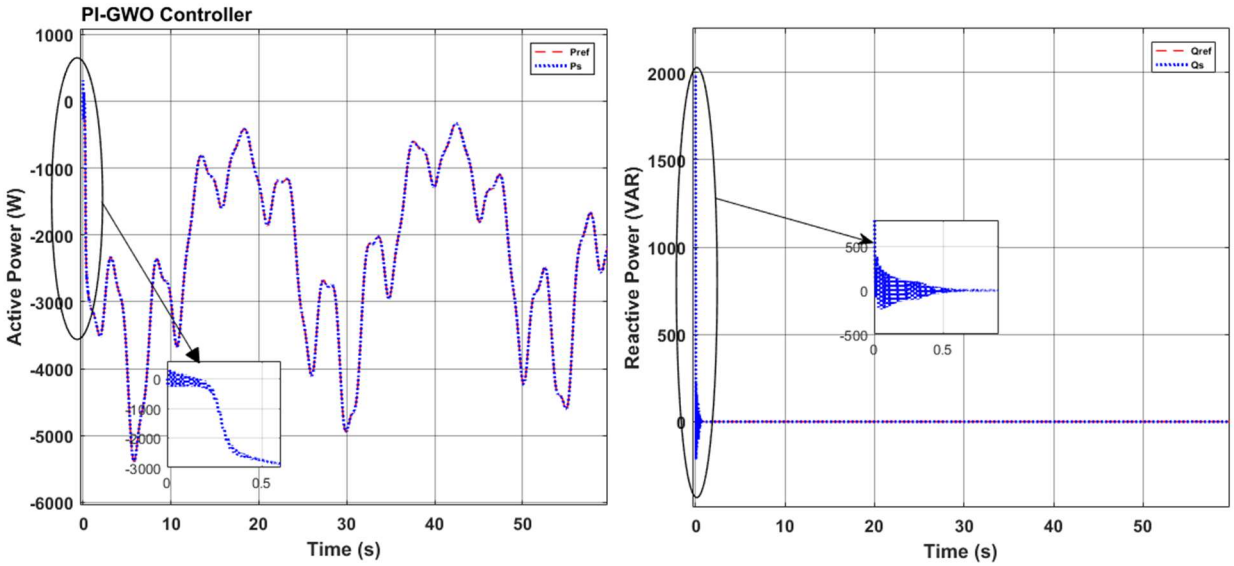

Figure IV-4 : Stator Power Response Using PI–GWO Controller at Variable Wind Speed

IV.3.1.4 Interpretation of Results

In the 60-second variable-wind simulation, the PI controller follows the general power trend but exhibits noticeable tracking errors and oscillations. The results clearly indicate that more advanced controllers can better smooth active and reactive power fluctuations—an essential factor for grid stability—whereas the PI controller is more sensitive to wind-induced variations. Thus, under variable-speed conditions, the PI controller remains functional but provides the lowest robustness and power quality.

IV.3.2 Optimal Fuzzy Control Using GWO

The membership functions of the input and output variables are depicted in Figures IV-5 and IV-6, respectively. The error signal is represented using one triangular and two trapezoidal membership functions, while the change in error is described by two trapezoidal membership functions. The output variables are modeled using six triangular membership functions.

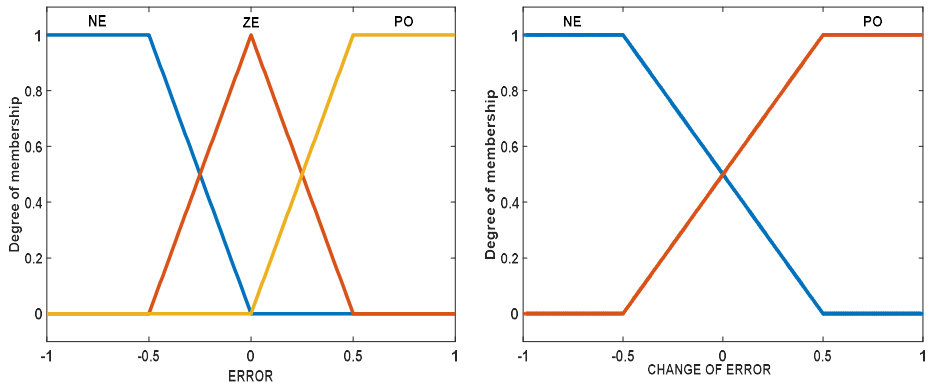

Figure IV-5 : Membership Function for Input Variables

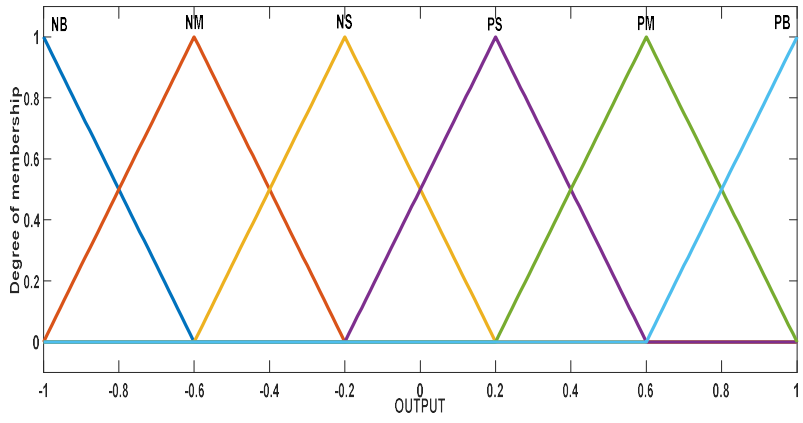

Figure IV-6 : Membership Function for Output Variable

The number of membership functions assigned to the input variables is deliberately minimized to ensure a simple yet effective controller design, resulting in a compact rule base consisting of six rules (Table IV-1). This approach captures the essential nonlinear control

behavior required for reliable power regulation while reducing computational burden, making it well suited for potential real-time implementation.

Table IV-1: Fuzzy Control Rules

Δe \ e	NE	ZE	PO
NE	NB	NM	PS
PO	NS	PM	PB

A Mamdani-type if–then inference structure is adopted, based on system knowledge and expert experience. The fuzzy inference system employs a modified product–sum–centroid (center of gravity) method to reduce computational cost and mitigate nonlinear effects [92].

Figure IV-7 illustrates the output surface obtained using the MATLAB/Simulink Fuzzy Logic Toolbox.

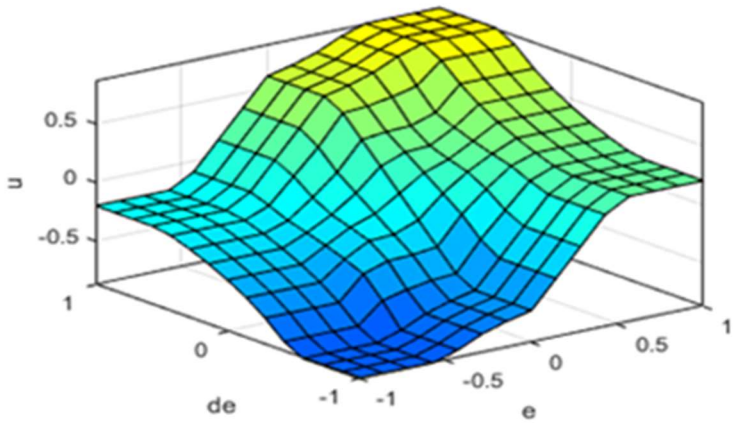

Figure IV-7 : Structure of the Fuzzy Controller Membership Function

IV.3.3 SFOC Based on FPD-GWO Controllers

To enhance the tracking performance of active and reactive power references, two fuzzy PD controllers are employed, as illustrated in Figure IV-8.

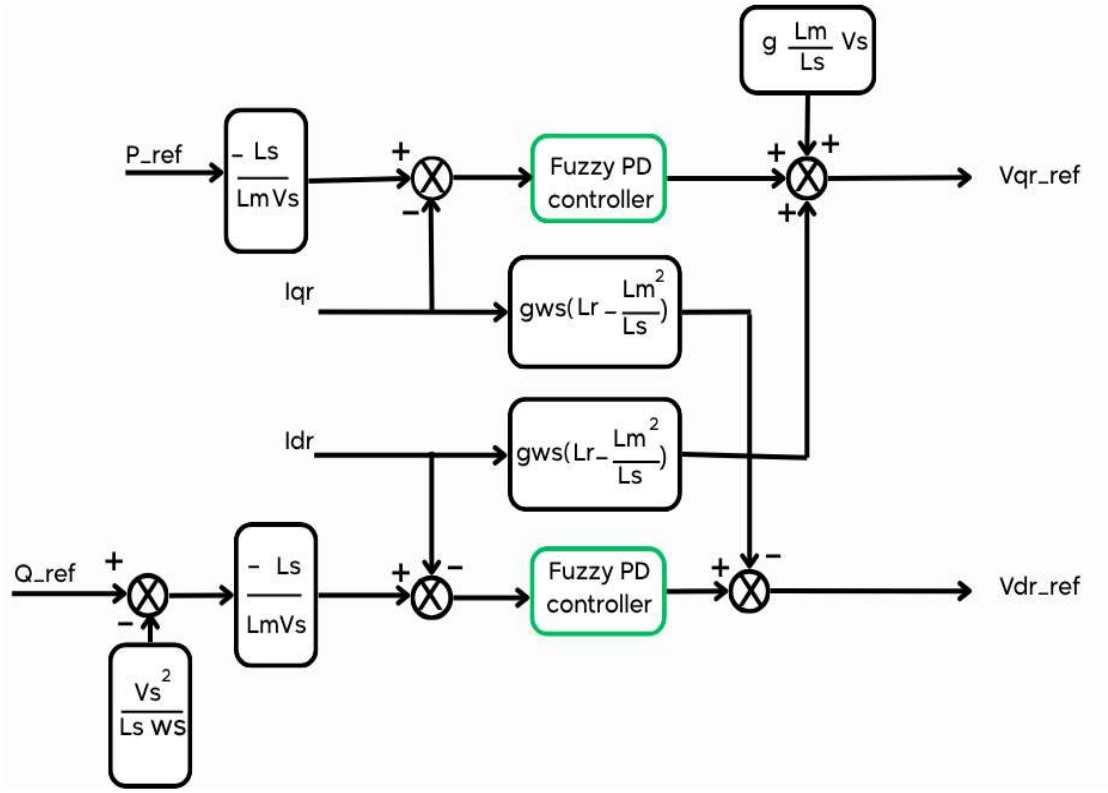

Figure IV-8 : Fuzzy PD Control

IV.3.3.1 Simulation Results for Constant Speed

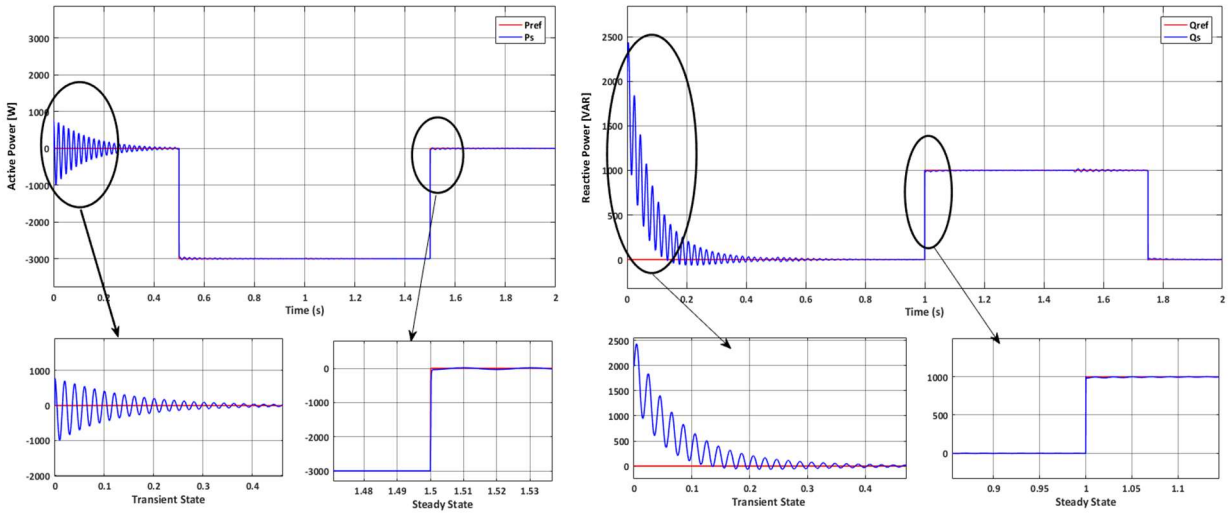

Figure IV-9 : Stator Power Response Using FPD-GWO Controller at Constant Wind Speed

IV.3.3.2 Interpretation of Results

The fuzzy PD controller reduces overshoot and improves the transient response by decreasing the response time. It is well suited for systems requiring rapid variations due to its fast-dynamic behavior and high tracking performance; however, it may exhibit a steady-state error.

IV.3.3.3 Simulation Results for Variable Speed

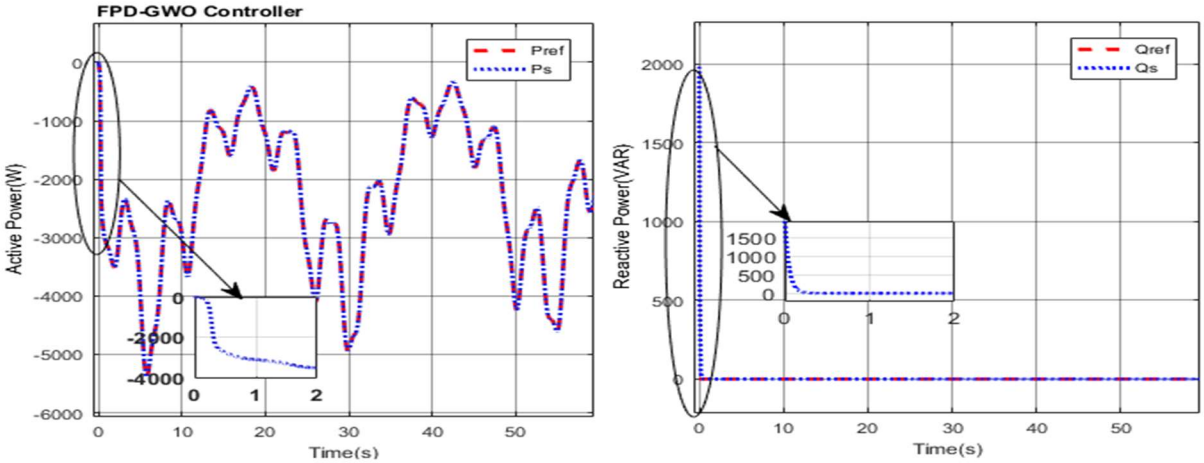

Figure IV-10 : Stator Power Response Using FPD–GWO Controller at Variable Wind Speed

IV.3.3.4 Interpretation of Results

Under variable wind conditions, the Fuzzy PD–GWO controller improves the dynamic tracking of stator power but still exhibits noticeable deviations from the reference. Although it responds rapidly, it does not fully eliminate steady-state and low-frequency errors as wind conditions vary.

IV.3.4 SFOC Based on FPD+I-GWO Controllers

The application of GWO for tuning the proposed fuzzy PD+I controller is illustrated in Figure IV-11. To enhance the tracking performance of active and reactive power references, the proposed fuzzy PD+I controllers are implemented within the study system using the SFOC strategy, as shown in Figure IV-12.

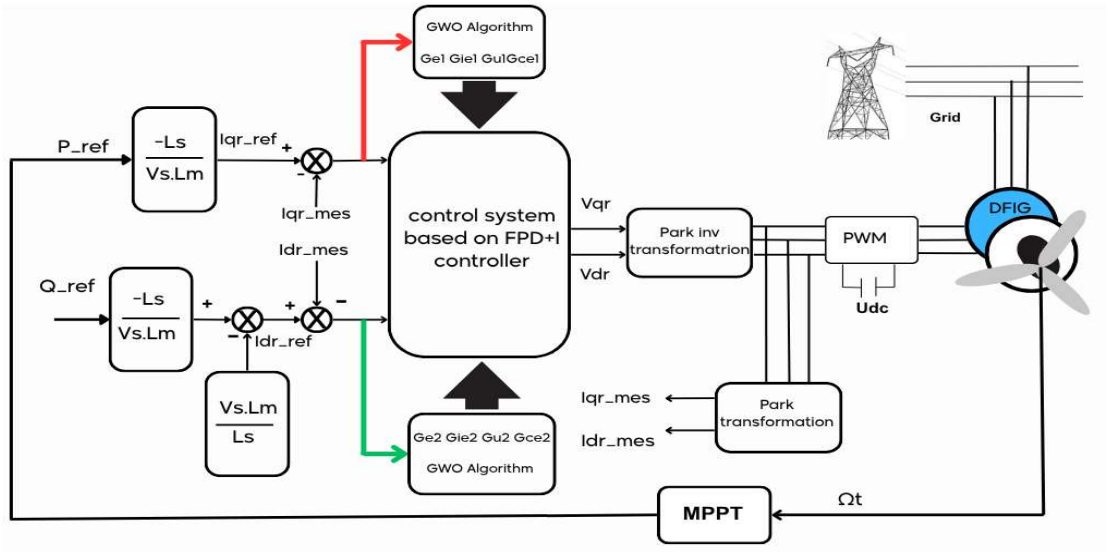

Figure IV-11 : Fuzzy PD+I-GWO Control

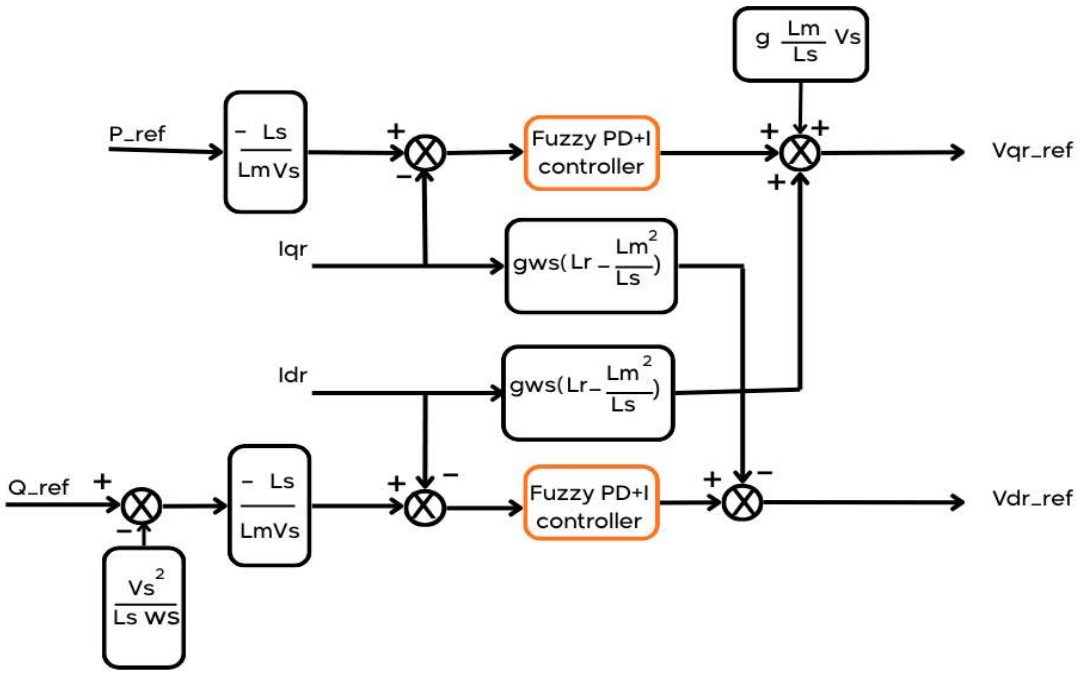

Figure IV-12 : Fuzzy PD+I Control

IV.3.4.1 Simulation Results for Constant Speed

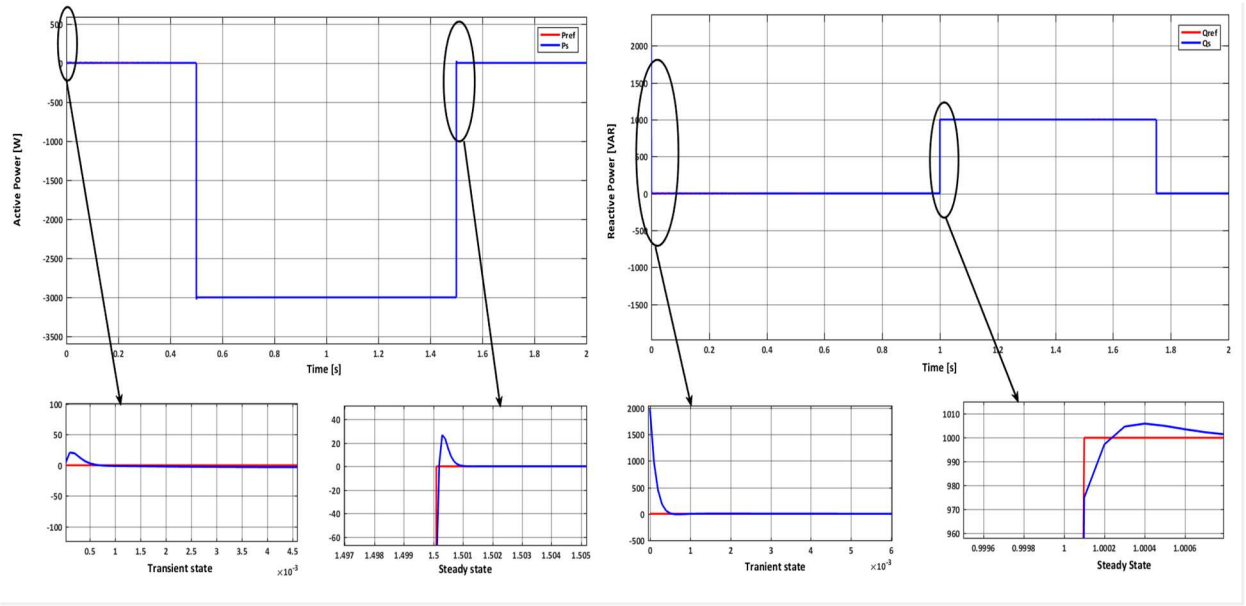

Figure IV-13 : Stator Power Response Using FPD+I-GWO Controller at Constant Wind Speed

IV.3.4.2 Interpretation of Results

The best performance is achieved by the hybrid fuzzy PD+I–GWO controller. It tracks the reference signals with negligible overshoot and a settling time of less than 0.05 s under constant speed conditions, exhibiting near critically damped behavior.

IV.3.4.3 Simulation Results for Variable Speed

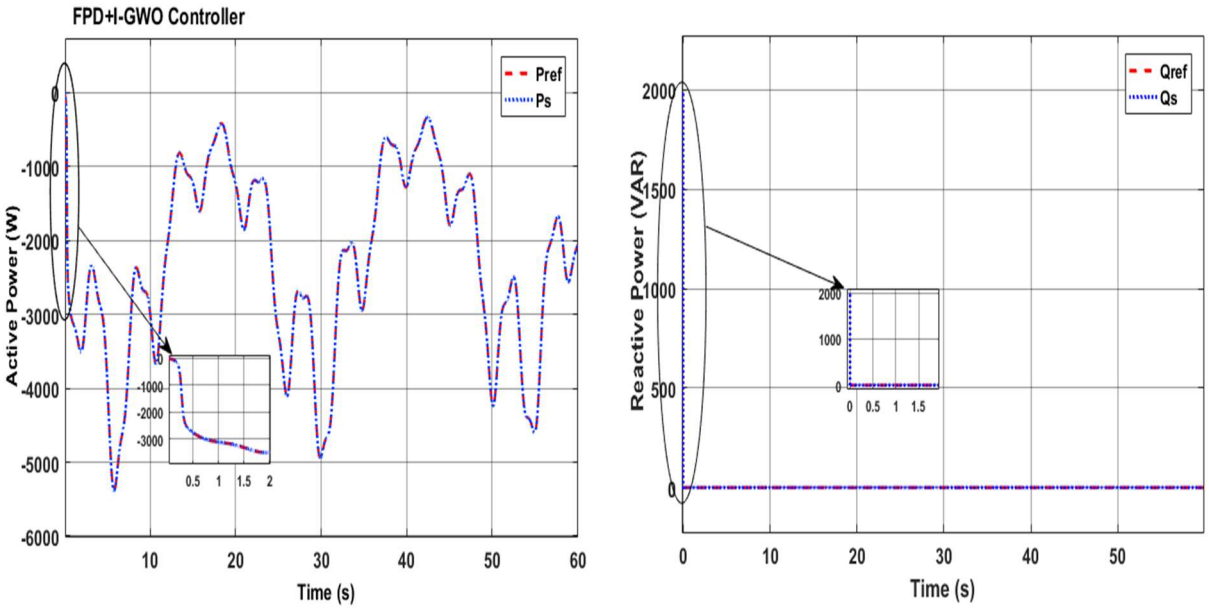

Figure IV-14 : Stator Power Response Using FPD+I-GWO Controller at Variable Wind Speed

IV.3.4.4 Interpretation of Results

Under the same 60-second variable wind-speed profile, the fuzzy PD+I–GWO controller demonstrates improved tracking accuracy and enhanced stability, even under realistic and fluctuating operating conditions. It effectively maximizes energy capture in the partial-load region while ensuring smooth and constant power output.

IV.4 Comparative Analysis and Control Performance

IV.4.1 Qualitative Comparisons

IV.4.1.1 Interpretation of Results

The comparative analysis of the PI–GWO, fuzzy PD–GWO, and fuzzy PD+I–GWO controllers reveals significant differences in both dynamic performance and numerical effectiveness. From a qualitative standpoint, the PI–GWO controller exhibits a slow response, pronounced overshoot, and a relatively long settling time, which limits its performance under rapid system variations. The fuzzy PD–GWO controller improves the transient response by enabling faster tracking and reducing oscillations due to its nonlinear structure; however, it still presents noticeable steady-state errors. In contrast, the proposed fuzzy PD+I–GWO controller achieves near-critically damped behavior, with minimal overshoot, an extremely fast settling time (below 0.05 s), and accurate tracking performance under both steady-state and variable wind conditions, as illustrated in Figures IV-3, IV-4, IV-9, IV-10, IV-13, and IV-14.

IV.4.2 Quantitative Comparisons

This test focuses on four main criteria: the integral of squared error (ISE), the integral of absolute error (IAE), the integral of time-weighted squared error (ITSE), and the integral of time-weighted absolute error (ITAE). All results are obtained under identical operating conditions. The performance indices are mathematically defined as follows:

The Integral of Squared Error:

$$ISE = \int_0^T e(t)^2\, dt \qquad \text{IV} - 13$$

The Integral of Absolute Error:

$$IAE = \int_0^T |e(t)| dt \qquad \text{IV} - 14$$

The Integral of Time-weighted Squared Error:

$$ITSE = \int_0^T t.e(t)^2 dt \qquad \text{IV} - 15$$

The Integral of Time-weighted Absolute Error:

$$ITAE = \int_0^T t.|e(t)|dt \qquad \text{IV} - 16$$

IV.4.2.1 Simulation Results

Table IV-2: Performance Index of Active and Reactive Power

Power	Index criteria	PI-GWO	FPD-GWO	FPD+I-GWO
Active	ISE	20.98	0.13620	0.00674
	IAE	1.459	0.18300	0.00274
	ITSE	0.996	0.01523	0.00654
	ITAE	0.162	0.04281	0.00179
Reactive	ISE	21.52	1.17700	0.00999
	IAE	1.424	0.36470	0.00361
	ITSE	0.659	0.03163	0.00102
	ITAE	0.113	0.03910	0.00093

IV.4.2.2 Interpretation of Results

The numerical results presented in Table IV-2 confirm the outperformance of the fuzzy PD+I–GWO controller through a significant reduction in all performance indices. The ITAE for active power decreases from 0.162 (PI–GWO) to 0.04281 (fuzzy PD–GWO), and further to 0.00179 with the fuzzy PD+I–GWO controller, corresponding to an improvement of approximately 98.9% relative to the PI–GWO case. Similarly, the ISE is reduced from 20.98 to 0.00674, while the IAE decreases from 1.459 to 0.00274, indicating a substantial reduction in tracking errors. For reactive power, the ITAE decreases from 0.113 (PI–GWO) to 0.00093 with the fuzzy PD+I–GWO controller. Overall, these quantitative results clearly demonstrate that the proposed fuzzy PD+I–GWO controller achieves superior accuracy and significantly lower error indices compared with the other evaluated control strategies.

IV.5 Optimality and Robustness Analysis

IV.5.1 Optimality Analysis

IV.5.1.1 Simulation Results

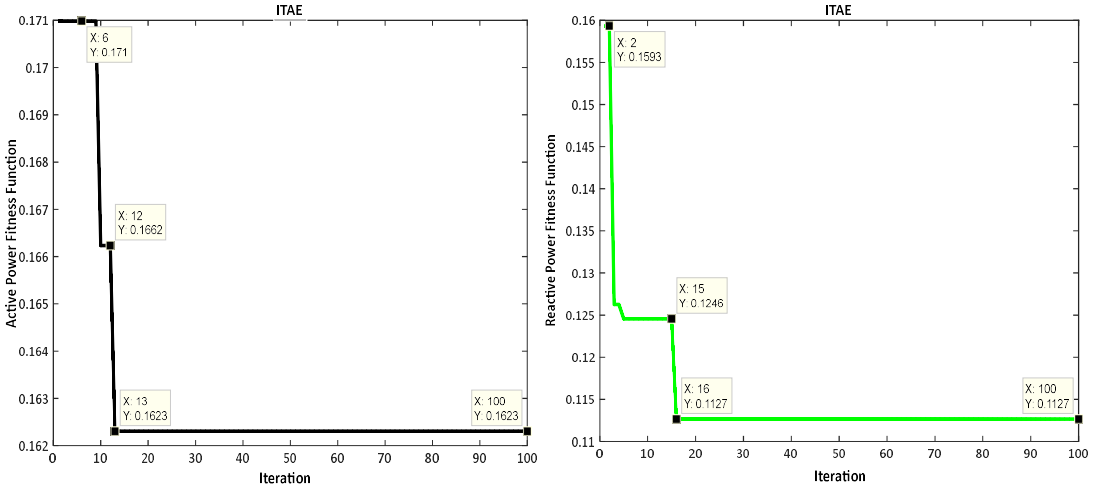

Figure IV-15 : ITAE-Based Performance Evaluation of the PI-GWO Controller

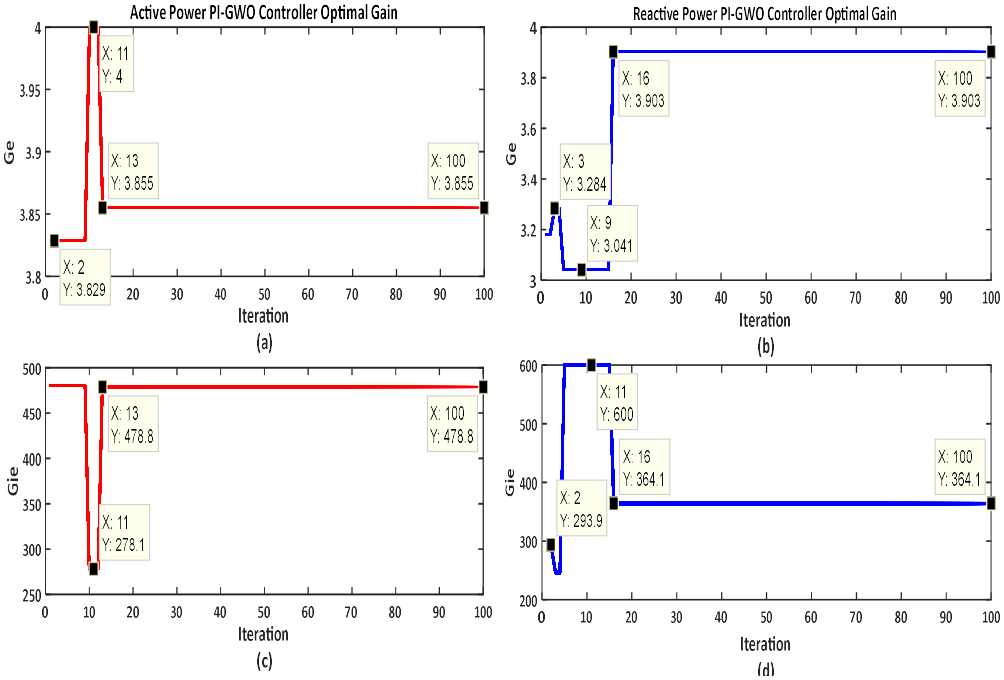

Figure IV-16 : PI-GWO Controller Gains Determined via Offline Optimization

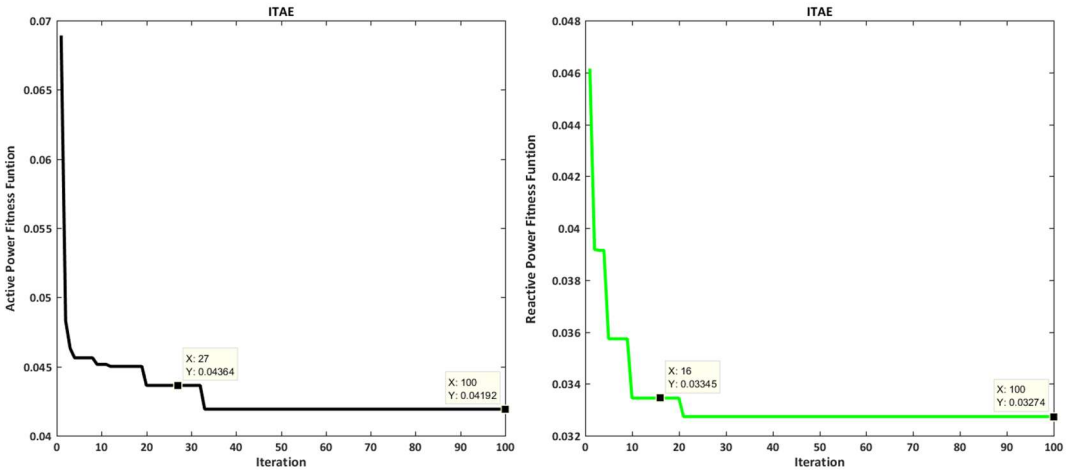

Figure IV-17 : ITAE-Based Performance Evaluation of the FPD-GWO Controller

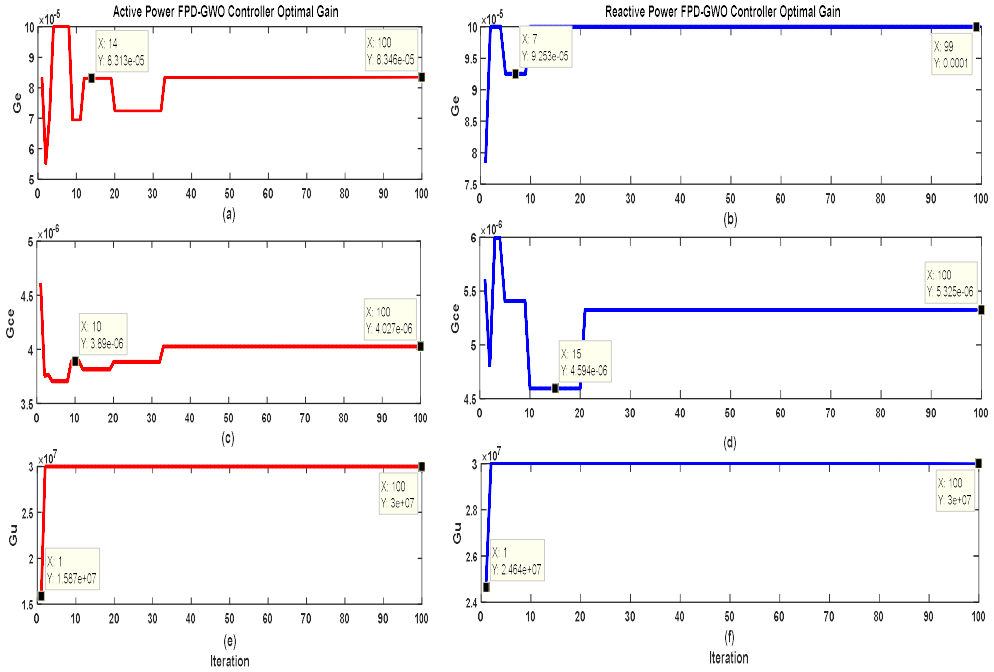

Figure IV-18 : FPD-GWO Controller Gains Determined via Offline Optimization

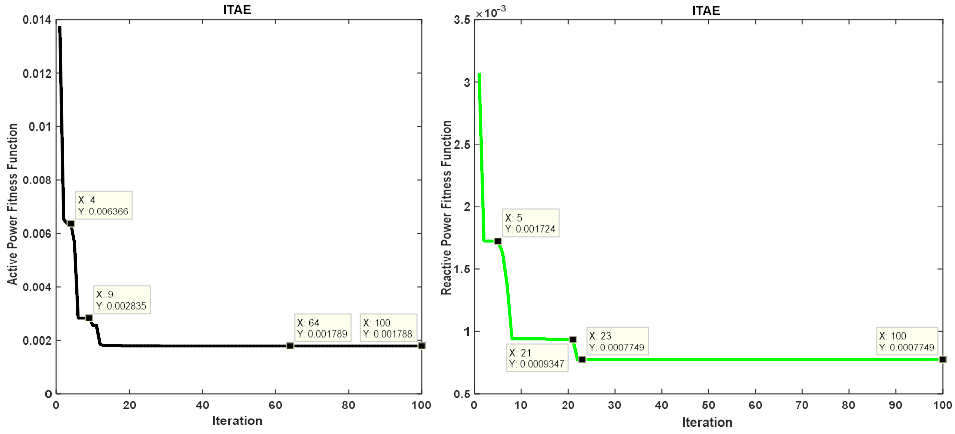

Figure IV-19 : ITAE-Based Performance Evaluation of the FPD+I-GWO Controller

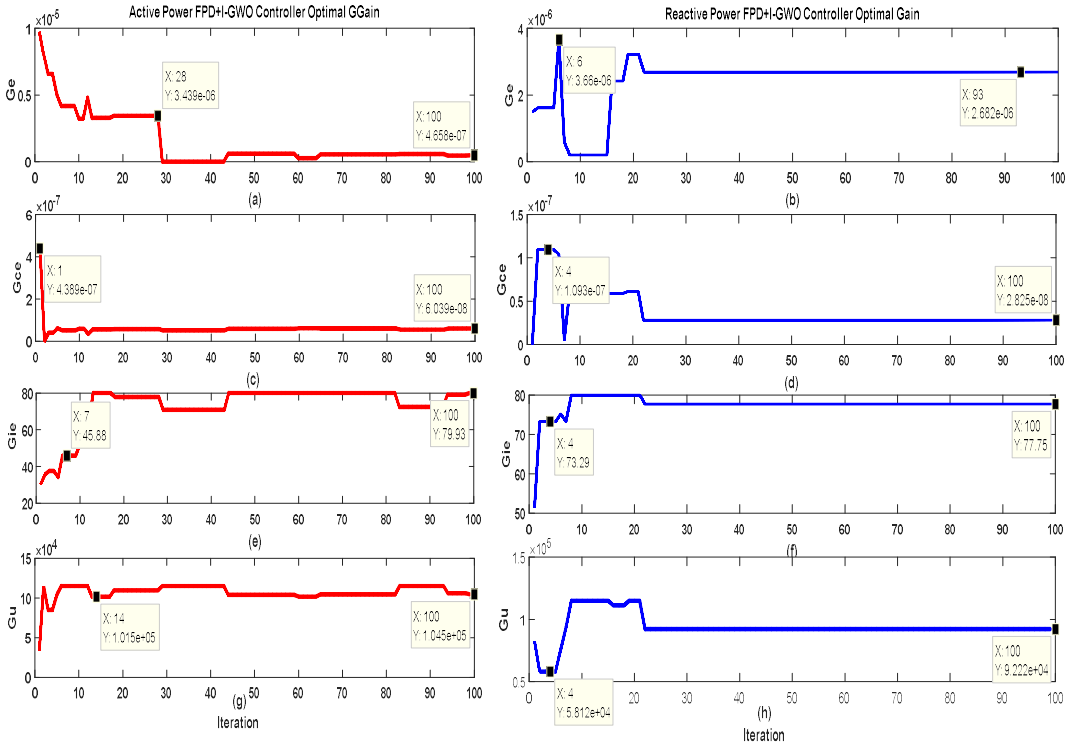

Figure IV-20 : FPD+I-GWO Controller Gains Determined via Offline Optimization

Table IV-3: Optimal Gains of Controllers

Power	Gain	PI-GWO	FPD-GWO	FPD+I-GWO
Active	Ge1	3.855	9.00E-05	3.83E-07
	Gie1	478.8	-----	7.26E+1
	Gce1	-----	4.04E-06	5.47E-08
	Gu1	-----	29977814	1.14E+05
Reactive	Ge2	3.903	1.00E-4	7.52E-07
	Gie2	364.1	----	7.75E+01
	Gce2	----	5.35E-06	5.92E-08
	Gu2	----	29933834.6	1.14E+05

IV.5.1.2 Interpretation of Results

The efficacy of the suggested control approach is guaranteed by employing the GWO algorithm for offline adjustment of the controller gains. The convergence characteristics of the fitness function, determined by the Integral of Time-weighted Absolute Error (ITAE), are depicted in Figures IV-15, IV-17, and IV-19 for the PI-GWO, Fuzzy PD-GWO, and Fuzzy PD+I-GWO controllers, respectively. The data illustrates the progression of the ITAE across 100 iterations with a population of 10 grey wolves, where each iteration represents a simulation period of 2 seconds, so assuring a uniform assessment of controller efficacy.

In all cases, the ITAE decreases progressively as the iterations advance, confirming the effectiveness of the GWO algorithm in exploring and exploiting the search space. However, the convergence behavior differs among the controllers: the PI-GWO exhibits slower convergence and stabilizes at a higher ITAE value, whereas the Fuzzy PD-GWO achieves faster convergence and lower error levels. The proposed Fuzzy PD+I-GWO controller shows the fastest convergence and reaches the minimum ITAE, demonstrating superior optimization efficiency and the ability to identify near-optimal gain values. This is further supported by the gain evolution shown in Figures IV-16, IV-18, and IV-20, as well as the optimal parameters reported in Table IV-3, which ensure enhanced dynamic performance with reduced implementation complexity.

IV.5.2 Robustness Analysis

IV.5.2.1 Interpretation of Results

The robustness of the proposed Fuzzy PD+I-GWO controller is validated through both qualitative and quantitative analyses. As shown in Table IV-2, the controller achieves the lowest performance indices (ISE, IAE, ITSE, and ITAE) for both active and reactive power, indicating superior error minimization and strong disturbance rejection capability. Furthermore, the dynamic responses presented in Figures IV-3, IV-4, IV-9, IV-10, IV-13, and IV-14 demonstrate that the controller maintains accurate reference tracking with negligible overshoot and a very fast settling time under both step changes and variable wind conditions.

This constant performance underscores the controller's capacity to adeptly manage system nonlinearities, parameter uncertainties, and external disturbances. Thus, the suggested methodology guarantees significant resilience, rendering it a dependable and effective solution for DFIG-based WECSs.

IV.6 Conclusion

This chapter applies three types of controllers: PI, Fuzzy PD, and Fuzzy PD+I to the system under both constant and variable wind speed situations utilizing SFOC and the GWO algorithm. The results obtained are simulated using MATLAB/Simulink, thereafter evaluated, compared, and interpreted.

The suggested Fuzzy PD+I–GWO controller exhibits enhanced performance relative to the PI-GWO and Fuzzy PD-GWO approaches. It achieves the lowest error indices, fastest convergence, and excellent dynamic behavior with negligible overshoot and rapid settling time. The results confirm its strong robustness, accurate tracking capability, and effectiveness in handling nonlinearities, uncertainties, and wind variations in DFIG-based WECSs, establishing it as a dependable solution for practical applications.

General Conclusion

In the context of the ongoing global transition toward sustainable and low-carbon energy systems, renewable energy sources – particularly wind energy – have become essential for meeting the increasing electricity demand while mitigating environmental impacts. However, the inherent intermittent nature of wind and the complex nonlinear behavior of modern WECSs, especially those based on DFIGs, present significant challenges in terms of control, stability, and power quality.

This thesis has addressed these challenges by proposing an advanced and robust control strategy aimed at enhancing the performance of DFIG-based WECS functioning under fluctuating wind conditions. This study's main contribution is the creation of a hybrid intelligent controller that combines a fuzzy PD+I structure with the GWO for effective offline adjustment of controller settings. This method utilizes the nonlinear processing skills of fuzzy logic alongside the effective global search capabilities of GWO.

The efficacy of the suggested control technique has been confirmed by extensive MATLAB/Simulink simulations. The results indicate a substantial enhancement in dynamic performance, characterized by rapid settling time, little overshoot, and precise tracking of active and reactive power during both step changes and genuine wind fluctuations. Furthermore, the significant reduction in performance metrics such as ITAE and ITSE confirms the resilience, accuracy, and dependability of the suggested strategy amidst system nonlinearities, parameter uncertainties, and external disturbances.

A salient benefit of the proposed approach is its pragmatic viability. The offline optimization process results in a controller that is both simple and efficient, and which is suitable for real-time implementation. This can be attributed to the fact that it circumvents the computational demands and the potential for instability that are concomitant with online adaptive or model-based control methodologies. This renders the proposed solution particularly attractive for industrial applications in modern wind farms.

This work contributes to the advancement of high-performance control techniques for renewable energy systems. Furthermore, it emphasizes the potential of hybrid intelligent optimization techniques in enhancing energy capture efficiency, improving power quality, and ensuring reliable grid integration. Moreover, the proposed methodology can be extended beyond wind energy systems to a broader class of nonlinear and uncertain electromechanical and energy systems.

In terms of future work, it is recommended that research be focused on real-time implementation and experimental validation using digital control platforms, hardware-in-the-loop (HIL) systems, or laboratory-scale prototypes. It is submitted that such investigations will facilitate

the evaluation of the performance of the controller under realistic operating conditions. The aforementioned conditions encompass disturbances in the grid, measurement noise and variations in parameters. This step is essential to bridge the gap between simulation and practical deployment, and to fully assess the robustness, reliability, and industrial applicability of the proposed approach.

Bibliographies

[1] International Energy Agency, "World Energy Outlook 2023," IEA, Paris, France, Rep. WEO-2023, Oct. 2023.

[2] S. Zhang, E. Robinson, and M. Basu, "Hybrid Gaussian process regression and Fuzzy Inference System based approach for condition monitoring at the rotor side of a doubly fed induction generator," *Renewable Energy,* vol. 198, pp. 936-946, Oct. 2022.

[3] Intergovernmental Panel on Climate Change, "Climate Change 2023: Synthesis Report," IPCC, Geneva, Switzerland, General Assembly Rep. AR6-SYR, Mar. 2023.

[4] International Renewable Energy Agency, "Renewable Energy Statistics 2023," IRENA, Abu Dhabi, UAE, Jul. 2023.

[5] T. F. Stocker, D. Qin, G. K. Plattner, M. Tignor, S. K. Allen, J. Boschung, A. Nauels, Y. Xia, V. Bex, and P. M. Midgley Eds, "Climate Change 2013: The Physical Science Basis," Cambridge, UK: Cambridge University Press, 2013.

[6] International Energy Agency, "Renewables 2023: Analysis and Forecast to 2028," IEA, Paris, France, Agency Rep. Renewables-2023, Jan. 2024.

[7] REN21, "Renewables 2023 Global Status Report – Global Overview," REN21 Secretariat, Paris, France, Rep. GSR-2023, Jun. 2023.

[8] M. J. B. Kabeyi, and O. A. Olanrewaju, "Sustainable Energy Transition for Renewable and Low Carbon Grid Electricity Generation and Supply," *Front. Energy Res.,* vol. 9, no. Art. no. 743114, Mar. 2022.

[9] T. Ackermann, Wind Power in Power Systems, 2nd ed. Chichester, UK: Wiley, 2012.

[10] Global Wind Energy Council, "Global Wind Report 2023," Brussels, Belgium, Policy Rep. GWR-2023, Mar. 2023.

[11] H. M. S. Jabr, "Doubly-fed induction generator used in wind energy," Ph.D. dissertation, Dept. Elect. Comput. Eng., Univ. of Windsor, Windsor, ON, Canada, 2008.

[12] F. Blaabjerg, M. Liserre, and K. Ma, "Power Electronics Converters for Wind Turbine Systems," *IEEE Trans. Ind. Appl.,* vol. 48, no. 2, p. 708–719, Mar./Apr. 2012.

[13] S. D. Ahmed, F. S. M. Al-Ismail, M. Shafiullah, F. A. Al-Sulaiman, and I. M. El-Amin, "Grid Integration Challenges of Wind Energy: A Review," *IEEE Access,* vol. 8, p. 10857–10878, 2020.

[14] R. Pena, J. C. Clare, and G. M. Asher, "Doubly Fed Induction Generator Using Back-to-Back PWM Converters," *IEE Proc. - Electr. Power Appl.,* vol. 143, no. 3, p. 231–241, May 1996.

[15] S. Heier, Grid Integration of Wind Energy: Onshore and Offshore Conversion Systems, 3rd ed., Chichester, Wiley UK: John Wiley & Sons, Ltd, 2014.

[16] G. Ofualagba, and EU. Ubeku, "Wind energy conversion system- wind turbine modeling," in *2008 IEEE Power and Energy Society General Meeting*, Pittsburgh, PA, USA, 2008, pp. 1–8.

[17] N. E. Mouhi, and A. Essadki, "Active and Reactive Power Control of DFIG used in WECS using PI Controller and Backstepping," in *2017 International Renewable and Sustainable Energy Conference (IRSEC)*, Tangier Morocco, 2017, pp. 1–6.

[18] D. Rekioua, N. Mezzai, Z. Mokrani, A. Oubelaid, K. Kakouche, P. O. Logerais, M. Alshareef, M. Bajaj, M. B. Tuka, and S. S. M. Ghoneim, "Effective optimal control of a wind turbine system with hybrid energy storage and hybrid MPPT approach," *Sci. Rep.,* vol. 14, no. 1, Art. no. 30013, Dec. 2024.

[19] B. Wu, Y. Lang, N. Zargari, and S. Kouro, Power Conversion and Control of Wind Energy Systems, Hoboken, NJ, USA: Wiley-IEEE Press, July 5, 2011.

[20] B. I. Saeed, and B. Mehrdadi, "Zero overshoot and fast transient response using a fuzzy logic controller," in *Proceedings of the 17th International Conference on Automation and Computing (ICAC)*, Huddersfield, UK, 2011, pp. 106–111.

[21] L. A. Zadeh, "Fuzzy Sets," *Inf. Control,* vol. 8, no. 3, p. 338–353, Jun. 1965.

[22] R. Rouabhi, A. Herizi, and A. Djerioui, "Performance of Robust Type-2 Fuzzy Sliding Mode Control Compared to Various Conventional Controls of Doubly-Fed Induction Generator for Wind Power Conversion Systems," *Energies,* vol. 17, no. 15, Art. no. 3778, Jul. 2024.

[23] A. Herizi, R. Rouabhi, F. Ouagueni, and A. Zemmit, "Robust Wind Power Control Using Sliding Mode, Backstepping and Fuzzy Logic," *Rev. Roum. Sci. Techn. – Électrotechn. et Énerg ,* vol. 70, no. 3, pp. 313-318, Aug. 2025.

[24] Y. Bekakra, and D. Ben Attous, "Optimal tuning of PI controller using PSO optimization for indirect power control for DFIG based wind turbine with MPPT," *Int. J. Syst. Assur. Eng. Manag.,* vol. 5, no. 3, pp. 219-229, Sept 2014.

[25] A. Guediri, M. Hettiri, and A. Guediri, "Modeling of a wind power system using the genetic algorithm based on a doubly fed induction generator for the supply of power to the electrical grid. Processes," *Processes,* vol. 11, no. 3, Art. no. 952, Mar. 2023.

[26] Z. Zeghdi, L. Barazane, and Y.Bekakra, "Improved backstepping control of a dfig based wind energy conversion system using ant lion optimizer algorithm," *Period. Polytech. Electr. Eng. Comput. Sci.,* vol. 66, no. 1, pp. 43-59, 2022.

[27] S. Mirjalili, S. M. Mirjalili, and A. Lewis, "Grey wolf optimizer," *Adv. Eng. Softw.,* vol. 69, pp. 46-61, Mar. 2014.

[28] M. Bouderbala, B. Bossoufi, A. Lagrioui, M. Taoussi, H. A. Aroussi, and Y. Ihedrane, "Direct and indirect vector control of a doubly fed induction generator based in a wind energy conversion system," *Int. J. Electr. Comput. Eng.,* vol. 9, no. 3, pp. 1531-1540, June 2018.

[29] B. Desalegn, D. Gebeyehu, and B. Tamrat, "Wind energy conversion technologies and engineering approaches to enhancing wind power generation : A review," *Heliyon,* vol. 8, no. 11, Art. no. e11263, Nov. 2022.

[30] IEEE, "Search results for 'Wind Energy' publications, 2010–2025," IEEE Xplore Digital Library, https://ieeexplore.ieee.org, accessed April 2026.

[31] Elsevier, "Search results for 'Wind Energy' publications, 2010–2025," ScienceDirect, https://www.sciencedirect.com., accessed April 2026.

[32] Springer Nature, "Search results for 'Wind Energy' publications, 2010–2025," https://link.springer.com, accessed April 2026.

[33] Global Wind Energy Council (GWEC), Global Wind Report 2026, Brussels, Belgium, Apr. 2026.

[34] J. Giri, N. K. Mishra, A. Patra, and M. K. Shukla, "Control Strategies of DFIG Technology-based Variable-Speed Wind Turbines-A Review," *IOP Conf. Ser.: Earth Environ. Sci.,* vol. 1285, no. 1, Art. no. 012007, Jan 2024.

[35] R. Ryndzionek, K. Blecharz, F. Kutt, M. Michna, and G. Kostro, "Development and performance analysis of a novel multiphase doubly-fed induction generator," *Arch. Electr. Eng.,* vol. 71, no. 4, p. 1003–1015, Dec. 2022.

[36] F. P. Deylami, and A.Darabi, "Steady-state performance analysis for optimal operation determination of doubly fed induction motors," *J. Eng.,* vol. 2023, no. 1, Art. no. e12220, Jan. 2023.

[37] C. Klumpner, "Analysing the converter requirements for a dual-fed induction machine based flywheel energy storage system," in *Proc. 10th Int. Conf. Power Electronics, Machines and Drives (PEMD 2020)*, 2020, pp. 684–689.

[38] G. Iwański, M. Piwek, and G. Dauksha, "Doubly Fed Induction Machine-Based DC Voltage Generator with Reduced Oscillations of Torque and Output Voltage," *Energies,* vol. 16, no. 2, art. no. 814, Jan. 2023.

[39] N. El Ouanjli, S. Motahhir, A. Derouich, A. Ghzizal, A. Chebabhi, and M. Taoussi, "Improved DTC strategy of doubly fed induction motor using fuzzy logic controller," *Energy Rep.,* vol. 5, p. 271–279, Nov. 2019.

[40] Z. Kara, and K. Barra, "Control of Doubly Fed Induction Generator Supplied via Matrix Converter for Wind Energy Conversion System," *Int. J. Mod. Nonlinear Theory Appl.,* vol. 3, no. 3, p. 98–112, Jul. 2014.

[41] W. Seubkinorn, and B. Neammanee, "Sliding Mode Control for Wind Turbine with Doubly Fed Induction Generators," *GMSARN Int. J.,* vol. 2, no. 1, p. 35–40, Mar. 2008.

[42] L. S. Barik, and H. Misra, "Control of wound rotor induction machine for Indian traction applications," in *Proceedings of the 2022 22nd National Power Systems Conference (NPSC)*, New Delhi, India, 2022, pp. 195-200.

[43] A. Banerjee, M. S. Tomovich, S. B. Leeb, and J. L. Kirtley, "Control Architecture for a Switched Doubly Fed Machine Propulsion Drive," *IEEE Trans. Ind. Appl.,* vol. 51, no. 2, p. 1538–1550, Mar./Apr. 2015.

[44] S. P. Mohapatra, and P. K. Dash, "A novel control strategy of a variable-speed doubly-fed-induction-generator-based wind energy conversion systemClean Energy," *Clean Energy,* vol. 8, no. 2, p. 153–170, Apr. 2024.

[45] R. K. Kumar, and J. Choudhary, "Design of a novel control scheme for the operation of the doubly fed induction generator," *Arch. Electr. Eng.,* vol. 73, no. 1, p. 373–392, May 2024.

[46] K. Ghefiri, S. Bouallègue, I. Garrido, A. J. Garrido, and J. Haggège, "Complementary power control for doubly fed induction generator-based tidal stream turbine generation plants," *Energies,* vol. 10, no. 7, art. no. 862, Jun. 2017.

[47] T. Feehally, and J. Apsley, "The Doubly Fed Induction Machine as an Aero Generator," *IEEE Trans. Ind. Appl.,* vol. 51, no. 4, p. 3462–3471, Jul./Aug. 2015.

[48] A. Radaideh, M. Bodoor, and A. Al-Quraan, "Active and reactive power control for wind turbines based DFIG using LQR controller with optimal gain-scheduling," *J. Electr. Comput. Eng.,* vol. 202, no. Art. no. 1218236, Oct. 2021.

[49] M. I. Abdelkader, A. K. Abdelsalam, and A. A. Hossameldin, "Indirect vector-controlled brushless doubly-fed twin-stator induction generator for wind energy conversion application," *Energies,* vol. 13, no. 16, p. 4174, Aug. 2020.

[50] R. K. Behara, and A. K. Saha, "Deep Q-Network Reinforcement Learning-Based Rotor Side Control System of a Grid-Integrated DFIG Wind Energy System Under Variable Wind Speed Conditions," *IEEE Access,* vol. 12, p. 184179–184205, 2024.

[51] C. Sun, C. Lu, Y. Wang, B. Zhang, H. Gao, and D.Xu, "Rotational Reference Frame Control of DFIG-Based Wind Turbines for Inertial Frequency Response," *IEEE Access,* vol. 12, p. 149606–149616, 2024.

[52] A. Maafa, H. Mellah, K. Benaouicha, B. Babes, A. Yahiou, and H. Sahraoui, "Fuzzy Logic-Based Smart Control of Wind Energy Conversion System Using Cascaded Doubly Fed Induction Generator," *Sustainability,* vol. 16, no. 21, Art. no. 9333, Oct, 2024.

[53] I. Bouguettah, M. Messadi, K. Kemih, A. T. Azar, and A. R. Mahlous, "Adaptive Passive Fault-Tolerant Control of DFIG-Based Wind Turbine Using a Self-Tuning Fractional

Integral Sliding Mode Control," *Frontiers in Energy Research,* vol. 12, no. art. 1429877, Aug. 2024.

[54] F. Boucetta, M. T. Benchouia, M. Becherif, and M. Chebani, "Direct Flux-Vector Control of Stand-Alone DFIG-Based Wind Energy Conversion System," *Proceedings,* vol. 105, no. 1, art. no. 126, May 2024.

[55] A. Tapia, G. Tapia, J. Ostolaza, and J. Sáenz, "Modeling and control of a wind turbine driven doubly fed induction generator," *IEEE Transactions on Energy Conversion,* vol. 18, no. 2, p. 194–204, Jun. 2003.

[56] P. Peng, and P. Han, "Generalized high-fidelity reduced-order modeling of doubly-fed machines and induction machines," in *Proc. IEEE Energy Conversion Congress and Exposition (ECCE)*, 2022, pp. 1–6.

[57] K. Gayathri, and S. Jeevananthan, "Candid inquest on modeling methods of doubly fed induction generator: And corroboration through simulation study," *Modelling, Measurement and Control A,* vol. 91, no. 4, p. 222–232, Dec. 2018.

[58] M. Dal, and R. Kennel, "A Dynamic Modeling Approach: Simplifying DFIG Theory, Simulation, and Analysis," *Energies,* vol. 18, no. 2, Art. no. 282, Jan. 2025.

[59] T. Djellouli, and M. Boucherit, "Speed estimation of a Doubly Fed Induction Machine controlled by a Field Oriented Control Strategy," *ENP Engineering Science Journal,* vol. 2, no. 2, p. 7–13, Dec. 2022.

[60] Z. Zheng, Z. Man, S. Tan, W. Yan, Y. Lu, J. Tian, W. Liu, and X. Wang, "Model Reference Adaptive Sensorless Control of Variable-Speed Pumped Storage Doubly Fed Induction Machine Under Reversible Operations," *Energies,* vol. 18, no. 11, Art. no. 2998, Jun. 2025.

[61] Y. Drimizi, M. Pietrzak-David, and P. Maussion, "Synchronization Angle determination in DVCSFO of DFIM naval propulsion," in *Proc. 2022 24th European Conf. Power Electronics and Applications (EPE'22 ECCE Europe)*, Hannover, Germany, 2022.

[62] J. Fletcher, and J.Yang, "Introduction to the Doubly-FedInduction Generator for Wind Power Applications," in *Paths to Sustainable Energy, A. Ng and J. Nathwani, Eds. London, UK: IntechOpen*, Dec. 30, 2010, ch. 14, pp. 259–282.

[63] B. K. Bose, Modern Power Electronics and AC Drives, Upper Saddle River: NJ, USA: Prentice Hall, 2002.

[64] R. Rouabhi, A. Zemmit, A. Herizi, O. Moussa, and S. Djeriou, "Hybrid type-2 fuzzy backstepping control of doubly fed induction generator for wind energy conversion systems," *J. Braz. Soc. Mech. Sci. Eng.,* vol. 47, no. 24, pp. 1-20, 2025.

[65] V. S. K. Lagudu, D. V. N. Ananth, and S. Madichetty, "Independent control of active and reactive power for grid connected DFIG using reference power based improved field-oriented control scheme," *International Journal of Ambient Energy,* vol. 43, no. 1, p. 3252–3265, 2022.

[66] R. K. Behara, and A. K. Saha, "Deep Q-Network Reinforcement Learning-Based Rotor Side Control System of a Grid-Integrated DFIG Wind Energy System Under Variable Wind Speed Conditions," *IEEE Access,* vol. 12, p. 184179–184205, 2024.

[67] K. Belmokhtar, M. L. Doumbia, and K. Agbossou, "Modélisation et commande d'un systeme éolien à base de machine asynchrone a doublé alimentation pour la fourniture de puissances au réseau electrique," in *Proc. 4e Conf. Int. Génie Electr. (CIGE'10)*, Bechar, Algérie, Nov. 3–4, 2010, pp. 1–8.

[68] P. S. Babu, C. K. Sundarabalan, C. B. Sundar, and T. S. Krishnan, "Fuzzy logic based optimal tip speed ratio MPPT controller for grid connected WECS," *Mater. Today Proc,* vol. 45, no. pt. 2, p. 2544–2550, 2021.

[69] E. Bekiroglu, and M. D. Yazar, "MPPT control of grid-connected DFIG at variable wind speed," *Energies,* vol. 15, no. 9, Art. no. 3146, Apr. 2022..

[70] X. Zhang, Z. Zhang, J. Jia, and L. Zheng, "A Maximum Power Point Tracking Control Method Based on Rotor Speed PDF Shape for Wind Turbines," *Appl. Sci.,* vol. 12, no. 18, Art. no. 9108, Sep. 2022.

[71] H. Chojaa, A. Derouich, O. Zamzoum, A. Watil, M. Taoussi, Y. Abdelaziz Al. Moataz, ZMS. Elbarbary, and MA. Mossa, "Robust Control of DFIG-Based WECS Integrating an Energy Storage System With Intelligent MPPT Under a Real Wind Profile," *IEEE Access,* vol. 11, p. 90065–90083, 2023.

[72] W. Ahmed, "Mechanical Modeling of Wind Turbine Comparative Study," *Int. J. Renewable Energy Res.,* vol. 3, no. 1, p. 94–97, 2013.

[73] S. Mensou, A. Essadki, T. Nasser, B. Bououlid Idrissi, and L. Ben Tarla, "Dspace DS1104 implementation of a robust nonlinear controller applied for DFIG driven by wind turbine," *Renewable Energy,* vol. 147, p. 1759 1771, Mar. 2020.

[74] J. F. Manwell, J. G. McGowan, and A. L. Rogers, Wind Energy Explained: Theory, Design and Application, 2nd ed. Chichester, U.K: Wiley, 2009.

[75] A. Gambier, "Pitch Control of Three Bladed Large Wind Energy Converters—A Review," *Energies,* vol. 14, no. 23, Art. no. 8083, Dec. 2021.

[76] J. Mohammadi, S. Vaez-Zadeh, S. Afsharnia, and E. Daryabeigi, "A Combined Vector and Direct Power Control for DFIG-Based Wind Turbines," *IEEE Trans. Sustain. Energy,* vol. 5, no. 3, p. 767–775, Jul. 2014.

[77] F. Mazouz, S. Belkacem, Y. Harbouche, R. Abdessemed, and S. Ouchen, "Active and reactive power control of a DFIG for variable speed wind energy conversion," in *Proc. 6th Int. Conf. Syst. Control (ICSC)*, Batna, Algeria, 2017, pp. 370–375.

[78] F. Blaschke, "The principle of field orientation as applied to the new transvector closed-loop control system for rotating-field machines," *Siemens Rev,* vol. 34, no. 3, p. 217–220, 1972.

[79] I. Zgarni and L. El Amraoui, "Dynamic modeling and vector control of DFIG-based wind turbine," in *Proc. 5th Int. Conf. Adv. Syst. Emergent Technol. (IC_ASET)*, Hammamet, Tunisia, 2022, pp. 262–267.

[80] M. Taleb, and M. Cherkaoui, "Active and reactive power control of doubly fed induction generator wind turbines to answer grid codes requirements," *J. Clean Energy Technol.,* vol. 6, no. 2, p. 101–106, Mar. 2018.

[81] M. Pichan, H. Rastegar, and M. Monfared, "Two fuzzy-based direct power control strategies for doubly-fed induction generators in wind energy conversion system," *Energy,* vol. 51, pp. 154-162, 2013.

[82] M. G. Simões, "Introduction to Fuzzy Control," Engineering Division, Colorado School of Mines, Golden, CO, USA, Rep., 1999, p. 1–6.

[83] I. Eker, and Y. Torun, "Fuzzy logic control to be conventional method," *Elsevier, Energy Convers. Manage.,* vol. 47, no. 4, pp. 377-394, 2006.

[84] H.Ying, "Fuzzy control and it s applications," *IEEE Trans. Syst., Man, Cybern,* vol. 26, no. 6, p. 835–846, 1996.

[85] K. M. Passino, and S. Yurkovich, Fuzzy Control, MA, USA: Addison-Wesley, 1998.

[86] G. Prabhakar, S. Selvaperumal, and P. Nedumal Pugazhenthi, "Fuzzy PD plus I control-based adaptive cruise control system in simulation and real-time environment," *IETE J. Res.,* vol. 65, no. 1, p. 69–79, Jan. 2019.

[87] B. J. Kim, and C. C. Chung, "Design of fuzzy PD + I controller for tracking control," in *Proc. Amer. Control Conf.*, Anchorage, AK, USA, 2002, vol. 3, pp. 2124–2129.

[88] I. S. Jesus, and R. S. Barbosa, "Genetic optimization of fuzzy fractional PD+I controllers," *ISA Trans.,* vol. 57, p. 220–230, Jul. 2015.

[89] S. Alavandar, and M. J. Nigam, "Fuzzy PD+I control of a six DOF robot manipulator," *Int. J. Autom. Comput.,* vol. 5, no. 1, pp. 37-43, Jan. 2008.

[90] N. M. Hatta, A. M. Zain, R. Sallehuddin, Z. Shayfull, and Y. Yusoff, "Recent studies on optimisation method of Grey Wolf Optimiser (GWO): A review (2014–2017)," *J. Comput. Theor. Nanosci.,* vol. 15, no. 5, p. 1502–1515, 2018.

[91] B. Yang, X. Zhang, T. Yu, H. Shu, and Z. Fang,, "Grouped grey wolf optimizer for maximum power point tracking of doubly-fed induction generator based wind turbine," *Energy Convers. Manage.,* vol. 133, p. 427–443, Feb. 2017.

[92] S. Tabatabaei, A. Barzegar, M. S. Sadeghi, and P. F. Roosta, "Fuzzy PD+I and fuzzy PID controllers design for a nonlinear quarter car suspension system," in *Proc. Int. Conf. Comput. Appl. Ind. Electron. (ICCAIE)*, Kuala Lumpur, Malaysia, Dec. 5–7, 2010, pp. 116–121..

Appendix

Appendix A

1. Parameters of the Double-Fed Induction Generator (DFIG)

Nominal Values

Rated power: $P_n = 4\ kW$

Stator rated voltage: $V_s/U_p = 220/380\ V$

Stator rated current: $I_s/I_p = 15/8.6\ A$

Rated speed: $\Omega_n = 1440\ rpm$

Stator rated frequency: $f = 50\ Hz$

Number of pole pairs: $p = 2$

Electrical Parameters

Stator resistance: $R_s = 1.2\ \Omega$

Rotor resistance: $R_r = 1.8\ \Omega$

Stator inductance: $L_s = 0.1554\ H$

Rotor inductance: $L_r = 0.1568\ H$

Mutual inductance: $L_m = 0.1500\ H$

Mechanical Parameters

Moment of inertia: $J = 0.2\ kg.m2$

Friction coefficient : $f = 0.001\ N.\ m.\ s/\ rad$

2. Wind Turbine Parameters

Number of blades: $N_p = 3$

Blade radius: $R_T = 3\ m$

Gearbox gain: $G = 5.4$

Moment of inertia: $J = 315\ kg.m2$

Friction coefficient: $f = 0.0024\ N.\ m.\ s/\ rad$

Air density: $\rho = 1.225\ Kg/m^2$

3. Filter Parameters

Filter resistance: $R_f = 0.25\ \Omega$

Filter inductance: $L_f = 0.005\ H$

4. DC Bus Capacitor

Capacitance: $C = 4400\ \mu F$

Appendix B

PI Controller Sizing

Figure AP-1 shows a closed-loop system corrected by a PI controller.

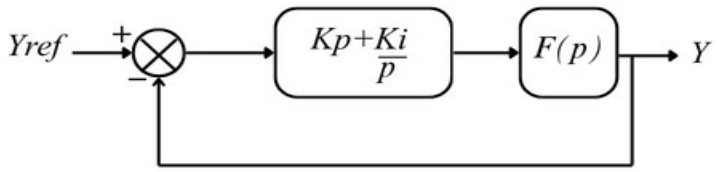

Figure AP-1 : PI Controller

The formula of the regulator PI is as follows: $k_p + \frac{k_i}{p}$

Where:

k_p is the proportional gain

and

k_i is the integral gain.

If we consider the following transfer function:

$$F(p) = \frac{k}{1+\tau p} \qquad AP-1$$

In open loop, we will have the following transfer function:

$$F_{OL}(p) = \left(\frac{k\left(k_p + \left(\frac{k_i}{p}\right)\right)}{1+\tau p} \right) = \left(\frac{k\left(k_p.p + k_i\right)}{p.(1+\tau p)} \right) = k k_i \frac{1+\left(\frac{k_p.p}{k_i}\right)}{p.(1+\tau p)} \qquad AP-2$$

We take

$$\tau = \frac{k_p}{k_i} \qquad AP-3$$

Then

$$F_{OL}(p) = \frac{k_i.k}{p} \qquad AP-4$$

In a closed loop, the transfer function is written as follows:

$$F_{CL}(p) = \left(\frac{k_i.k}{k_i.k+1} \right) = \left(\frac{1}{1+\frac{1}{k_i.k}p} \right) \qquad AP-5$$

To reach 95% of the setpoint, the response time tr of the closed-loop system is:

$$t_r = 3.\frac{1}{k_i.k} \qquad AP-6$$

Or

$$k_i = \frac{k_p}{\tau} \qquad AP-7$$

Then

$$t_r = 3.\frac{\tau}{k_p.k} \qquad AP-8$$

Where

$$\begin{cases} k_p = 3.\frac{\tau}{t_r.k} \\ k_i = 3.\frac{1}{t_r.k} \end{cases} \qquad AP-9$$

Abstract:

Variable-speed WECSs based on DFIGs require advanced control strategies to ensure efficient power extraction and reliable grid integration under nonlinear dynamics and fluctuating wind conditions. Conventional proportional–integral (PI) controllers often exhibit limited robustness and slow dynamic response in such environments.

This thesis proposes a hybrid intelligent control approach based on a fuzzy PD+I controller, whose parameters are optimally tuned offline using the GWO. The proposed method enables independent and accurate control of active and reactive power in DFIG-based systems. A comprehensive model of the WECS, including the turbine, gearbox, DFIG, and power converters, is developed and implemented in MATLAB/Simulink.

The performance of the proposed controller is evaluated and compared with PI–GWO and Fuzzy PD–GWO strategies under various operating conditions, including step changes and variable wind profiles. Simulation results demonstrate that the Fuzzy PD+I–GWO controller provides superior dynamic performance, characterized by fast response, negligible overshoot, and significant reductions in performance indices such as ITAE and ITSE. These improvements lead to enhanced energy capture efficiency and improved power quality delivered to the grid.

The proposed approach combines high performance, robustness, and implementation simplicity, making it suitable for real-time applications. It also offers promising potential for broader applications in nonlinear and uncertain energy systems.

Keywords: Power systems; Doubly fed induction generator (DFIG); Fuzzy logic control; Grey Wolf Optimizer (GWO)

Résumé :

Les systèmes de conversion d'énergie éolienne à vitesse variable basés sur les générateurs asynchrones à double alimentation (DFIG) nécessitent des stratégies de commande avancées afin d'assurer une extraction optimale de l'énergie et une intégration fiable au réseau malgré les non-linéarités et la variabilité du vent. Les régulateurs classiques de type PI présentent des limites en termes de robustesse et de rapidité de réponse.

Cette thèse propose une approche de commande intelligente hybride basée sur un contrôleur flou de type PD+I, dont les paramètres sont optimisés hors ligne à l'aide de l'algorithme GWO. Cette méthode permet un contrôle indépendant et précis des puissances active et réactive dans les systèmes à base de DFIG. Un modèle complet du système éolien, incluant la turbine, le multiplicateur, le générateur DFIG et les convertisseurs, est développé et simulé sous MATLAB/Simulink.

Les performances du contrôleur proposé sont évaluées et comparées aux approches PI-GWO et PD flou-GWO sous différentes conditions de fonctionnement, notamment des variations en échelon et des profils de vent variables. Les résultats de simulation montrent que le contrôleur proposé offre des performances dynamiques supérieures, avec une réponse rapide, un dépassement négligeable et une réduction significative des indices ITAE et ITSE. Ces améliorations permettent d'optimiser la capture d'énergie et d'améliorer la qualité de l'énergie injectée au réseau.

L'approche proposée présente un bon compromis entre performance, robustesse et simplicité d'implémentation, ce qui la rend adaptée aux applications en temps réel, avec un potentiel d'extension à d'autres systèmes non linéaires et incertains.

Mots-clés : Systèmes électriques ; Générateur asynchrone à double alimentation ; Commande floue ; Grey Wolf Optimizer

الملخص:

تتطلب أنظمة تحويل طاقة الرياح ذات السرعة المتغيرة، المعتمدة على المولدات الحثية مزدوجة التغذية (DFIG) ، استراتيجيات تحكم متقدمة لضمان الاستخلاص الأمثل للطاقة ودمجها الموثوق في الشبكة الكهربائية، في ظل الديناميكيات غير الخطية وتقلبات سرعة الرياح. وغالبًا ما تُظهر وحدات التحكم التناسبية التكاملية التقليدية (PI) محدودية في المتانة وبطئًا في الاستجابة الديناميكية عند التشغيل في مثل هذه الظروف.

تقترح هذه الأطروحة نهج تحكم ذكيًا هجينًا يعتمد على وحدة تحكم ضبابية تناسبية تفاضلية مع جزء تكاملي (FPD+I) ، حيث يتم الضبط الأمثل لمعاملاتها خارجياً باستخدام خوارزمية مُحسِّن سرب الذئاب الرمادية .(GWO) وتمكّن الطريقة المقترحة من تحقيق تحكم مستقل ودقيق في كلٍّ من القدرة الفعالة والقدرة غير الفعالة في الأنظمة القائمة على المولدات الحثية مزدوجة التغذية. كما تم تطوير نموذج شامل لنظام تحويل طاقة الرياح، يشمل التوربين الرياحي وعلبة التروس والمولد الحثي مزدوج التغذية ومحولات القدرة، وتم تنفيذه باستخدام بيئة.MATLAB/Simulink

تم تقييم أداء وحدة التحكم المقترحة ومقارنته باستراتيجيتي PI-GWO و FPD-GWO تحت ظروف تشغيل متنوعة، بما في ذلك التغيرات المفاجئة في سرعة الرياح وتغيرات معاملات النظام. وأظهرت نتائج المحاكاة أن وحدة التحكم FPD+I-GWO توفر أداءً ديناميكيًا متفوقًا يتميز بسرعة الاستجابة، وانخفاض التجاوز، وتحسن ملحوظ في مؤشرات الأداء مثل ITAE و ITSE. وقد انعكست هذه التحسينات إيجابًا على كفاءة استخلاص الطاقة وجودة القدرة المحقونة في الشبكة الكهربائية.

يجمع النهج المقترح بين الأداء العالي والمتانة وسهولة التنفيذ، مما يجعله مناسبًا للتطبيقات الآنية. كما يُظهر إمكانات واعدة للتطبيق في نطاق أوسع من أنظمة الطاقة غير الخطية وغير المؤكدة.

الكلمات المفتاحية: أنظمة تحويل طاقة الرياح؛ المولد الحثي مزدوج التغذية (DFIG)؛ التحكم الضبابي؛ مُحسِّن الذئاب الرمادية (GWO)؛ التحكم الذكي؛ تحسين الأداء الديناميكي.